

Influence of liquefaction on scour around offshore monopile foundations

Msc Thesis

March 2014



Ferdinand van den Brink

UNIVERSITEIT TWENTE.



Influence of liquefaction on scour around offshore monopile foundations

March 2014

Ferdinand van den Brink

In partial fulfilment of the requirements for the degree of

Master of science in Civil Engineering

Structural Engineering Track at Delft University of Technology

&

Master of science in Civil Engineering

Water Management and Engineering at University of Twente

Committee:

Prof. dr. ir. W.S.J. Uijtewaal
Prof. dr. S.J.M.H. Hulscher
Dr. ir. Pieter Roos
Ir. T.C. Raaijmakers
Dr. ir. W. Broere
Ir. F. Renting

Delft University of Technology
University of Twente
University of Twente
Deltares
Delft University of Technology
Delft University of Technology

Summary

Scour hole formation around offshore monopile foundations is a threat for the structure's stability. Large uncertainty leads to conservatism in design codes and hence to high construction costs. Under the same hydrodynamic loading as for scour hole formation the soil can liquefy due to structural vibrations or waves. The aim of this study is to determine the effect of liquefaction from vibrations of offshore monopile foundations on scour by performing scaled flume experiments, where liquefaction is induced by a monotonic excess pore water pressure (EPWP).

Liquefaction is known to be caused by EPWP build up under cyclic loading and normally lasts for limited time, because the built up pore water pressure drains off to the bed surface. Therefore, monotonic EPWP is introduced at the bottom of a pile, which is placed in a flume filled with fine sand. During the experiments a current is used to induce scour, while the EPWP is used as independent variable.

In the experiments the EPWP gradient is observed to take some time to bring the sediment into liquefaction. First the soil is lifted, but as soon as the vertical resistance of the sand is lost a current breaks through. Subsequently, the flow concentrates in one feeder and sediment is transported as if it is in suspension. When this occurs depends on the magnitude of the EPWP. During the scour experiments this resulted in a sudden collapse of the scour hole. The scour depth decreased and a new balance arises between slope sliding and erosion due to the horseshoe and lee-wake vortices.

It is concluded that under liquefaction the equilibrium scour depth decreases for a larger negative excess pore water pressure gradient. Furthermore, the angle of repose is decreased. The equalising effect of liquefaction on the scour hole is also expected in field situations, but the extent is unknown. The potential gain of the decreased scour depth to the structure's stability is limited, since the liquefied area may not be expected to provide any contribution to the stability of the structure.

Samenvatting

Ontgronding rondom offshore monopile funderingen vormt een bedreiging voor de stabiliteit van de constructie. Grote onzekerheid leidt tot conservatisme in de ontwerpvoorschriften en deswege een verhoging van de bouwkosten. Bij dezelfde belasting als voor ontgronding kunnen trillingen zorgen voor verweking van de bodem. Het doel van het onderzoek is om het effect te bepalen van de verweking ten gevolge van trillingen in de constructie op het ontgrondingsgedrag door middel van geschaalde experimenten in een stroomgoot, waarbij de verweking is aangebracht met een monotone grondwateroverdruk (EPWP).

Verweking kan ontstaan door accumulatie van EPWP onder cyclische belasting en heeft normaal gesproken een beperkte duur, omdat de opgebouwde poriewaterdruk naar boven wegvloeit. Daarom is EPWP aangebracht aan de onderkant van een paal, die geplaatst is in een met fijn zand gevulde stroomgoot. Tijdens het experiment wordt een constante stroming gebruikt om ontgronding te veroorzaken en de EPWP is gebruikt als onafhankelijke variabele.

Tijdens de experimenten kost het enige tijd voordat de EPWP gradiënt leidt tot verweking. Eerst worden de bodem iets opgetild, maar nadat de verticale weerstand in het zand is overwonnen, komt een stroming op gang. Wanneer dit gebeurt hangt af van de grootte van de aangebrachte EPWP. Tijdens het experiment resulteert dit erin dat het ontstane gat plotseling voor een deel instort, maar zich vervolgens verder kan ontwikkelen met een andere natuurlijke hellingshoek. De evenwichtsontgrondingsdiepte is afgenomen waarbij zich een nieuwe balans heeft ingesteld tussen afschuivend sediment en erosie ten gevolge van “horseshoe” en “lee-wake” wervelingen.

Er kan worden geconcludeerd dat de evenwichtsontgrondingsdiepte afneemt naar mate de toegepaste grondwateroverdruk toeneemt. Daarnaast is de natuurlijke hellingshoek afgenomen. Dit gelijkmakende effect van verweking wordt ook in het veld verwacht, hoewel de mate op basis van de experimenten niet kan worden geschat. De potentiële winst van de verminderde ontgrondingsdiepte fundering is beperkt, want van het verweekte gebied mag nauwelijks een bijdrage worden verwacht aan de stabiliteit van de windmolen.

Acknowledgements

With this thesis I will complete both my MSc specialisation Water Engineering & Management at the university of Twente and Structural Mechanics at Delft University of Technology.

Since this is a cooperation between two universities, this project was not so self-evident and required more dedication of my supervisors. This research would not be succeed without their help and support. Great thanks goes to my daily supervisor at Delft University of Technology Wim Uijtewaal for his great guidance and critical feedback. I experienced our meetings as very interesting and constructive. Besides, I would like to thank my everlastingly enthusiastic daily supervisor Twente University Pieter Roos for his useful feedback and understanding. I would like to thank Suzanne Hulscher for the pleasant and useful meetings and here support throughout the project when I needed it. I am very grateful to the other members of the committee Tim Raaijmakers, Wout Broere and Frank Renting, for their feedback.

For the construction of the research setup a lot of people were assisting, including Hans Tas, Jaap van Duin, Frank Kalkman and Tom from DEMO. Special thanks goes out for Sander de Vree, who was always willing to listen and help with the practical problems I faced in a constructive way.

Next I thank my fellow students at the MSc room for their companionship, motivating eeuwige roem punten system and numerous kleintjes. Finally I would like to thank my family and friends for their aid and confidence.

Contents

Summary	3
Samenvatting	4
Acknowledgements	5
List of symbols	11
1. Introduction.....	13
1.1 Current developments on offshore wind energy.....	13
1.2 Goal of research.	16
1.3 Research questions	16
1.4 Methodology	16
1.5 Outline of report.....	16
2. Theoretical background	17
2.1 Introduction.....	17
2.2 Fundamental hydrodynamic and morphodynamic processes.....	18
2.2.1 Bed shear stress	18
2.2.2 Shields parameter.....	19
2.2.3 Important dimensionless quantities	20
2.3 Classifications and definitions	21
2.3.1 Slender piles and large piles	21
2.3.2 Local and global scour.....	22
2.3.3 Clear-water and Live-bed	22
2.3.4 Current-induced and wave-induced	22
2.3.5 Liquefaction.....	23
2.4 Theory on scour hole development.....	23
2.4.1 Mechanism	24
2.4.2 Equilibrium scour depth.....	26
2.4.3 Time-bound behaviour of scour	29
2.4.4 Shape of scour hole	32
2.5 Theory on liquefaction	32
2.5.1 Momentary liquefaction.....	33
2.5.2 Residual liquefaction	34
2.6 Conclusion	36
3. Field characteristics.....	37
4. Experimental setup.....	39
4.1 Introduction.....	39
4.2 Physical model setup	39
4.2.1 Flume	39

4.2.2 Liquefaction.....	41
4.2.3 Soil	43
4.3. Measurements.....	44
4.3.1 Measurement of scour depth	44
4.3.2 Pore water pressure	45
4.3.3 Velocity measurement	46
4.3.4 Water depth measurement.....	47
4.3.5 Data acquisition	47
4.4 Performed model tests	47
5. Results	49
5.1 Reference case	49
5.2 Results with liquefaction.....	51
5.2.1 Effects of liquefaction on the soil	51
5.2.2 Liquefaction during the scour experiments.....	52
5.2.3 Effect on scour depth and time scale	53
5.3 Results of the pore water pressure	57
6. Discussion.....	61
6.1 Behaviour of scour during experiments.....	61
6.2 Functioning of setup	62
6.2.1 Endoscope camera.....	62
6.2.2 Constant pressure as liquefaction mechanism.....	65
6.2.3 Porous stone	65
6.2.4 Resistance in tube and porous stone.....	66
6.2.5 Discharge measurement and bed velocity measurement	67
6.3 Measurement errors	67
6.3.1 Measurement of the scour depth.....	67
6.3.2 Other measurement errors.....	68
6.3.3 Overview measurement errors.....	68
6.4 Pore pressure analysis.....	69
6.5 Implications of results for liquefaction in field	71
7. Conclusions and recommendations.....	75
7.1 Conclusions	75
7.2 Recommendations for further research	76
7.3 Recommendations on experimental setup.....	77
References	79
Appendix A: Side view flume.....	87
Appendix B: Design considerations for the experiment	88
Points of departure for the design of the experiment	88

Design quantities of setup	89
Appendix C.1: Notes on optical measurement on the scour depth.....	92
Design	92
Practice	93
Calibration.....	93
Appendix C.2: Endoscope Voltcraft SB 16.....	95
Appendix C.3: Operations by Matlab to determine the scour depth.....	97
Detection of the border	97
Detection of middle of pile	98
Appendix C.4: Matlab script on determination scour depth	100
Appendix D.1: Water pressure gauge – Technical specifications.....	102
Appendix D.2: Water pressure gauge – Calibration	108
Appendix D.3: Result of pore water pressure measurements	110
Appendix E: Electromagnetic flow meter	115
Appendix F: Preliminary tests on liquefaction.....	116
Setup.....	116
Results	116
Description of process	117

List of symbols

b_{flume}	Width of flume
C_D	Dimensionless drag coefficient
CRR	Cyclic Resistance Ratio
CSR	Cyclic Stress Ratio
D	Pile diameter
d	Median grain size
D^*	Dimensionless grain size
$e_r, e_z, e_{h, sed}, e_{h, w}$	Measurement error of r, z, h_{sed}, h_w
f_p	Peak frequency of the wave power spectrum
Fr	Froude number
FS	Factor of safety
g	Acceleration due to gravity
H	Wave height
h_{flume}	Height of flume
h_{image}	Height of image expressed in pixels
h_{sed}	Sediment height
h_{sed}	Thickness of porous stone
h_w	Water height
Kc	Keulegan-Carpenter number
K_d	Sediment size factor
K_I	Flow intensity factor
K_{mob}	Mobility factor
k_s	Nikuradse roughness
K_s	Shape factor
K_t	Time factor
K_a	Alignment factor
K_δ	Boundary layer depth to pile size ratio
L	Wave length, Length of vortex street
M	Stress amplification factor
\dot{p}	Period averaged excess pore water pressure
Q	Discharge
Q_{max}	Maximum discharge
r	Radial coordinate in images
Re	Reynolds number
S	Equilibrium scour depth
S_a	Actual scour depth in time
t	Time
t^*	Dimensionless time
T_b^*	Dimensionless timescale for backfilling
T_c^*	Dimensionless timescale for current-induced scour
$t_{99\%}$	Time for 99% of scour hole evolvement
T_c	Timescale for current-induced scour
t_e	Time to attain clear-water equilibrium scour depth

T_p	Wave period
U	Velocity in long direction
\bar{U}	Depth-Average flow velocity
U_a	Armouring peak velocity
U_c	Undisturbed current velocity at D/2 from the bed
U_{cr}	Critical velocity
U_{cw}	Velocity ratio, $U_c/(U_c + U_w)$
u_e	Excess pore water pressure
U_f	Undisturbed bed friction velocity
u_{hs}	Hydrostatic pore water pressure
U_m	Maximum value of undisturbed orbital velocity at the bed
U_w	Amplitude of the orbital velocity at the seabed
V_c	Undist. current vel. at D/2 from bed perpendicular to main flow dir.
$w_{downstream}$	Downstream scour width
w_{side}	Scour width sides
$w_{upstream}$	Upstream scour width
z	Vertical coordinate
z_0	Bed roughness length
z_{image}	Vertical coordinate from images
α	Angle inclination scour hole
γ_s	Bulk unit weight of sediment
γ_w	Bulk unit weight of water
δ	Boundary layer thickness
$\Delta_{p,a}$	Applied height difference bucket water level in flume
$\Delta_{p,od}$	Measured hydraulic head in porous stone
θ	Shields parameter at the bed
θ_a	Shields parameter under ambient conditions
θ_{cr}	Critical shield parameter
κ	Von Karnman constant
ν	Kinematic viscosity
ρ	Density of water
ρ_s	Density of sediment
σ_g	Geometric standard deviation of sediment
σ_v	Vertical stress in soil
σ'_v	Vertical effective stress
$\tau_{0,ambient}$	Ambient bed shear stress
$\tau_{0,local}$	Local bed shear stress
τ_b	Bed shear stress
ω_w	Angular frequency of the waves

1. Introduction

1.1 Current developments on offshore wind energy

Offshore wind energy is a rapidly developing industry. The rising awareness in the western society of the current dependence on fossil fuels and its impact on global warming, has driven up the demand for alternatives. Wind energy is considered as an environmentally friendly and inexpensive alternative. People generally have a positive attitude towards wind energy, although they dislike turbines to be built close to their houses, because of its visual impact, noise and influence on property value. Because scarcity of construction locations, offshore wind turbines are considered as an attractive alternative and have a large unexploited potential.

Furthermore, offshore wind speeds are higher, implying a larger productivity per turbine. It also allows for a more efficient turbine design, as there are no size limits from requirements on visual impact, noise and issues with transportation of large prefabricated components. On the other hand, the installation and maintenance costs of offshore wind turbines are higher. This can be ascribed to (Henderson et al., 2003):

- The more expensive foundation, due to the increased height of offshore wind turbines and larger foundation length;
- More expensive integration in the electrical network, because the transmission of energy is done over a longer distance in a marine environment and because of the irregular supply of wind energy.
- More expensive installation costs, due to more expensive installation procedures and restricted access owing to weather conditions.
- More expensive maintenance locations can only be reached during 50 – 75% of the time and organisational difficulties with unexpected repairs.

Therefore offshore wind energy is now still 1,5 to 2 times as expensive as onshore. To improve the attractiveness of offshore wind, a combination of innovations and economies of scale is aimed at (Breton and Moe, 2009; Sun et al., 2012).

Despite these disadvantages, a number of offshore wind farms have recently been built and will be built coming decades. Nowadays, Europe has a lead over the rest of the world in the development of offshore wind. Especially around the shallow and sheltered North Sea several wind farms have been built and have been planned, as can be seen in figure 1 (Offshore Wind Energy, 2008). The offshore wind farms show a trend toward larger wind farms and turbines in deeper water at greater distances from the shore, although this implies increased construction costs (Sun et al., 2012).

Here the most common foundation type is the monopile foundation (about 65%) besides gravitation based foundations (25%) and jacket foundations (8%)(Van der Walle, 2011). Monopile foundations are currently feasible up to a water depth of 30 meters. For deeper water multiple footed and floating structures become a more feasible option (Breton and Moe, 2009). The dimensions of a typical design of an offshore wind turbine with a monopile foundation is shown in figure 2. Note that in this example scour protection has been applied.

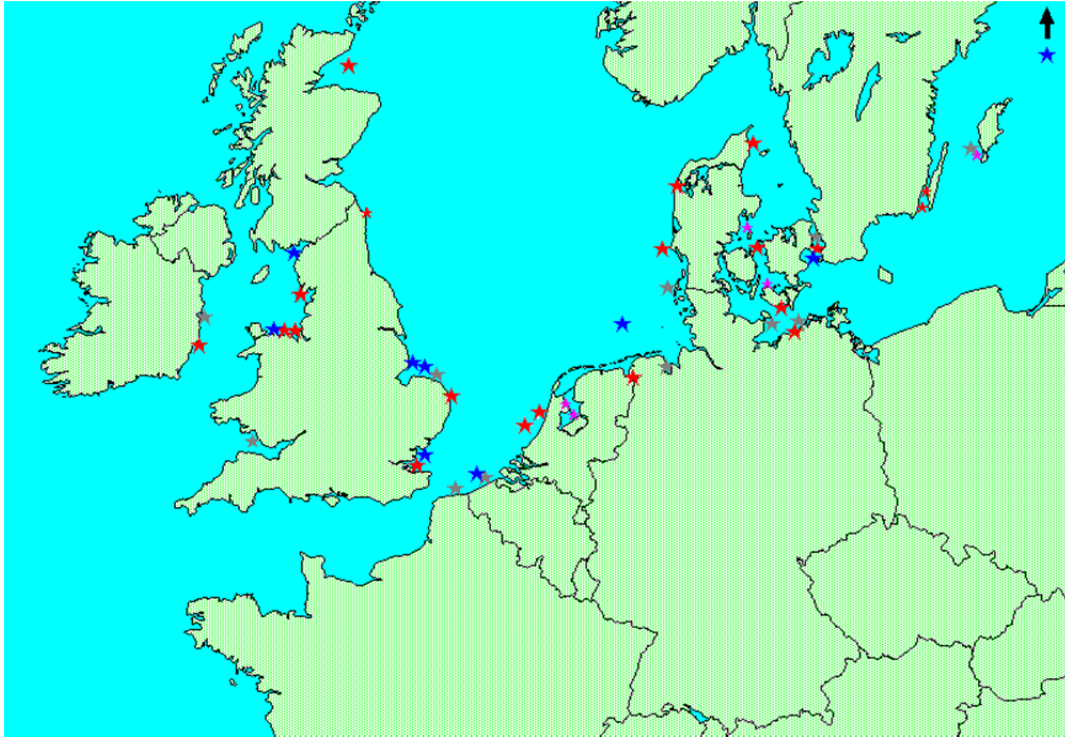


Figure 1: Existing and planned wind farms in North West Europe. Red = Already built, purple = built small turbines, blue = under construction, grey = planned (from Offshore Wind Energy, 2008).

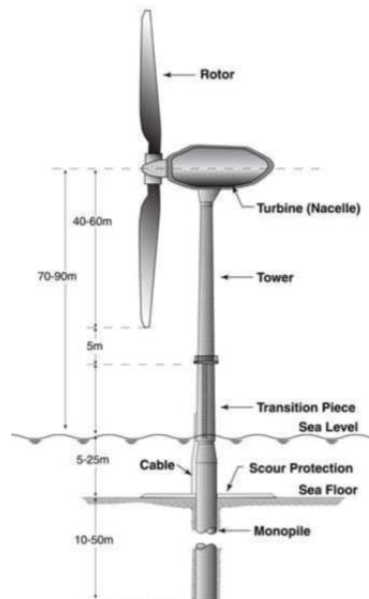


Figure 2: Typical dimensions for an offshore wind turbine with a monopile foundation (from Malhotra, 2011)

In the design of the offshore wind turbines still a lot of uncertainty is present. In the load or in the load combinations a conservative design method is chosen. Consequently redundant construction costs are made. Foundation costs are between 15% and 40 % of the total costs of current offshore wind farm projects. The process of scour is one of the many design issues of the wind turbines.

An illustration of a large discrepancy between design assumptions and actual situation is given by Gómez (2007). Here the actual water depth at a turbine on the Arklow Bank

was found to be 5.25 meter. Due to all assumptions, including on scour and sand waves, 9.30 meter was required to take into account in the design, though during the 6 months of measurement no variation was found on the actual bed level.

Other illustrations of the implications of redundant conservatisms on scour design in practice are given by Hartvig et al. (2010) and Høgendal and Hald (2005). The first aims to predict the scour holes in time and space. Predicting scour behaviour around monopile foundations is important for the planning around the deployment of scour protection. It is even more important when no or partial scour protection is used. Large uncertainties include the process of backfilling, which is counteracting the scour process during milder hydrodynamic conditions. Depending on the local physical circumstances, partial protection or a design with free scour development may be economically attractive as is shown by Raaijmakers et al. (2013), but are not chosen due to the increased uncertainty it brings about.

Høgendal et al. (2005) show what the current design assumptions are on the scour depth. The current practice now takes into account a constant value for scour irrespective of the hydrodynamic conditions (DNV, 2013). This is the maximum scour that could be present from a quasi-steady current only. When waves are present, this scour depth is never reached. Furthermore it is based on the most extreme case, but since it takes time for the scour hole to develop, the equilibrium scour depth corresponding with this extreme case may not be reached (Høgendal et al., 2005).

The need for increased efficiency is illustrated by the intention of the Dutch government to increase the installed power supply from offshore wind turbines from the current 250 MW to 3450 MW in 2023. This is a result of the agreement of the Dutch government in September 2013 that offshore wind will provide a substantial part of renewable energy. Here the construction preparations for three wind farms are already in execution, while another 9 have been granted a permit but are waiting for funding. Risks are run by the developing companies, so the construction relies on subsidies from one fund for all renewable energy sources. For the governmental subsidies offshore wind has to compete with other forms of renewable energy, while other sustainable energy sources are still more cost effective. Therefore, the Dutch government will only provide the subsidy to the planned 3450 MW of wind energy plants when the industry is able to achieve a cost reduction of 40% in the coming years. This cost reduction should come from innovations and economies of scale (Dutch Ministry of Infrastructure and Environment, 2013).

One of the design aspects in offshore wind turbines is scour around the foundations. By increasing knowledge on this topic it is expected to contribute to an economically more attractive design. The proposed research aims at improving the knowledge on the process of scour around offshore wind turbines. Furthermore, due to both hydrodynamic loading and aerodynamic loading the pile is likely to vibrate. This pile movement continues below the bed level. It is proposed here to investigate whether these vibrations can have an effect on the scour that usually takes place around the pile. So far, this has only been investigated for clay soils (Reese et al., 1989). However, the driving mechanism here strongly differs from the mechanism behind scour in non-cohesive bed material.

The vibrations of the piles in a sandy soil are expected to have a number of effects. In the first place it can densify the soil around the pile. Furthermore, the soil has to take up the stresses induced by the vibrations of the structure. The pore pressure respond to these vibrations. Due to the vibrations the soil may lose part of its shear strength

(Whitehouse, 1998). In a similar way the vibrations of a structure under cyclic loading can lead to soil liquefaction in extreme cases (Sumer and Fredsøe, 2002). Here liquefied soil is sediment that transformed into a state where the soil acts as being a liquid. Besides from structural vibrations, liquefaction can take place as a consequence of waves or earthquakes.

1.2 Goal of research.

The aim of this research is to determine the effect of liquefaction from vibrations of offshore monopile foundations on scour by performing scaled flume experiments where liquefaction is induced by a monotonic excess pore water pressure.

1.3 Research questions

1. What are the observed effects of liquefaction on the scour depth and time scale of scour development?
2. How is the functioning of the research setup?
3. To what extent can the result from the laboratory be considered to be representative for the effect of vibrations of offshore wind turbines in the field?

1.4 Methodology

Many scour problems are investigated by the use of physical modelling. So far only a few studies have been performed where both liquefaction and scour were observed in one experiment. Only little is known on the combinations of both phenomena. Therefore, scaled experiments are performed in a flume.

This study focuses on the influence of structural vibrations through liquefaction on scour. In order to exclude the effects that do not relate to liquefaction, a pile modelling a monopile foundation is fixed and a monotonic excess pore water pressure applied. If this pressure is large enough and lasts for a sufficiently long time, the sediment grains lose their mutual contact and the soil becomes liquefied. Different values for the excess pore water pressure are used and compared with a reference scour experiment, where no liquefaction was present.

1.5 Outline of report

First, the phenomena of scour and liquefaction are introduced. A theoretical background is given on both in chapter 2. Next, the field characteristics are shortly described in chapter 3. After that the experimental setup and measurement devices are described and motivated. In addition the conditions during the experiments and the steps that are followed are given in chapter 4. In chapter 5 the behaviour during the reference case is presented. Furthermore, the observed processes during the tests with liquefied soil are described. This is supported with the measurements of scour depth and pore water pressure. In chapter 6 a discussion is given on the obtained results and measurements. Furthermore the implications of the results from the laboratory for the situation in the field are discussed here. Finally, the conclusions and recommendations are given in chapter 7.

2. Theoretical background

2.1 Introduction

Scour is a process which takes place when a fixed structure is placed in a marine or fluvial environment with an erodible bed. As a consequence of the structure the water flow pattern is disturbed. This can lead to the following flow pattern changes (Sumer and Fredsøe, 2002):

- Contraction of flow
- Formation of horseshoe vortices
- Formation of lee-wake vortices
- Generation of turbulence
- Reflection and diffraction of waves
- Wave breaking

All these flow pattern changes are likely to affect sediment transport around the structure, though their importance may differ for different applications. For offshore monopiles, which can be classified as slender piles (see section 2.3.1), the most important processes have been illustrated in figure 3. More on the flow characteristics around cylinders can be found in e.g. Sumer and Fredsøe (1997).

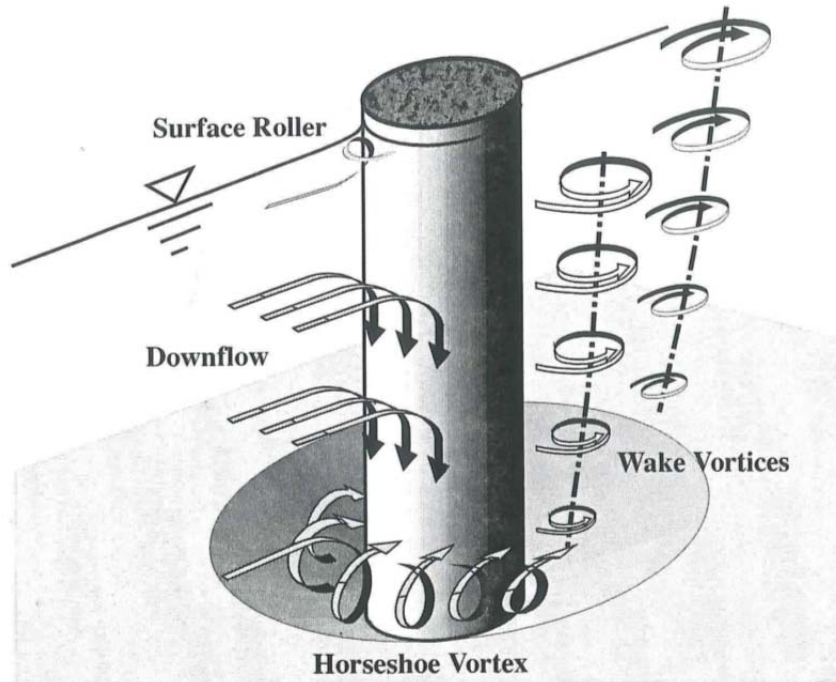


Figure 3: Flow pattern around monopile (original from Melville and Coleman, 2000)

The additional eddies lead to higher bed shear stresses around the structure compared to the ambient bed shear stress. The bed shear stress is the principal factor determining the onset of scour, because it controls sediment transport locally. This amplification of bed shear stress M is therefore expressed as the ratio between the local bed shear stress $\tau_{0,local}$ and the ambient bed shear stress $\tau_{0,ambient}$.

$$M = \frac{\tau_{0,local}}{\tau_{0,ambient}}$$

This results in a shear stress pattern as for example given by Hjort (1975), see figure 4. Here the shear stress distribution is shown around a pile as being measured during experiments.

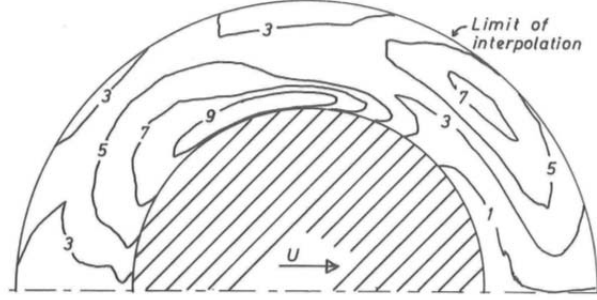


Figure 4: Pattern of shear stress amplification M from cylindrical pile. Here with flow velocity $U = 30$ cm/s and water depth $H = 10$ cm (from Hjorth, 1975)

The rate of erosion initially follows the bed shear stress pattern.

The remainder of this chapter further elaborates on the processes behind scour. To this end, the definitions are presented for the shear stress, Shields parameter, Froude number, Reynolds number and Keulegan-Carpenter number in section 2.2. Furthermore, in section 2.3 a number of classifications are made to further specify scour as is investigated with this research. Finally, in section 2.4 and 2.5 the relevant knowledge on scour and liquefaction is given.

2.2 Fundamental hydrodynamic and morphodynamic processes

2.2.1 Bed shear stress

As stated in section 2.1 scour is initiated when the bed shear stress exceeds a critical value. The definition of the bed shear stress for a horizontal bed and turbulent flow is

$$\tau_{bed} = \rho \nu \left. \frac{dU}{dz} \right|_{z=z_{bed}}$$

Where ν is the eddy-viscosity and U is the flow velocity.

The shear is caused by the velocity at the bed, which can be determined by assuming a logarithmic velocity profile

$$U(z) = \frac{U_f}{\kappa} \ln \left(\frac{z}{z_0} \right)$$

Here U_f is the undisturbed bed friction velocity, κ is the Von Karman constant being $\kappa = 0.4$, z is the distance from the bed and z_0 is the reference level near the bottom where the flow velocity is zero. When the bed is assumed as a hydraulic rough wall $z_0 = k_s / 30$. k_s is the Nikuradse roughness, often used being $k_s = 2.5d$ and d is the median sediment grain size.

The depth-averaged flow velocity \bar{U} is obtained by integration over the water column.

$$\bar{U} = \frac{1}{h_w} \int_{z_0}^{h_w} U(z) dz = \frac{U_f}{\kappa} \ln \left(\frac{30h_w}{k_s} \right)$$

Here h_w is the water height. The relation between the bed shear stress and undisturbed friction velocity U_f is by definition:

$$\tau_b = \rho U_f^2$$

Consequently,

$$\tau_b = \rho C_f \bar{U}^2$$

Where ρ is the density of water. C_f is a dimensionless drag coefficient and is for hydraulic rough flow (Soulsby, 1997)

$$C_f = \left(\frac{0.40}{\ln(h/z_0) - 1} \right)^2$$

2.2.2 Shields parameter

The shear stress at the bed is often expressed in non-dimensional form being the Shields parameter θ , given by

$$\theta = \frac{\tau_b}{g(\rho_s - \rho)d},$$

where ρ_s is the density of the sediment. At the threshold of sediment motion the lift force from a current at the bed exceeds the force from the submerged weight. If a critical velocity is exceeded corresponding to a threshold shear stress τ_{cr} , a sediment particle comes into motion. The shear at the threshold of motion expressed in a non-dimensional way is

$$\theta_{cr} = \frac{\tau_{cr}}{g(\rho_s - \rho)d}$$

The threshold of motion is given by the Shields curve as is given in figure 5.

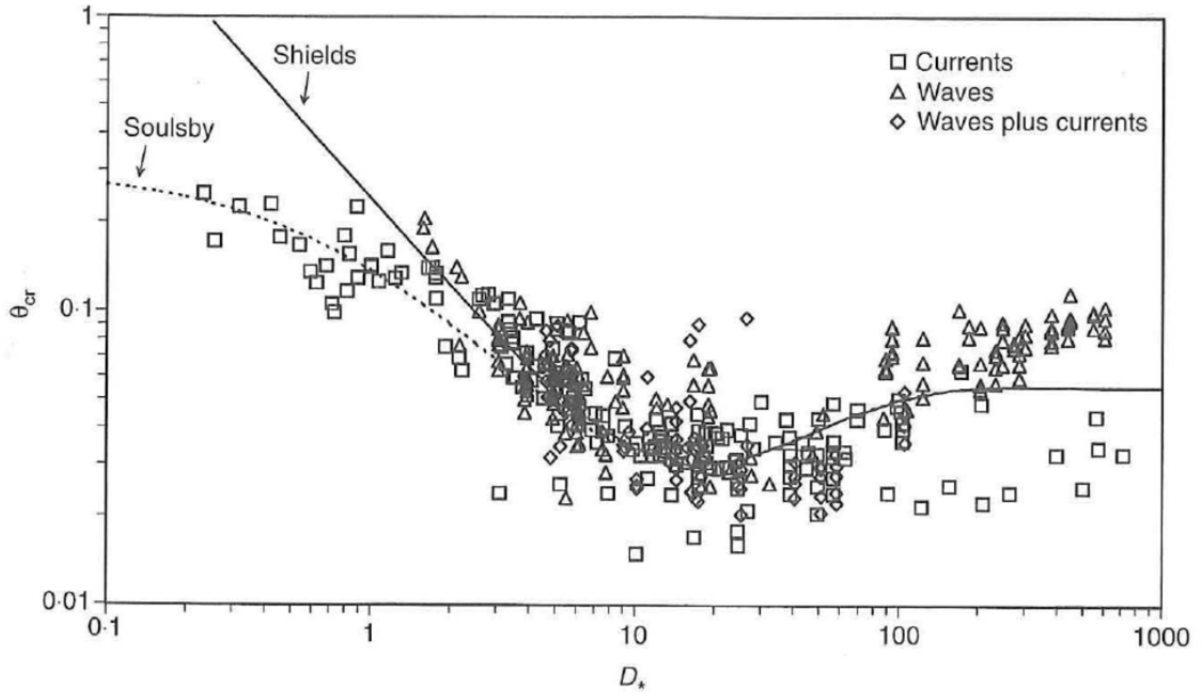


Figure 5: Shields curve from Soulsby (1997)

Here the dimensionless grain size D_* is given by

$$D_* = d \left(\frac{(\rho_s / \rho - 1)g}{\nu^2} \right)$$

Where ν is the kinematic viscosity of the fluid.

Just above the critical velocity the dominant mode of sediment transport is bed load sediment transport. When the flow velocity increases, the smaller particles start to lose their contact with the bed. When more sediment is transported as suspended sediment, the suspension threshold is passed. This is not a clear threshold, since it depends not only on the median grain size, but also on the distribution of the sand, which is quite irregular in the field (Knighton, 1998).

2.2.3 Important dimensionless quantities

Scour and the hydrodynamic circumstances are typically characterised by a number of dimensionless quantities. These include the Froude number Fr , the Reynolds number Re and the Keulegan-Carpenter number Kc . These are will be defined below.

The Froude number is defined as the ratio of a characteristic velocity to a gravitational wave speed and it gives the relative influence of the inertial force to the gravity force in a hydraulic flow. This is defined as

$$Fr = \frac{U}{\sqrt{gh_w}}$$

Where U and h_w are a flow velocity and water depth respectively, which depend on the context. g is the acceleration due to gravity. The Froude number distinguishes whether

a flow is in a subcritical state, where $Fr < 1$ and disturbances are transmitted upstream or supercritical where $Fr > 1$ and disturbances are not transmitted upstream (Hughes, 1993).

The Reynolds number Re is in the context of scour often based on the pile diameter D .

$$Re_D = \frac{UD}{\nu}$$

The Keulegan-Carpenter number Kc is important in the description of scour, since it is a way to express the relative amplitude of orbital motion to the pile diameter. For scour caused by waves this is the main parameter required to determine the equilibrium scour depth. This quantity is defined as

$$Kc = \frac{U_m T_p}{D}$$

Where $T_p = 2\pi / \omega_w$ is the peak wave period, defined with $T_p = 1 / f_p$ and f_p is the peak frequency of the wave power spectrum. U_m is the maximum value of the undisturbed orbital velocity at the bed and can be calculated from small amplitude sinusoidal wave theory (Sumer and Fredsøe, 2002a). Furthermore, D is the pile diameter, a is the amplitude of orbital motion and ω_w is the angular frequency of the waves. A small value of Kc means that the amplitude of the orbital motions from a wave is small compared to the pile diameter.

2.3 Classifications and definitions

As stated in chapter 1, this research focuses on scour around offshore monopiles, so on piles with a circular shaped cross-section. For this type of structure a number of classifications can be made. Every classification here is used to further specify this research and shows how it can be related to other research.

2.3.1 Slender piles and large piles

Among others, scour depends on the pile diameter. Therefore the scour depth S is often made dimensionless with the pile diameter D . Furthermore, two driving mechanism regimes are possible. When the pile diameter is small compared to the water height, the flow is separated. This leads to separation vortices like horseshoe vortices and lee-wake vortices. Alternatively, for very large diameters the structure is too big and functions more as a wall. No separation vortices are present, but diffraction and reflection effects become important. This is the case when $D / L > O(0.1)$, where L is the wave length. Then piles are classified as large piles. The Keulegan-Carpenter numbers are generally small ($Kc > O(1)$) (Sumer and Fredsøe, 2002). However, for slender piles $D / L < O(0.1)$ (Klinkvort and Hededal, 2011) scour takes place when $Kc > O(6)$ (Sumer and Fredsøe, 2001). It should be noted here that the classification on Kc numbers only holds when a steady current is absent. Offshore monopile foundations are generally slender, so this research focuses on slender piles only.

2.3.2 Local and global scour

Around all single piles scour occurs when the flow velocities are high enough to cause sediment movement. Around single piles the scour is defined as local scour. When a group of objects is enhancing scour, the large scale scour pattern can be defined as global scour. Alternatively this is referred to as dishpan scour or general scour (Whitehouse, 1998; Diamantidis, 1986). This is clarified in figure 6 with the idealised photographic representation of Angus and Moore (1982).

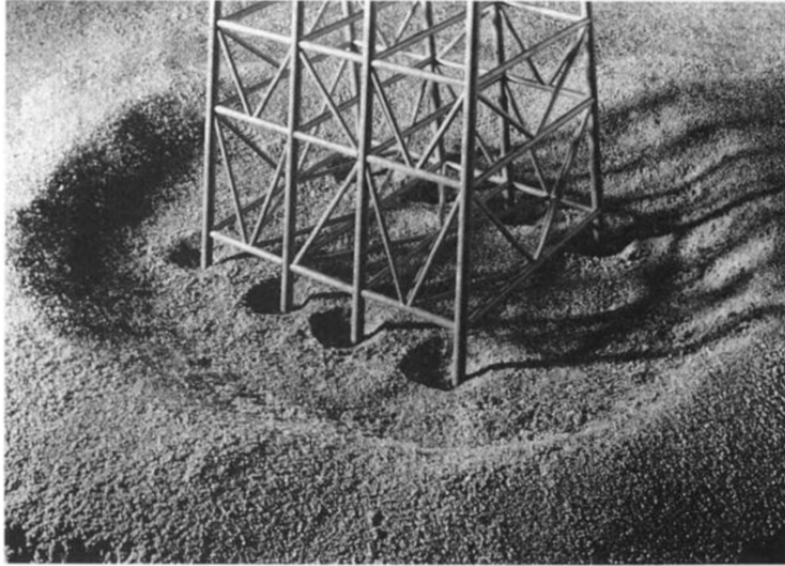


Figure 6: Photographic representation of local scour around each individual pile and global scour around the structure as a whole (from Angus and Moore, 1982)

2.3.3 Clear-water and Live-bed

This classification is based on whether flow conditions around the ambient bed are such that sediment transport takes place or not. The occurrence of sediment transport depends on whether the bed shear stress exceeds the critical shear stress, or equivalently whether the shields parameter exceeds its critical value. When sediment is transported around the structure, whereas far away from the structure it is not, the scour is referred to as clear-water scour. Conversely, when the critical bed shear stress is exceeded at undisturbed flow conditions, so when $\theta_a > \theta_{cr}$, this is referred to as a live-bed condition. This is clarified with the photos in figure 7 from experiments done by Hartvig et al. (2010).

2.3.4 Current-induced and wave-induced

As also becomes clear from figure 7, the scour pattern strongly depends on whether the flow is a steady current or whether wind waves are present too. Both the scour depth and the timescale at which the scour take place depend on the presence and power of waves. Both conditions are often studied separately, though more recent studies perform combined experiments, since the effects of waves are usually enlarged by tide-induced currents. In the present research it is attempted to isolate the problem as much as possible. Therefore only current-induced scour is regarded.

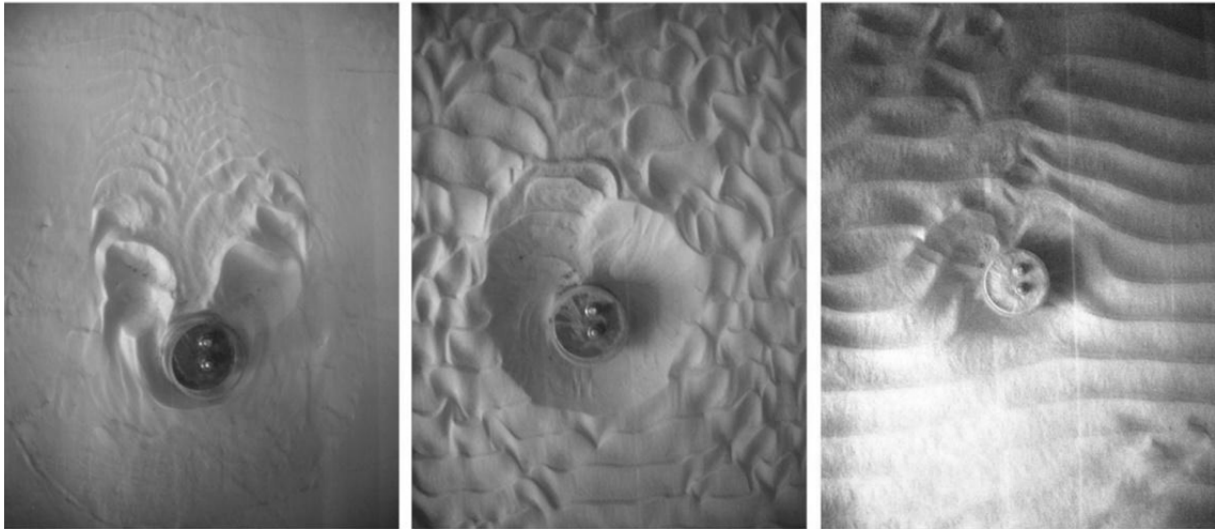


Figure 7: Photos from scaled experiment with a) unidirectional flow under clear-water conditions b) unidirectional flow under live-bed conditions and c) currents and waves under live-bed conditions (obtained from Hartvig et al, 2010)

2.3.5 Liquefaction

Excess pore water pressures can affect the foundation in a number of ways (Whitehouse et al., 2004):

- Generation of net uplift pressures on the foundation
- Changes to the skin friction on the foundation wall
- Potential for seabed liquefaction.
- Horizontal stiffness of foundation to deflections

This research investigates on the influence of seabed liquefaction on scour. Under the influence of waves, earthquakes or structural vibrations the pore water pressure may increase such that the seabed becomes liquefied. Since a liquefied bed barely has any shear strength, the sediment can be eroded more easily than a non-liquefied bed (Whitehouse, 1998).

Liquefaction means that the material behaves as if it were a liquid. For cohesionless soils this is defined by Marcuson (1978) as being “the transformation of a solid state to a liquefied state as a consequence of increased pore pressure and reduced effective stress”. Consequently the capacity of the soil to support vertical load is lost and the soil is much more susceptible to erosion (Whitehouse, 1998).

2.4 Theory on scour hole development

Steady flow scour has been extensively studied in the fluvial context of bridge piers. The main mechanisms behind scour are explained here to get insight in the processes that cause scour. These are the horseshoe-vortices, the lee-wake vortices and flow contraction. The problem of scour falls apart in the depth the scour hole may reach, the time it takes for the hole to develop this depth and the shape of the scour hole. These are discussed below, where focus is put on current induced scour, since a current was used to induce scour during the experiments of this research.

2.4.1 Mechanism

The dominant feature of scour around a pile is the horseshoe-vortex system (Breusers, 1977), although initially the cross-section of the vortices is small and its influence is weak. As noted in section 2.1, this causes an increased bed shear stress around the pile. Consequently the bed starts to erode. With the formation of the scour hole the vortex rapidly grows in size and strength as additional fluid attains a downwards component and the strength of the downward flow increases. During the development of the scour hole, the shape of the hole remains the same and therefore the shape of the bed shear stress, flow magnitudes, flow directions and turbulence intensities remain similar. As the depth of the hole increases, the down flow near the bottom of the scour hole decreases and therefore the erosion rate starts to decrease. This scouring process continues till an equilibrium scour depth has been reached. For clear-water scour the equilibrium is a condition at which the depth of scour ahead of the cylinder is just sufficient so that the magnitude of the vertically downwards flow can no longer dislodge surface grains at the bed surface. For live-bed conditions the equilibrium is a balance between the erosion of sediment by the downward flow and the incoming sediment from upstream. Behind the pile the eroded sediment settles down, where it is progressively reworked and flattened by the flow out of the scour hole (Melville, 1975).

Behind the pile lee-wake vortices arise. These vortices are convected downstream at a speed initially less than the approaching flow, but after a distance of $8D$ it almost approaches this flow velocity. The shape changes along its way. Just behind the cylinder its centre is vertical over the water height, but due to the difference in mean flow over the height, it tends to bend further away from the cylinder at the upper part of the water column. Due to the lower pressure in the middle, the vortices attract sediment towards their centres and may bring it into suspension. Behind the pile a ripple arises coinciding with the path of the cast-off vortices (Melville, 1975).

At the sides of the pile both vortex systems interfere with each other. The arms of the horseshoe vortices extend around the pile and oscillate on the same frequency as the lee-wake vortices, both horizontally and vertically. This is because the location of the lee-wake vortex influences the pressure distribution and pulls the vortex arm with it.

More recent research focused on scour from waves only. Early studies focused on the description of scour from both waves and current by looking at relevant dimensionless parameters (e.g. Eadie and Herbich, 1986). More recently Sumer et al. (1992a) studied scour induced by waves only.

When the scour is caused by waves, the same processes take place as under currents, but now the current is oscillatory. Therefore the main driving mechanism under current, being the horseshoe vortex, shows inertia and is not fully developed all the time. When the wave period is long enough, the flow can be considered to be quasi-steady during every half cycle. Then also the horseshoe vortex is fully developed. However, when the wave period is small, the horseshoe vortex does not get enough time to develop, the scouring mechanism is less strong and the relative importance of wave vortices increases. Therefore the amount of scour strongly depends on the wave characteristics.

In order to express the relative importance of the inertia, the Keulegan-Carpenter number Kc is used, which is defined in section 2.2.3.

The horseshoe and lee-wake vortices are not present for $Kc < 6$ and consequently no scour takes place. Scour can still take place as a consequence of flow contraction.

Because the blockaded area in the flow, the streamlines contract at the side edges of the pile. When the Kc value is small, horseshoe vortices are only present for a small part of the half-wave period as can be seen from figure 8. Also vortex shedding occurs from $Kc > 6$. Individual vortices function as a significant mechanism to erode sediment away from the pile. Sumer et al. (1992a) found that the length L of the vortex street formed at the lee side of the pile depends linearly on the Kc number.

$$\frac{L}{D} = 0.3Kc$$

When the Kc value increases, the horseshoe vortices remain over a larger time span and increase in relevance. For $Kc > 30$ these horseshoe vortices start to dominate (Sumer et al., 2002).

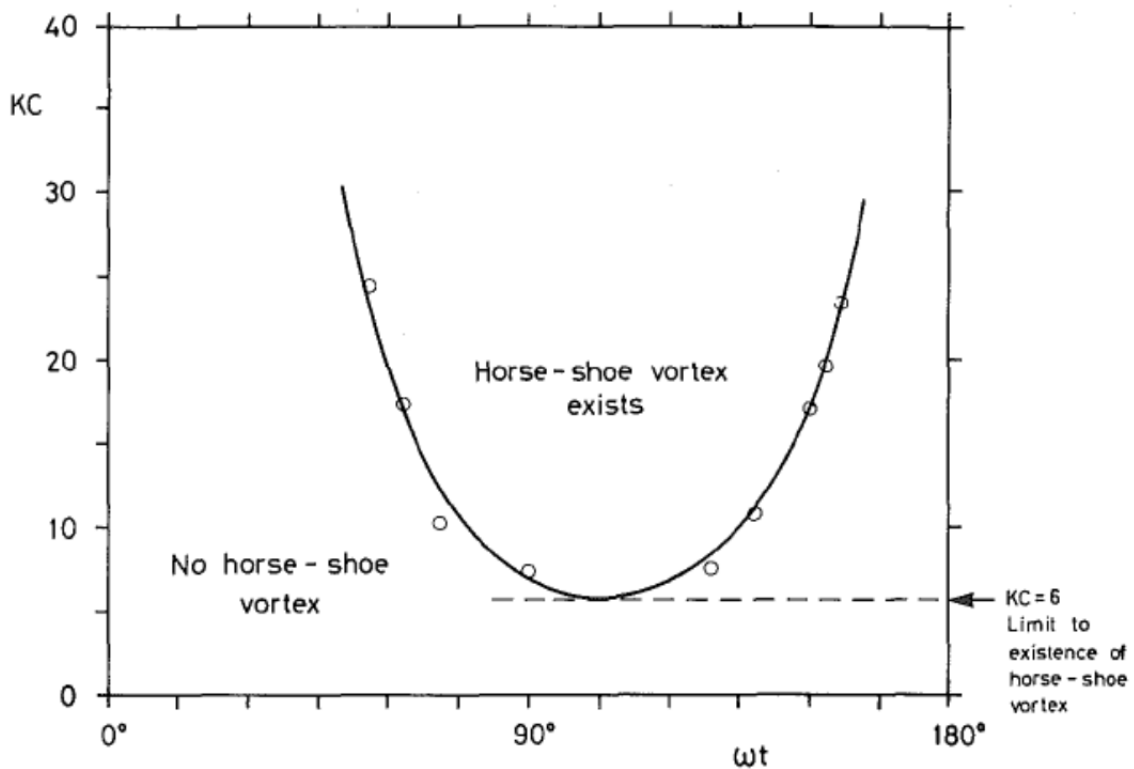


Figure 8: Existence of horseshoe vortex over wave period (from Sumer et al., 1992a)

When a current co-exists with waves, the additional current increases the flow velocity just above the bed. Therefore, the scour is likely to increase. Scour due to combined random waves and current has been studied by e.g. Eadie and Herbich (1986). However, this research did not describe scour as a function of Kc . This has been done for the first time by Sumer and Fredsøe (2001). For different combinations of waves and currents they performed laboratory experiments. The relative strength of the current is described by a dimensionless parameter U_{cw}^*

$$U_{cw}^* = \frac{U_c}{U_c + U_w}$$

In their experiments they found that the equilibrium scour depth can be well predicted by only U_{cw}^* and Kc . The results are plotted in figure 9.

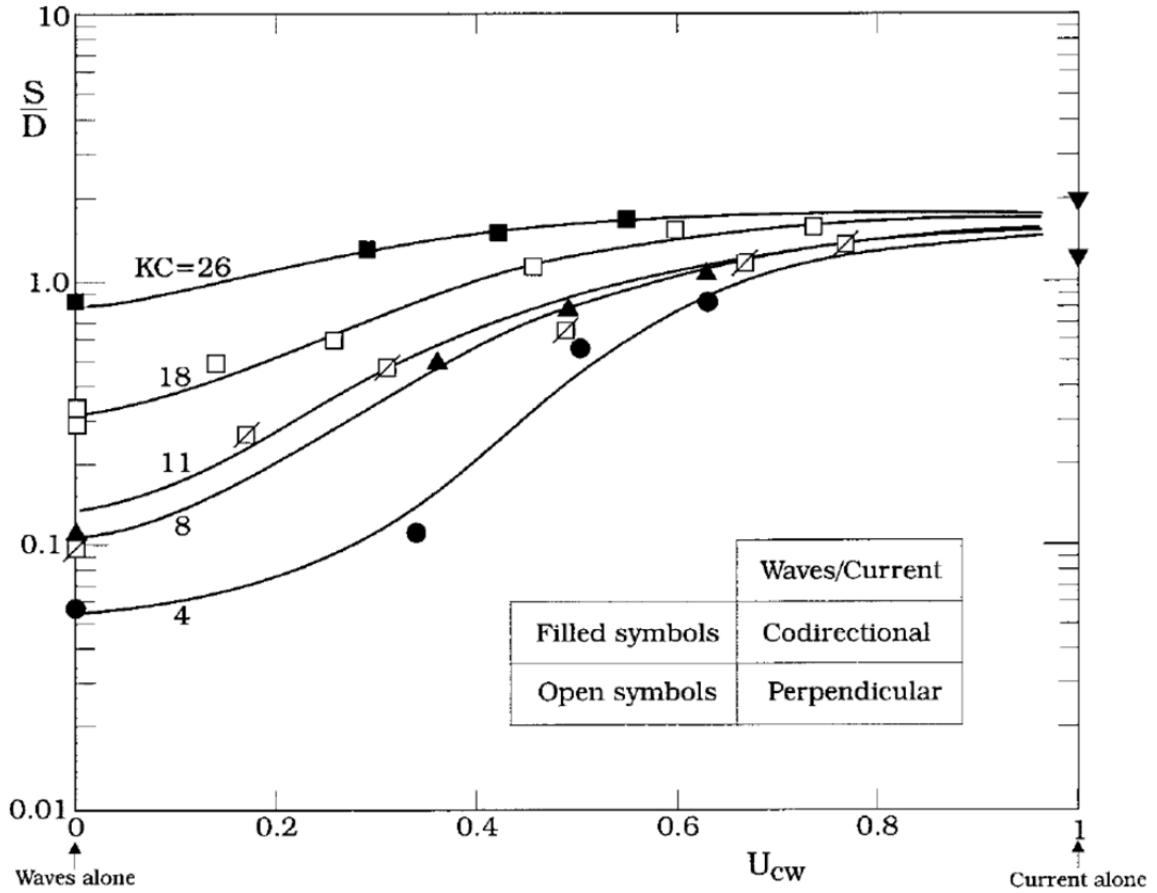


Figure 9: Equilibrium scour depth for waves and currents under live-bed conditions (from Sumer et al., 2001)

2.4.2 Equilibrium scour depth

As an effect of the flow pattern as described in the foregoing section, a scour hole grows till it reaches an equilibrium after sufficiently long time of steady current or waves. For a circular foundation pile these processes are influenced by a number of factors. For steady currents the most important ones are the Shields parameter, the sediment gradation, the depth of the boundary layer and the sediment grain size with respect to the pile size.

Scour caused by waves is mainly governed by the Kc number, since this represents the relative importance of inertial effects. Additional influences include the cross-section of the pile and the value of the shields parameter if $\theta < \theta_{cr}$. Reference is made to Sumer et al. (2002a) for further details on the various parameters on wave-induced scour, since it is considered to fall beyond the scope of this report.

For current-induced scour the influence of the Shields parameter θ is very pronounced, since it is a non-dimensional form of the bed shear stress, which is the driving force behind bed particle movement. This quantity determines directly whether it is a clear-water condition or a live-bed condition. This has been shown by Melville and Coleman (2000). From figure 10 it can be derived that there are two flow velocities at which the scour depth is at its maximum. Note that the scour depth S is expressed in a non-dimensional way, since it is divided by the pile diameter D . The first peak is at the transition from clear-water to live-bed conditions. The second peak is at the transition

from a bed with dunes to a bed where these sand dunes have been washed away. These peaks are referred to as the threshold peak and the live-bed peak respectively. Furthermore, the figure shows the effect of sediment non-uniformity. Armouring occurs in non-uniform sediment, so small particles may shelter behind the larger ones and larger particles are exposed by the smaller ones. Therefore, the threshold peak shifts to slightly higher flow velocities and the scour depth is lower (Melville et al., 2000).

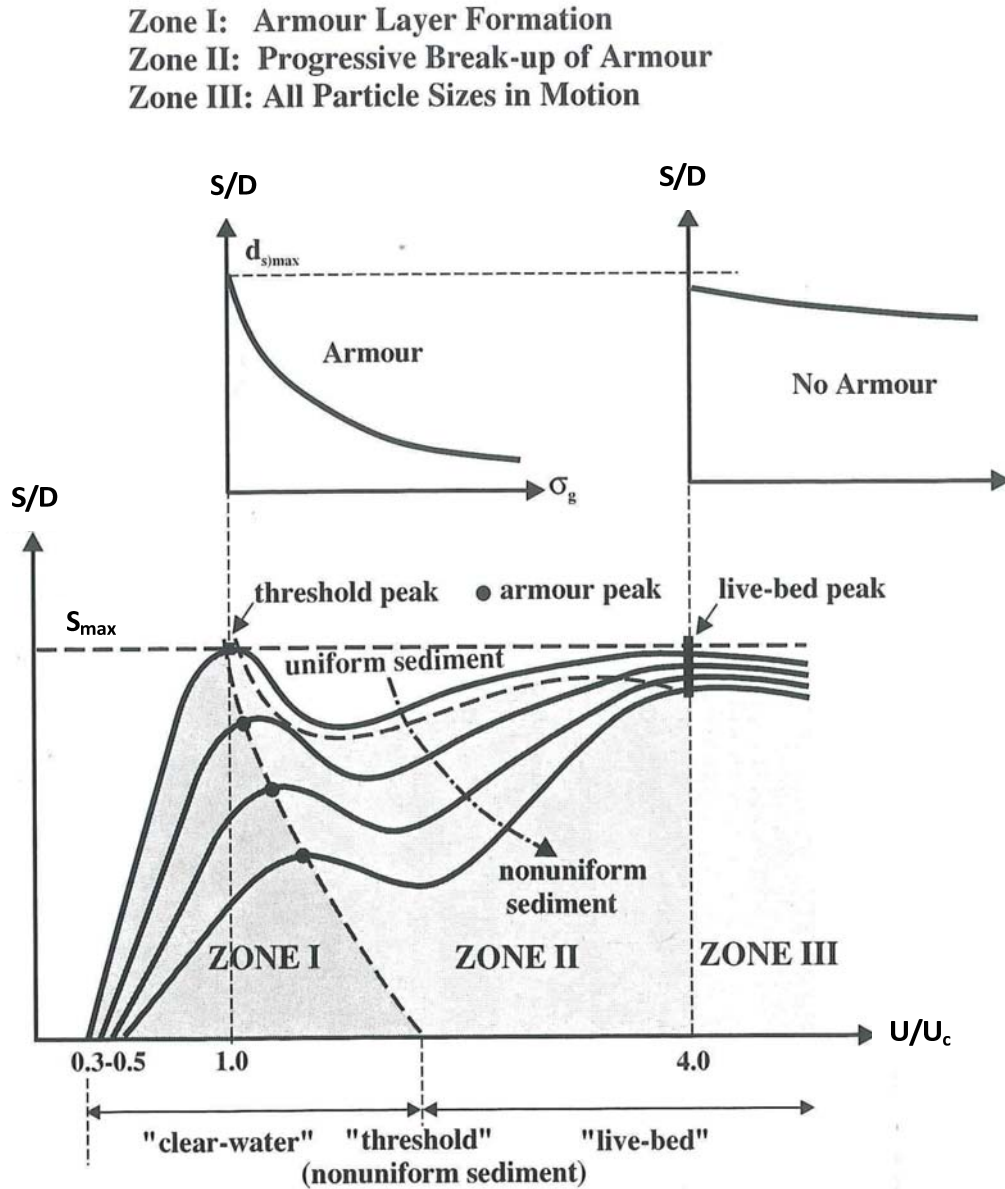


Figure 10: Local scour depth variation for different flow velocity and different sediment uniformity (from Melville et al., 2000).

The effect of the boundary layer thickness δ , expressed in a non-dimensional way δ / D , is considered as an important parameter, since it determines the location of the separation point of the horseshoe vortex (Baker, 1980). The effect on scour is such that when the boundary layer thickness is small compared to the pile diameter, the scour depth is reduced compared to a certain reference scour depth, as can be seen from figure 11. For $\delta / D > 3$ no reduction is present (Melville and Sutherland, 1988).

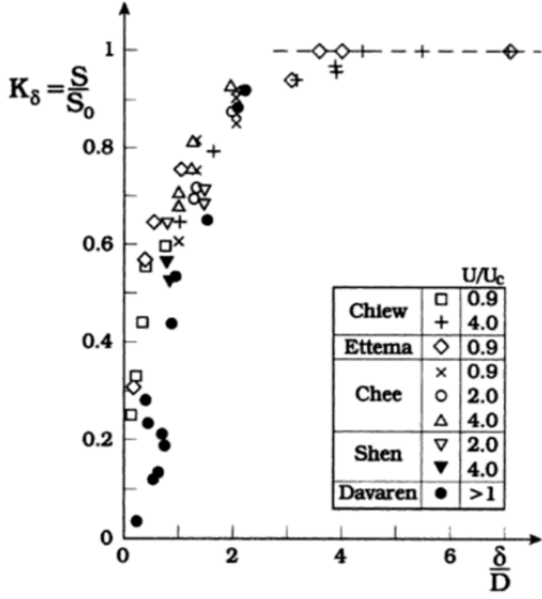


Figure 11: Effect of boundary-layer thickness (from Sumer and Fredsøe, 2002) where data where compiled by Melville et al. (1988).

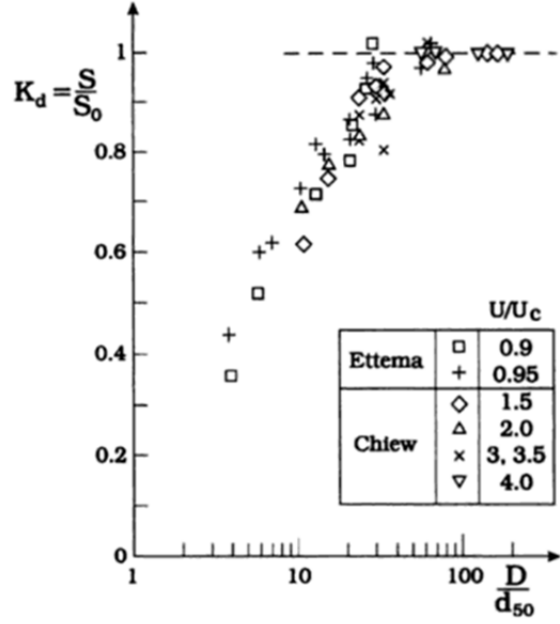


Figure 12: Effect of sediment size (from Sumer and Fredsøe, 2002) where data where compiled by Melville et al. (1988).

Finally the sediment grain size has an important influence. Larger median grain sizes compared to the pile diameter reduces the scour depth as can be seen from figure 12. The behaviour is different for cohesive sediment (Sumer and Fredsøe, 2002). Then the forces that are resisting motion include not only those associated with particle geometry, but also electrochemical forces from clay particles, which bind the material together (Knighton, 1988).

For current induced scour the dimensionless scour depth is estimated by Melville et al. (1988) through

$$\frac{S}{D} = K_I K_\delta K_d K_s K_\alpha$$

Here K_I is the flow intensity factor

$$K_I = \begin{cases} 2.4 & \text{for } \frac{U - U_a - U_{cr}}{U_{cr}} > 1 \\ 2.4 \left| \frac{U - U_a - U_{cr}}{U_{cr}} \right| & \text{for } \frac{U - U_a - U_{cr}}{U_{cr}} \leq 1 \end{cases}$$

K_s is the shape factor, where $K_s = 1$ for circular cross-sections. K_δ and K_d are factors reflecting the influence of the boundary-layer thickness and median grain size respectively. K_α is the alignment factor in case the cross-section is rectangular. For circular cross-sections this is $K_\alpha = 1$. More details on these factors can be found in Melville et al., (1988). U_a is the armouring peak velocity and in an uniform sediment $U_a = U_{cr}$. It should be noted here that the effects as shown in figure 10 till 12 are not reflected in the relations for waves from Sumer et al. (2002).

2.4.3 Time-bound behaviour of scour

So far the focus has been the maximum scour depth. Another aspect of scour is the time scale in which it develops. The largest scour depths generally occur under action of current, but Høgendal et al. (2005) show that the timescale for only current is generally much larger than for only waves. Furthermore, the equilibrium scour depth may be calculated for extreme hydraulic conditions, but if these conditions last for only a short moment, this equilibrium may not be reached and may partially be filled again.

The timescale of wave-induced scour and current-induced scour under live-bed conditions has been investigated by Sumer et al. (1992b). They found that under constant conditions the scour depth behaves according to the solution to a relaxation problem, where the actual scour depth $S_a(t)$ is converging exponentially to the equilibrium scour depth. The scour at a certain moment of time t may be approximated by the following relationship.

$$S_a(t) = S + (S_a(0) - S) \exp\left(-\frac{t}{T(S_a)}\right)$$

Here S is the equilibrium scour depth under the present hydrodynamic conditions and $S_a(0)$ is the actual scour depth at $t=0$. Note that backfilling occurs when the actual scour is larger than the equilibrium scour depth corresponding to the applied hydrodynamic conditions. Since the time scale of scouring and backfilling are different, the time scale T depends on the actual scour depth. It can be brought into its dimensionless form T^* by

$$T^* = \frac{\sqrt{g(\rho_s / \rho - 1)d^3}}{D^2} T$$

Where ρ_s and ρ are the density of bed material and water respectively, d is the sediment grain size and g is the acceleration due to gravity. The non-linear time behaviour can be expressed mathematically with

$$T^* = \begin{cases} T_s^* & \text{for } S_a \leq S \\ T_b^* & \text{for } S_a > S \end{cases}$$

Investigation of the time development of a scour hole often comprises the determination of T_s^* for scour and T_b^* for backfilling. The time scale can be predicted from the scour depth time series by calculating the slope of the tangent line to $S_a(t)$ curve at $t=0$ (Sumer et al., 1992b).

For a steady current the time scale has been found to depend on the dimensionless boundary layer thickness δ/D and shields parameter θ .

$$T_c^* = \frac{1}{2000} \frac{\delta}{D} \theta^{-2.2}$$

For waves this is found to be

$$T_w^* = 10^{-6} \left(\frac{Kc}{\theta} \right)^3$$

Both relations have been based on best fits to experimental data (Sumer et al., 1992b).

Raaijmakers et al. (2008) used different relations for the time scale however. For current-dominated scour they found

$$T_c = c_1 \frac{D^2}{\bar{U}^3} K_{mob}$$

While for wave-dominated scour they found

$$T_w = c_1 \frac{D^2}{U_w^3} K_{mob}$$

Where $K_{mob} = 1 + \frac{10}{(\theta / \theta_{cr})^2}$, $c_1 = 1000 \text{ m/s}^2$ \bar{U} is the depth-averaged current velocity and

U_w is the amplitude of the orbital velocity at the seabed.

Finally, the effect of time on the scour hole under clear-water conditions is given by Melville and Chiew (1999). The equilibrium scour depth is multiplied by a time factor K_t given by

$$K_t = \exp \left(-0.03 \left| \frac{\bar{U}}{\bar{U}_{cr}} \ln \left(\frac{t}{t_e} \right) \right|^{1.6} \right)$$

The time it takes to attain the equilibrium scour depth is found to be

$$t_e (\text{days}) = \begin{cases} 48.26 \frac{D}{\bar{U}} \left(\frac{\bar{U}}{\bar{U}_{cr}} - 0.4 \right) & \text{for } \frac{h_w}{D} > 6, \frac{\bar{U}}{\bar{U}_{cr}} > 0.4 \\ 48.26 \frac{D}{\bar{U}} \left(\frac{\bar{U}}{\bar{U}_{cr}} - 0.4 \right) \left(\frac{h_w}{D} \right)^{0.25} & \text{for } \frac{h_w}{D} \leq 6, \frac{\bar{U}}{\bar{U}_{cr}} > 0.4 \end{cases}$$

Here D , \bar{U} and \bar{U}_{cr} are expressed in m and m/s.

For combined waves and current it is much more difficult to give a proper relationship. Such a relationship has to be based on a large number of experiments, because it varies with a number of variables, namely U_{cw}^* , θ_w and Kc . Petersen et al. (2012) concluded that compared to the wave only case, a small additional current ($0 < U_{cw}^* < 0.3$) leads to an increased timescale, since the equilibrium scour depth is larger and more sediment needs to be eroded. Furthermore, vortex shedding on the upstream side in waves is

slightly limited by the presence of a current. When $0.3 < U_{cw}^* < 0.5$ the timescale is fairly constant, while for $U_{cw}^* > 0.5$ the time scale decreases again, since it starts to be a more current-dominated situation. Their results are shown in figure 13. More measurements are necessary to confirm the drawn conclusions from these figures.

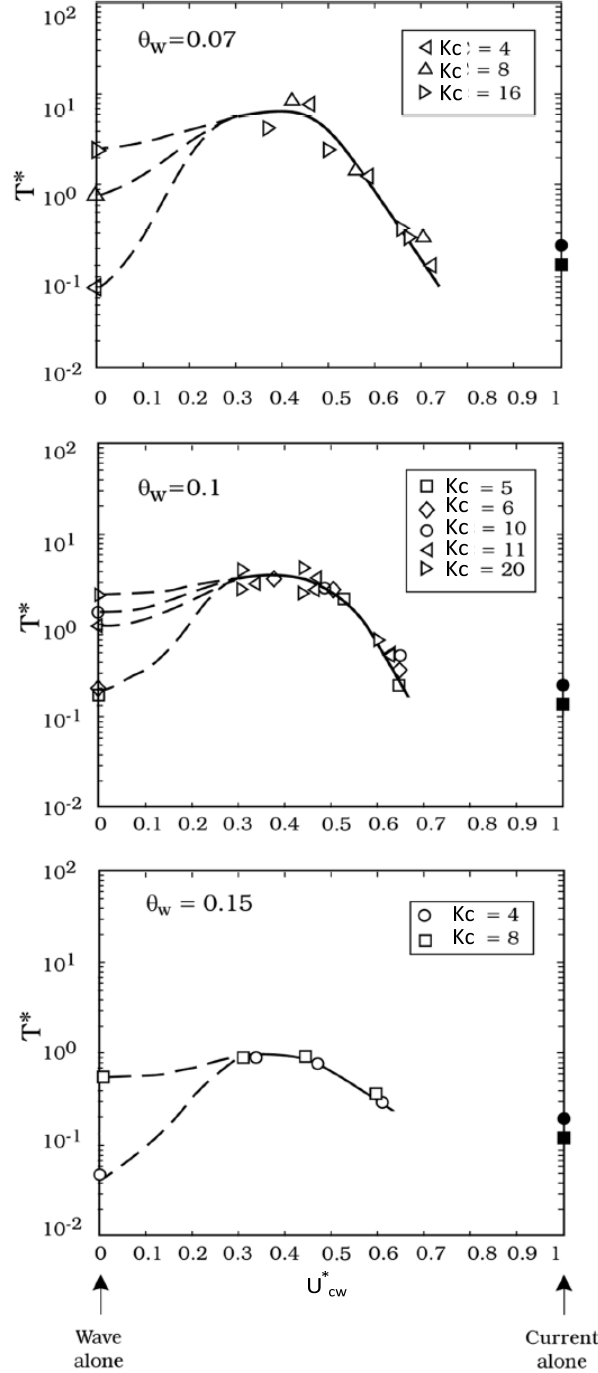


Figure 13: Time scale of scour around a circular cylinder in combined current and waves. (Current only tests ■ and • had conditions $\delta / D = 2.7$, $\theta = 0.13$) (obtained from Petersen et al., 2012)

Part of the time development in the field is backfilling, which take place when the hydraulic conditions are such that the equilibrium scour depth is smaller than the actual depth. Then sediment is deposited in the scour hole. Hartvig et al. (2010) found an exponential behaviour, not only when a scour hole forms, but also when backfilling takes

place. They showed that backfilling is approximately 10 times slower than scouring. Furthermore, they concluded that regardless of the time, the slope of the scour hole remains constant.

2.4.4 Shape of scour hole

Another feature of a scour hole is its shape. Nielsen and Hansen (2007) use three scour widths $w_{upstream}$, $w_{downstream}$ and w_{side} together with the scour depth to characterise the shape of the scour hole. These are the width upstream, downstream and at the sides as a result of symmetry on width perpendicular to the flow direction. This is shown in figure 14. This approach has been used by e.g. Harris et al., (2010) to describe the shape of the scour hole in time.

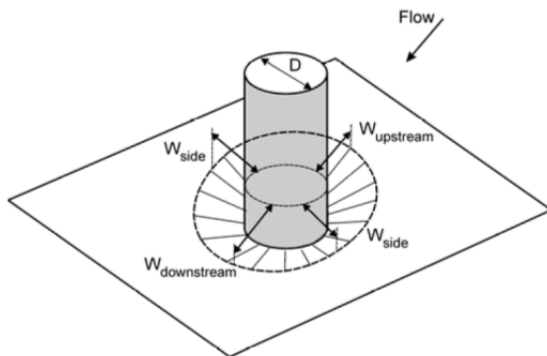


Figure 14: Definition of scour width (from Nielsen et al., 2007)

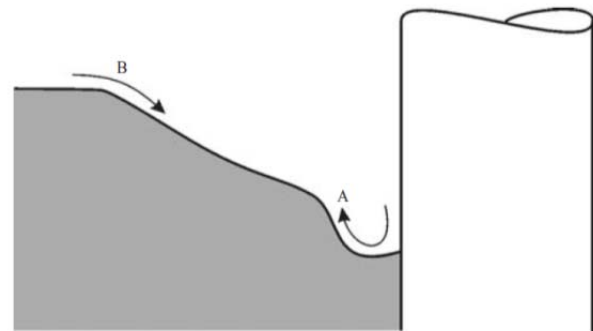


Figure 15: Balance of A: erosion of the foot of the upstream slope and B: Continuous supply of sediment by sliding of slope (from Roulund et al., 2005)

For current-induced scour the upstream width is found to be smaller than the downstream width and the scour hole is deeper on the upstream side, implying the upstream slope is steeper. As soon as the scour hole has developed around the entire pile perimeter, the angle of the upstream slope remains nearly constant. The downstream angle may vary more, but it is frequently assumed constant (Hartvig et al., 2010). This can be up to half the angle. This corresponds to a balance between supply and erosion. Sediment supply mainly comes from sediment sliding since the slope exceeds the angle of repose. The horseshoe vortex tends to push up sediment from the foot of the upstream slope first and after which it is moved side wards and removed from the scour hole (Roulund et al., 2005). This is illustrated in figure 15.

Downstream from the hole sand is deposited and a bar is formed. It depends on the ambient bed conditions till what extent the disturbed flow is able to further rework this sediment and consequently how large a possible bar can grow (Roulund et al., 2005).

For clear-water scour the shape of the hole is strongly formed by the shape of the horseshoe vortex, see figure 7. Reference is made to Khwairakpam et al. (2012) and Hartvig et al. (2010) for further information.

2.5 Theory on liquefaction

Soil liquefaction is a process which is closely related to scour. A liquefied bed behaves as if it were a liquid with different properties than water and has barely any shear strength. Consequently, bed forms strongly depend on the flow pattern and the capacity of the soil to support vertical or horizontal load is lost (Whitehouse, 1998). Denoting the

excess pore water pressure at time t and vertical location in the bed z as $u_e(z, t)$ and the vertical effective stress as $\sigma_v'(z, t)$, the criterion for liquefaction can be expressed as (Zen and Yamazaki, 1993):

$$\sigma_v'(v, 0) \leq u_e(z, t)$$

Or alternatively

$$\sigma_v(v, t) \leq u(z, t)$$

Where σ_v is the total vertical soil stress and u is the total pore water pressure.

Two types of liquefaction can be distinguished, namely:

1. Momentary liquefaction, which is an upward force from excess pore water under a single wave trough.
2. Residual liquefaction, where pore pressure is built up by cyclic loading.

Further distinctions can be made on the type of conditions (de Groot, 2006):

- Normal or shear loading
- Easy drainage to no drainage
- Soil properties like the relative soil density or gas content

The mechanics behind residual and momentary liquefaction are discussed below in section 2.5.1 and 2.5.2 respectively.

2.5.1 Momentary liquefaction

Momentary liquefaction is caused by the passage of a large single wave and involves cohesionless material with a larger permeability than residual liquefaction. Under the wave crest the pore pressure in the soil builds up, while under the wave trough the water flows out of the soil. Under the outflow there is a negative pore pressure gradient in the soil. When the soil is fully saturated the pressure gradient in the soil will not be enough to move particles. However, when the water contains some trapped air bubbles, even when the air content is less than 1%, the pore water combined with the air act as being compressible. Consequently, the pore water dissipates much faster with the depth and has a much higher gradient at the top layer of the soil. The difference in pore water pressure distribution is illustrated in figure 16. A substantial lift force is present and can exceed the submerged weight of the soil in case of liquefaction, as is clarified in figure 17 (Sumer et al., 2002a; Groot et al., 2006).

For momentary liquefaction Sakai et al. (1992) state that it is difficult to reproduce in a small size experiment. Experiments have been performed successfully though by Zen et al. (1993). In a tower of a few meters high filled with sand they measured the pore water pressure at a number of heights. Wave passing was simulated by artificially adding pressure at the top of the apparatus.

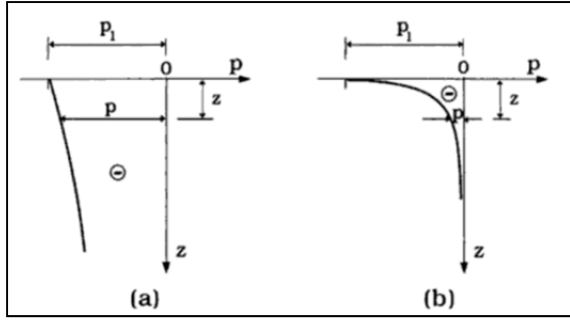


Figure 16: Pore pressure for a) fully saturated sea bed soil and b) a not saturated soil (from Sumer and Fredsøe, 2002a)

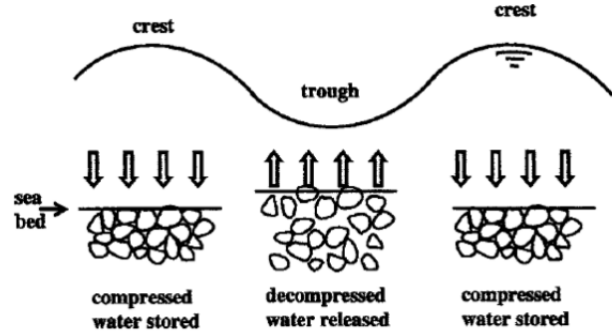


Figure 17: Schematised momentary liquefaction under a single wave (from Groot et al., 2006)

2.5.2 Residual liquefaction

For a pressure variation, for example caused by waves or earthquakes, the pressure between grains alternates continuously. Under a wave cycle the soil may not be able to fully dissipate its excess pressure built-up under the crest. Therefore the pore water pressure is able to build up gradually. After a number of waves it may happen that the accumulated pressure is high enough to exceed the value of the overburden pressure. Then soil grains become unbounded and start acting as a liquid. Among others this can be caused by the following phenomena (Sumer and Fredsøe, 2002a):

- Waves above relatively uncompacted soils
- Earthquakes
- Shocks (for instance from slope failure)
- Rocking of a structure.

After the liquefaction takes place, the pore water pressure gradually decreases, because the pore water slowly flows out of the soil. Finally, the accumulated excess pore water pressure converges to zero again, as is shown by Sumer et al. (1999) and Sumer et al. (2006). This is accompanied with compaction of the soil.

Earlier laboratory experiments have been used to reproduce residual liquefaction by earthquake events e.g. by Seed et al. (1983) and Steedman (1998). When a structure is built on soils that are susceptible for liquefaction induced by earthquakes, it can be tested whether additional measures are required. This is done with a factor of safety (FS) by comparing the Cyclic Resistance Ratio (CRR) with the Cyclic Stress Ratio (CSR).

$$FS = \frac{CRR}{CSR}$$

Generally FS should be higher than 1.0 to avoid liquefaction, though also with the factor of safety slightly higher than 1.0, the soils may liquefy under certain conditions. For FS much higher than 1.0, the soil can be expected to have enough resistance against liquefaction. For earthquakes the cyclic stress ratio is defined as the uniform cyclic shear stress amplitude divided by the vertical effective stress. Consequently this quantity is based on the local loading (the acceleration for earthquakes) and other local field conditions, like water height and soil type. The Cyclic Resistance Ratio is derived from standard penetration tests (Seed et al., 1983; Day, 2002). No design methods are known to the author on the cyclic stress by structural displacements.

Furthermore, wave-induced liquefaction was seen in the study of Sumer et al. (1999) and Sumer et al. (2006). In their studies waves were applied in a flume in which a part was filled with sand. They described the time development of liquefaction which developed under the waves. The results are shown schematically in figure 16. Note that this is at one particular depth in the sediment. Because the period averaged excess pore pressure \bar{u}_e needs to build up, liquefaction does not take place directly but after a number of waves (see part A of figure 18).

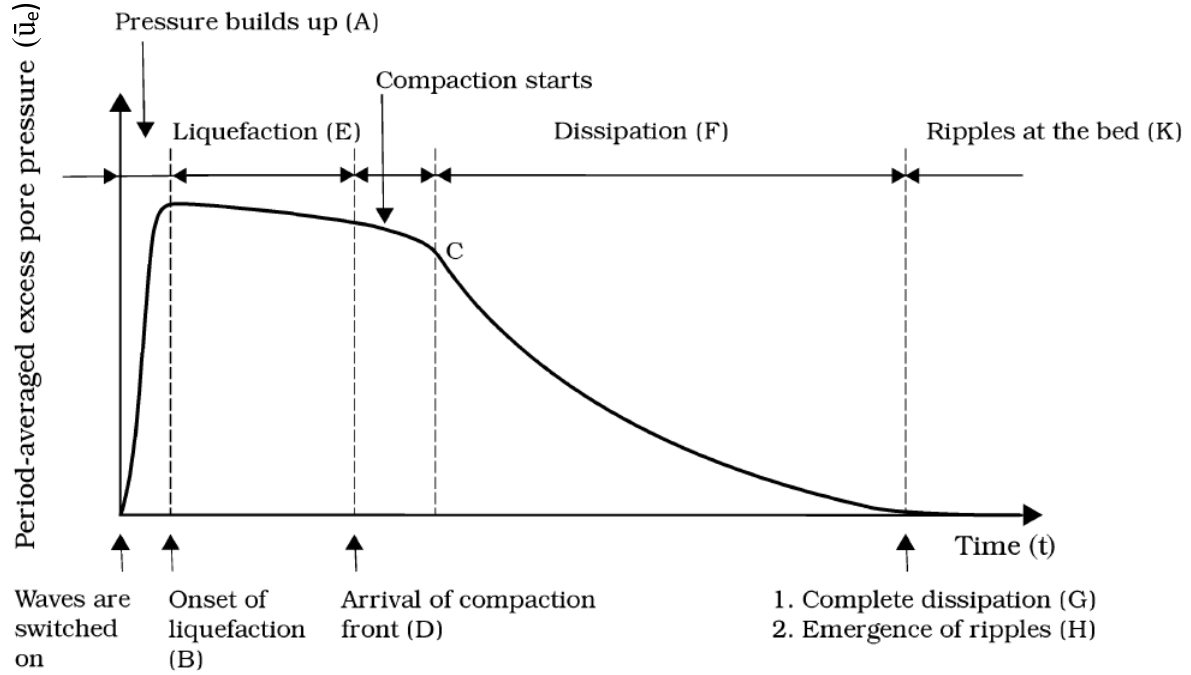


Figure 18: Time development of wave-induced liquefaction (from Sumer et al., 2006)

This pressure increase was found in flume experiments by Sumer et al. (1999) and is shown for waves with $H = 16.6$ cm in figure 19. Note that the excess pore water pressure \bar{u}_e is divided by the volumetric weight of water γ_w so that is expressed as centimetre water column. Liquefaction starts at the top of the bed and continues to move downwards up to a certain maximum depth. As soon as liquefaction starts at a certain depth, the excess pore pressure cannot further increase there (part E of figure 18 and figure 20).

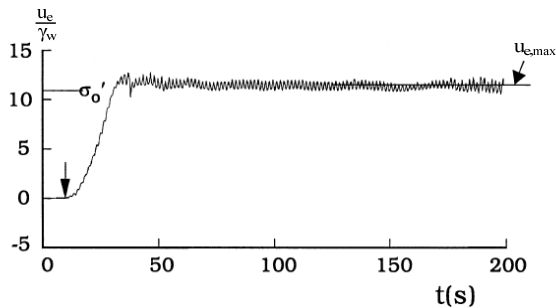


Figure 19: Build-up of pore water pressure for wave height $H = 16.6$ cm (from Sumer et al., 1999)

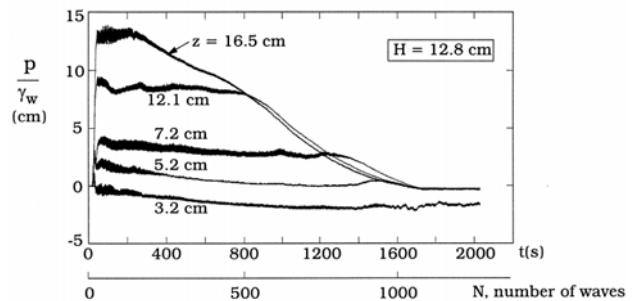


Figure 20: Behaviour of pore water pressure after a long time (from Sumer et al., 1999)

Next, the soil starts to compact. This goes as a front through the soil, going in upward direction and is referred to as the compaction front. As soon as this front passes the point

for which the graph is taken, the excess pore water pressure starts to dissipate (part F of figure 18). When the excess pore pressure has dissipated completely and the compaction front has reached the bed level, ripples start to emerge, eventually attaining the equilibrium state corresponding to the wave conditions (part K of figure 18) (Sumer et al., 2006).

Unless the soil is softened again, this type of liquefaction does not occur again for the same load. For storm events with larger waves it might happen again since the soil may further compact. Normally the sea bed has a long history of wave exposure, so it is not likely this process happens on an undisturbed bed (Sumer and Fredsøe, 2002a). However, recently deposited sediment will be susceptible for liquefaction and easily comes in motion again (Geremew, 2011). Because the pore pressure should be able to build up without flowing out of the soil directly, this kind of liquefaction mainly occurs at soils with intermediate permeability, e.g. fine sand or silt. Furthermore the frequency of loading should be sufficiently high (Sumer and Fredsøe, 2002)

Liquefaction has been combined with scour in one experiment by Sumer et al. (2007). Here finer sediment was used than before in scour experiments (e.g. Sumer et al., 1992; Sumer et al., 2001). Therefore, the soil started to liquefy after the wave start to run over the soil. An important conclusion was that as long as the soil was liquefied, no scour developed. The compaction had effect on the equilibrium scour depth, since compaction led to increased equilibrium scour depth. The increased relative soil density leads to increased angle of repose, which can explain this increase only partially. Local disturbance of the soil, for example by drilling the pile in the compacted bed, did not seem to have a role on the equilibrium scour depth (Sumer et al., 2007).

2.6 Conclusion

When a slender monopile is placed in a marine or fluvial environment, both horseshoe and lee-wake vortices arise originating from waves and currents. These vortices are in addition to flow contraction which always takes place due to the separation of flow. As a consequence the shear stress increases locally. When the critical shear stress is exceeded, additional erosion takes place and a scour hole forms. The description of scour falls apart in the quantification of the equilibrium depth, time scale and shape of the scour hole. Generally the quantification of these is based on scaled laboratory experiments. In the field a number of other processes play a role and the combination of processes may give different behaviour. This includes the difficulties with scaling from small scale laboratory experiments to prototype dimensions. Large safety margins are used to cope with this uncertainty.

The combination of scour and liquefaction has so far rarely been investigated. The same waves that are causing scour, can also cause liquefaction. Apart from waves, scour can be caused by structural motions and earthquakes. Depending on the hydrodynamic and geotechnical circumstances this can be both residual liquefaction and momentary liquefaction. Scour around a monopile and liquefaction has been shown in one experiment by Sumer et al. (2007). They concluded that a scour hole would only develop after the excess pore water pressure was dissipated such that liquefaction was not present anymore. On the other hand Whitehouse (1998) stated that since a liquefied soil has lost most of its shear strength, the soil can be eroded more easily. More research on the effects on scour should provide more certainty in the design of offshore wind turbine foundations.

3. Field characteristics

In this chapter reference is made to the conditions that are present in the field. The field conditions related to hydrodynamics, sediment and wind strongly vary among different wind farms. This is illustrated by Whitehouse et al., (2011), who collected the field conditions among various offshore wind farms. An overview of the sites they considered is given in table 1. For each site a description is given of the seabed, the hydrodynamic conditions and the resulting scour depth.

Table 1: Site characteristics (after Whitehouse et al., 2011)

Site	Description	Seabed sediment	Monopile diameter [m]	Scour protection	Depth LAT [m]	Mean tide level above LAT [m]	Tide range (n) neap and (s) spring [m]	Peak current speed [m/s]	Annual significant wave height [m]	Max. dim.less scour depth [-]
Scroby Sands OWF	Sand bank, east coast England: exposed to waves, strong currents, fine to medium sand, dynamic stand bank environment, shallow water, presence of mobile bedforms	Medium SAND, some GRAVEL/SHELL, CLAY at depth	4.2	Yes**	3-12	1.6	1.1 (n) 1.9 (s)	1.65	1 - 3.5****	1.38
Arklow Bank OWF	Sand bank, east coast, Ireland: exposed to waves, strong currents, sand/gravel, dynamic seabed environment, shallow water	Loose to medium dense SAND and sandy GRAVEL	5	Yes	2-6	1.3	1 (n) 2 (s)	2	5.6****	0.8
N7	Open seabed, southern North Sea: exposed to waves, moderate currents, medium sand, dynamic seabed environment, shallow water	Fine medium dense SAND	6	No	5.2	1.8***	2.6 (mean)	0.75	1.1	1.05
Scarweather Sands	Sand bank, Bristol Channel: exposed to waves, strong currents, medium sand, dynamic seabed environment, shallow water	Medium to fine shelly SAND	2.2	No	6	5.4	4.2 (n) 8.9 (s)	1.1	2.8	0.59
Otsumer Balje inlet	Tidal inlet, Wadden Sea: sheltered from waves, moderate currents, fine sand, dynamic seabed environment, very shallow water	Medium SAND	1.5	No	11.7	1.6	2.6 (mean)	1.4	Sheltered	1.47
Destin Inlet	Tidal inlet Gulf of Mexico: sheltered from waves, moderate currents, fine sand, dynamic seabed environment, very shallow water	Fine SAND	0.61*	No	3.8	0	0.2 (approx)	0.6	Sheltered	1.83
Barrow OWF	Open seabed, northwest coast of England: exposed to waves, moderate currents, sand and clay, stable seabed environment, deep water	Fine SAND to muddy SAND, some Gravels overlying CLAY; exposed CLAY	4.75	No	12-18	5.1	4.1 (n) 8.2 (s)	0.8	4.9	0.04-1.21
Kentish Flats OWF	Open seabed Thames Estuary, England: exposed to waves, moderate currents, sand and clay, stable seabed environment, very shallow water	Fine SAND; infilled paleo-channel with CLAYS and SANDS; CLAY near surface or exposed	5	No	3-5	2.74	2.9 (n) 4.7 (s)	0.9	3.3****	0.46
North Hoyle OWF	Open seabed, north Wales: exposed to waves, moderate currents, gravel/sandy gravel, stable seabed environment, deep water	Gravelly medium SAND or sandy GRAVEL overlying CLAY	4	No	6-12	5.15	4.1 (n) 6.1 (s)	1.17	4.9	0.125
Egmond aan Zee OWF*****	Open seabed, Southern North Sea: exposed to waves, moderate currents, medium sand, dynamic seabed environment	Medium Sand	2.9*****	No	16-20	-	2.4 (mean)	1.2	-	0.79*****

- * Square pile
- ** First survey without scour protection
- *** Mean Sea Level value
- **** Breaking waves
- ***** From Fischer et al. (2010), Louwersheim et al., (2007)
- ***** For measuring mast

Around the monopiles scour take place as a consequence of the disturbed water flow pattern around the foundation. From the collected field measurements it can be concluded that the scour is especially deep at sites with a strong tidal current and abundance of waves, like the Ozumer Balje inlet and Destin inlet. Furthermore clay influenced sites, like Barrow, Kentish flats or North Hoyle show a decrease in scour depth. Even within a wind farm the conditions can strongly vary, for example by the presence of clay.

Raaijmakers et al. (2013) predicted the dimensionless scour depth in the southern North Sea that would develop without scour protection. This is based on metocean data. The 95% non-exceedance values are given in figure 21. This calculation assumes a uniform non-cohesive soil, so based on the fraction of cohesive material, the dimensionless scour depth is overpredicted. The feasibility of a foundation without scour protection depends on the additional steel costs of increased foundation length and the costs of scour

protection. Raaijmakers et al. (2013) concluded that it turns out to be cost-efficient to omit scour protection at sites with a relatively low current velocities and larger waves. This is for example the case at the Doggersbank, the northern part of the German EEZ and at the Baltic Sea. In the south western part of the North Sea scour protection is more cost efficient.

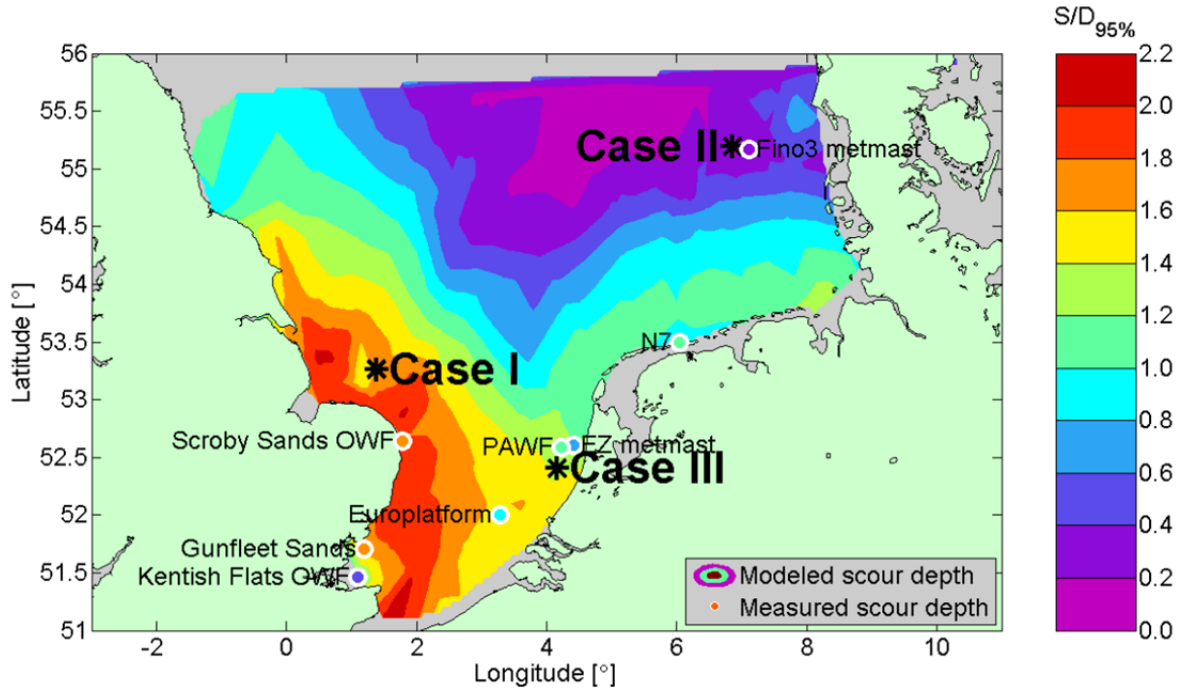


Figure 21: Prediction of the 95% non-exceedance values of the dimensionless scour depth in the southern part of the North Sea (assuming $D = 5$ m and $d = 200\mu\text{m}$) (from Raaijmakers et al., 2013)

OWEZ is one of the largest Dutch wind farms. The construction of this wind farm was accompanied with a large field measurement programme intended for research purposes. Based on the data that was measured, design values for the field characteristics have been obtained. A summary of the data on this wind farm is given in table 2.

Table 2: Field characteristics at OWEZ

Water height to MSL	h_w	21.4	m	Fischer et al. (2010)
Significant wave height (return period of 1 year)	H_s	6.06	m	Fischer et al. (2010)
Significant wave height (return period of 100 year)	H_s	8.41	m	Fischer et al. (2010)
Wave period (return period of 1 year)	T_p	9.7	s	Fischer et al. (2010)
Wave period (return period of 100 year)	T_p	11.6	s	Fischer et al. (2010)
Peak current speed (normal)	U_c	0.6	m/s	Fischer et al. (2010)
Peak current speed (extreme)	U_c	1.2	m/s	Fischer et al. (2010)
Pile diameter	D	4.6	m	NoordzeeWind (2008)
Median sediment grain size	d	266	μm	Bergman et al. (2012)

4. Experimental setup

4.1 Introduction

In the presented research the effect of liquefaction on scour is examined by performing scaled experiments in a flume. Scour is chosen to be caused by a constant current in order to keep the number of influencing parameters as low as possible.

Structural vibrations can affect scour in a number of ways, for example by densification of the soil and by soil liquefaction. This research focuses on the effects of liquefaction only.

Liquefaction is generally a temporal effect. As described in section 2.5, residual liquefaction in the field can be caused by e.g. large waves, earthquakes or structural rocking. Due to movements in the sediment bed it is possible to obtain a more efficient compaction of grains. This goes at the expense of the pore volume and therefore increases the pore water pressure. If the accumulated pore water pressure exceeds the overburden pressure, the soil grains become unbounded. Consequently, the soil completely loses its strength and starts to behave as a fluid.

The above mentioned procedure is strongly time dependent and it can happen only once, since the efficiency of compaction cannot be increase endlessly. Furthermore, the development and dissipation of the increased pore water pressure take place at a different time scale compared to scour. Therefore it is chosen to create liquefaction by a constant monotonic excess pore water pressure (EPWP). Although liquefaction is normally caused by oscillating processes, this is considered to be a realistic assumption, because the oscillation of pore water pressure in the top layer of the soil is relatively small compared to the total EPWP that has been build up there. Furthermore, scour occurs at this top layer and the net effect with respect to the pore water pressure in this layer is a negative EPWP gradient. In this way it is aimed to extract the actual effect of liquefaction as much from temporal effects and effects from the relative soil density.

Five tests are performed with a different EPWP. Other conditions are kept constant and are designed to follow recommendations on an experimental setup by e.g. Whitehouse (1988). Furthermore, one reference test is performed without any EPWP to compare the actual effects. In addition, comparison can be made with other researches on current-induced scour. The scour is characterised by the equilibrium scour depth and the time in which the scour hole develops, while the applied EPWP is characterised by the difference in hydraulic head. In the experiments the EPWP is used as the only variable.

This chapter starts with an overview of the various components of the experimental setup. A number of measurements are made during the experiments. These are discussed in section 4.3. Finally, the hydrodynamic conditions are described in section 4.4. Here the performed steps during the experiment are also given.

4.2 Physical model setup

4.2.1 Flume

The experiments have been performed in a flume in the Laboratory for Fluid Mechanics at the faculty of Civil Engineering and Geosciences of the TU Delft. The flume has an

effective length of 14.30 meter, a width of 40 cm and a maximum depth of 40 cm. The flow is recirculated, so the eroded sediment is kept in the flume. The part of the flume in between two slopes is filled with sand. This part is shown in figure 22. The complete side view of the flume is shown in Appendix A.

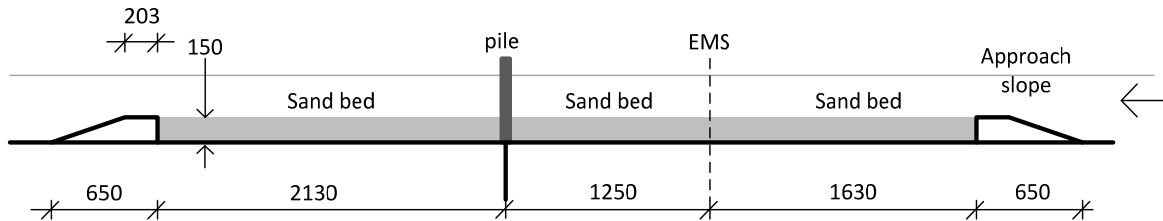


Figure 22: Geometry of sand bed flume (in mm)

In the flume an Electromagnetic flow meter (EMS) is placed upstream from the pile. Furthermore, a vertical Plexiglas pile is placed in the flume, representing a monopile foundation. The soil around the pile can be liquefied by EPWP. A porous block is installed under the pile to induce a certain overpressure evenly in the sediment. This mechanism is further elaborated in section 4.2.2. A cross-section can be drawn at the location of the pile, see figure 23.

The dimensions of the pile are based on the design considerations as mentioned in Whitehouse (1988). These are given in appendix B. Furthermore it is shown there how this resulted in the current design.

The pile is made from a Plexiglas tube with an outer diameter of 50 mm and a wall thickness of 5 mm. Consequently, the inner diameter is 40 mm. The bottom is closed with a 8 mm thick circular plate, which is glued in the tube. Furthermore, at 110 mm from the bottom of the pile a 3.5 mm thick circular plate is glued to prevent wiring from horizontal movement. The connections of the pile are glued waterproof, so the inner side is kept free from water.

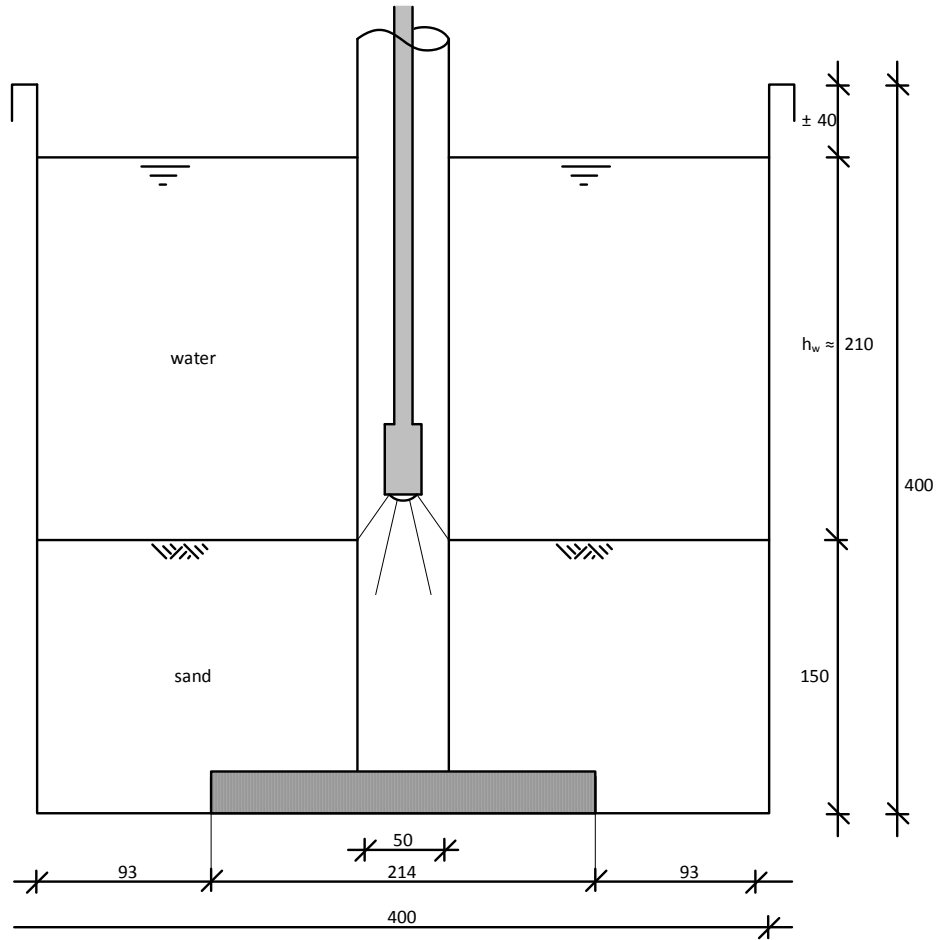


Figure 23: Cross-section at the pile, showing a Plexiglas pile placed in the sand bed (in mm)

4.2.2 Liquefaction

As stated in section 4.1, an excess pore water pressure is used to get the soil liquefied throughout the experiments. This pressure is introduced by a porous stone which is shown in figure 24.



Figure 24: Photo of porous stone

These disks are normally used to bring air into fish tanks for oxygen. The used porous stone is KOI PRO HI-OXYGEN DISK 20cm. Water is brought through a tube which is connected to the block. This tube with an inner diameter of 8 mm is attached to the bottom of the flume. The connectors had an inner diameter of 7 mm. The dimensions are shown in figure 25.

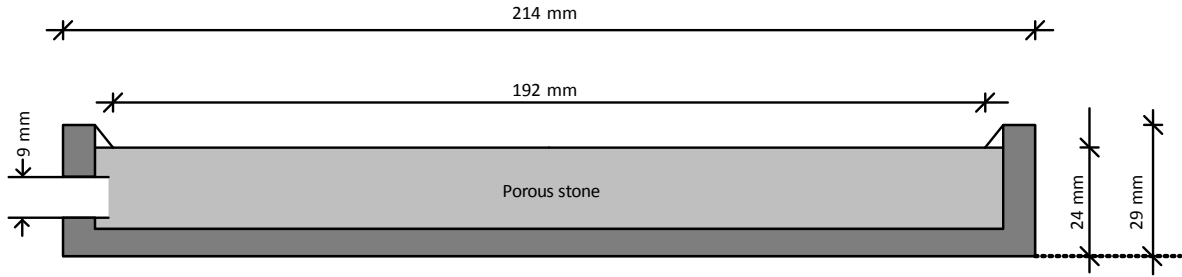


Figure 25: Dimensions porous stone

In order to test the intended way of liquefying the soil, preliminary tests are performed. The procedure and most important results of these test are given in appendix F. The preliminary tests indicated strong frictional losses in the tube connecting the porous stone with a bucket with a constant water level. Therefore the pressure in the porous stone is not equal to the pressure as applied in the bucket, as would follow from a hydrostatic calculation.

Hence the tube is split up in two just before the porous stone. One of these tubes is used to determine the “real” pressure in the porous stone. Real is quoted here, because this measurement appeared to be biased due to frictional losses in the porous stone itself as further addressed in section 6.2.4, on the functioning of the used setup. This is clarified with the sketch of the setup in figure 26. A photo of the implementation of the tubes in the flume is shown in figure 27 and 28. The hydrostatic pressure associated with the difference in water height between the bucket and the flume is denoted as $\Delta h_{p,a}$. The measured head difference just before the porous stone is denoted as $\Delta h_{p,od}$. Note that the photo differs from the schematisation, because the tubes are not installed vertically. Instead, they are installed with a small constant slope to prevent air bubbles being trapped. The tubes are installed downstream such that it has minimal influence on the water flow.

The bucket was placed on a platform installed at the top of the flume. The height of the bucket was adjusted by placing a certain number of multiplex plates underneath.

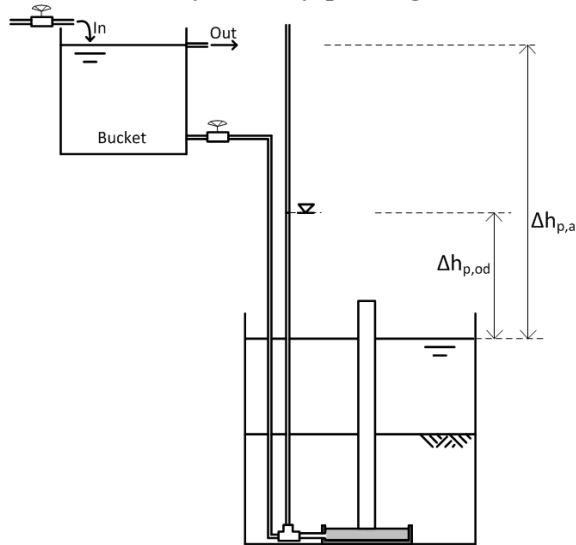


Figure 26: Schematisation of applied excess pore water pressure



Figure 27: Connection to porous stone. Note it is not connected yet and the Plexiglas pile is covered with paper for calibration purposes.



Figure 28: Photo of installation of tubes

4.2.3 Soil

Geometrically scaling the grain size would imply cohesive sediment, showing unrealistic behaviour. The decision for the grain size has been based on the usage in other experiments (e.g. Sumer et al., 2007; Qi et al., 2012; Chern and Chang, 1995). Residual liquefaction is usually investigated with relatively fine sediment, because the pore water pressure can only build up under action of waves or earthquakes when the grain size is small enough. Because of availability of sediment in the laboratory it is chosen to use sand with a median grain size of $d = 260 \mu m$. The corresponding grain size distribution is shown in figure 29. The geometric standard deviation is $\sigma_g = \sqrt{d_{84} / d_{16}} = 1.22$ (definition in accordance with Sumer et al., 2002), so the gradation is relatively steep.

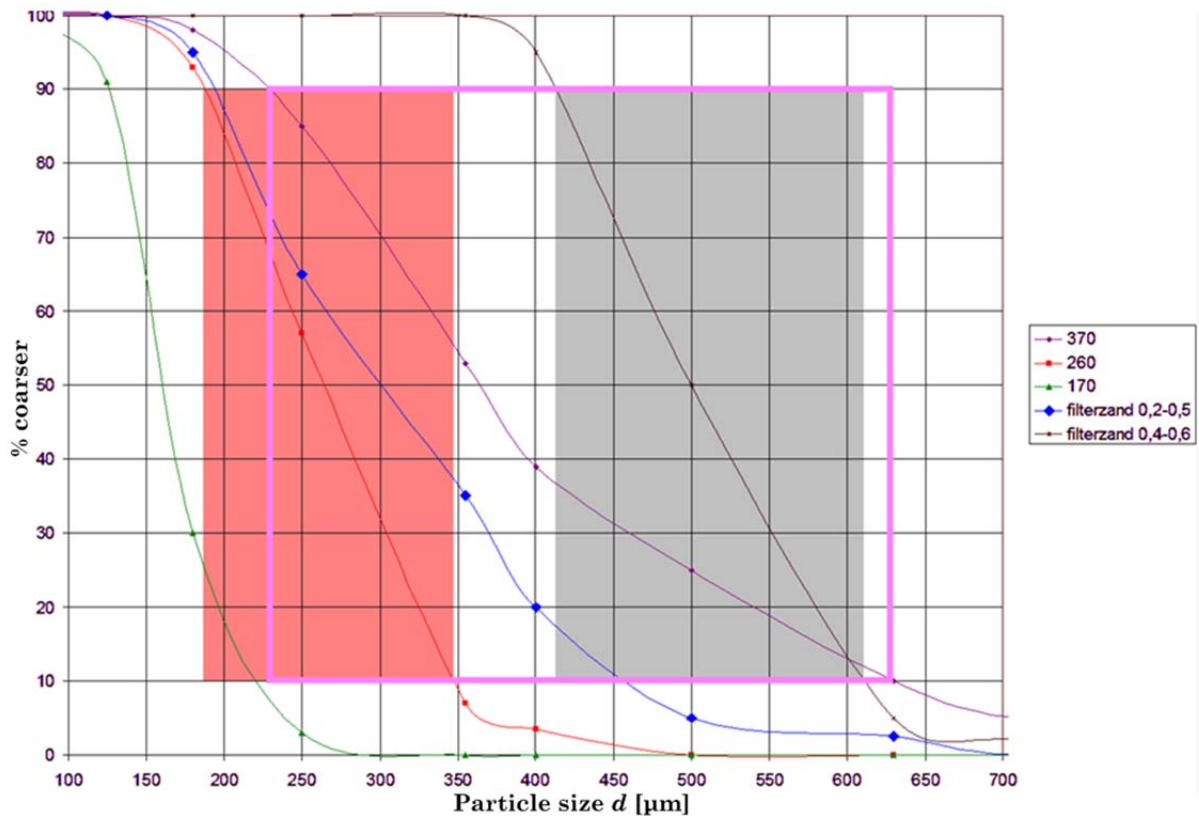


Figure 29: Particle size distribution curve. Only $d = 260 \mu m$ is used in this experiment

4.3. Measurements

4.3.1 Measurement of scour depth

The scour depth is measured by taking video images with an endoscope camera, placed inside the pile. The camera monitors the border between sand (dark on the images) and water (light) through the transparent pile. This can also be seen from the example image in figure 30.

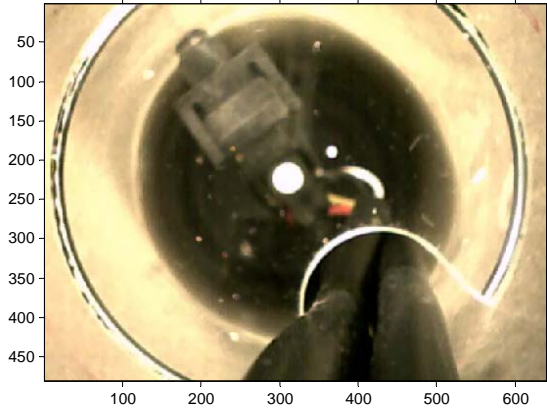


Figure 30: Example of images from endoscope camera

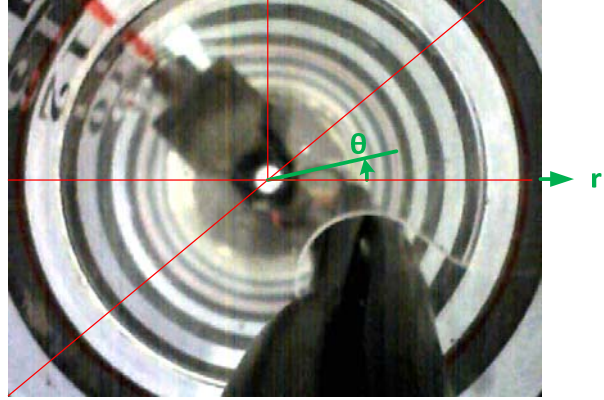


Figure 31: Image used from calibration (green: coordinate system; red: lines on which the calibration was performed)

Because the camera is fixed, the location of every pixel can be linked to a certain depth around the perimeter, so this requires calibration. Calibration is performed with a printed black white striped paper, which is attached to the pile. The vertical coordinate z_{image} in cm can now also be linked to the radius r , defined as the number of pixels from the middle of the pile to the lines in the calibration image as is shown in figure 31. Here the red lines are used for calibration and the green lines define the coordinate system. The calibration is further elaborated in appendix C.1. The result of calibration is a fourth order polynomial of z_{image} as a result of r / h_{image} , where h_{image} is the number of pixels of the image in vertical direction, so $h_{image} = 480$ pixels.

$$\frac{z_{image}}{D} = -31.8 \left(\frac{r}{h_{image}} \right)^4 + 82.9 \left(\frac{r}{h_{image}} \right)^3 - 83.2 \left(\frac{r}{h_{image}} \right)^2 + 403 \left(\frac{r}{h_{image}} \right) + 5.67$$

This relation is used to transform the detected border to the scour depth. The location of the camera is shown in figure 32. Here the height at which the camera is placed is based on the range of depths the sediment is expected to take. A best estimate of the maximum scour depth was $1.3D$, based on literature (e.g. Sumer et al., 2002; DNV, 2013).

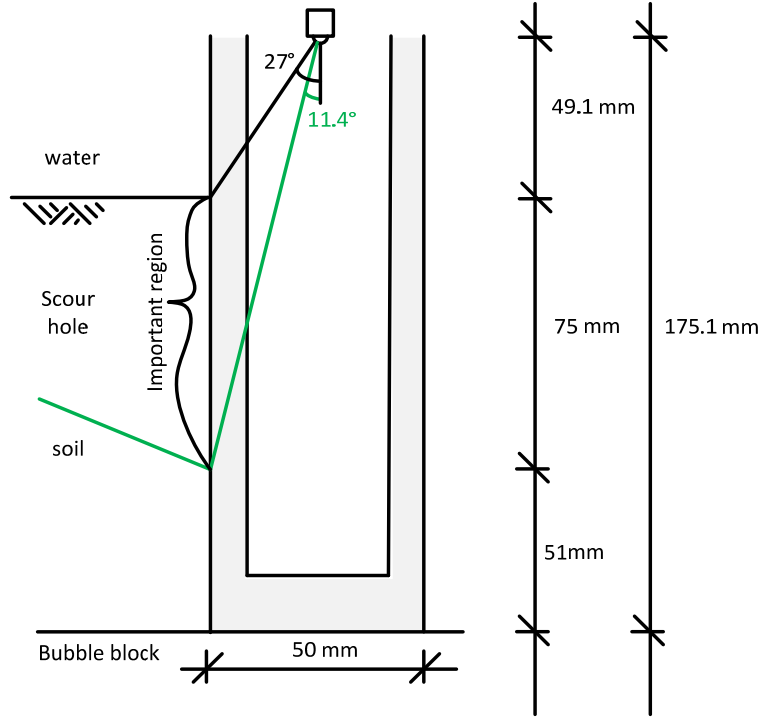


Figure 32: Visual range (green line is at maximum scour)

The middle is retrieved automatically from the images. The middle can be recognised from the white circle in the image. For every experiment the circle is determined in one photo, approximately halfway in the endoscope record. The circle is detected in the same way as the scour is obtained by only selecting a different region of interest. The centre of this area is calculated automatically.

Now from the vertical coordinate z_{image} the scour depth can be obtained by

$$S = h_{sed} - h_{od} - z_{image}$$

Where h_{sed} is the sediment height and h_{od} is the thickness of the porous stone.

4.3.2 Pore water pressure

To obtain further insight in the pressure distribution in the soil pore water pressure meters (Honeywell piezometer, type 24PCEFA6D) are installed in the wall of the pile. Technical specifications and the results of the calibration are given in appendix D.1 and D.2 respectively. The geometry of the pressure meters in the pile is shown in figure 33.

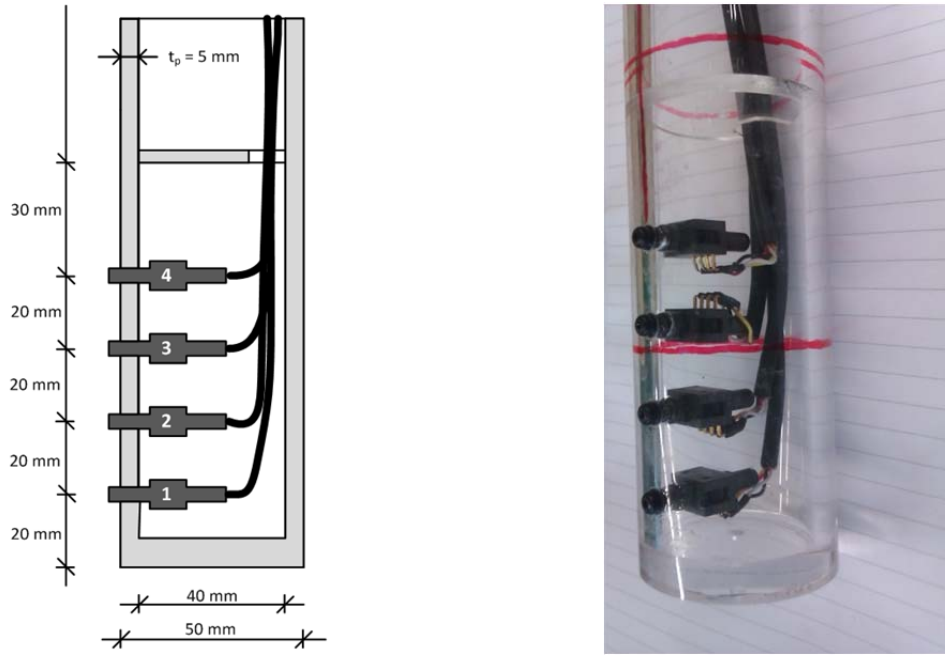


Figure 33: a) Geometry of the location of the piezometers and b) physical result of pile with piezometers

Besides the pore water pressure, the hydrostatic pressure at the bed can be derived from the water height. The applied pressure and actual pressure in the porous stone are measured manually once every test.

4.3.3 Velocity measurement

The flow velocity is measured in two ways, namely the flow velocity near the bed and depth averaged flow velocity.

The undisturbed velocity near the bed U_c is measured just above the bed. In accordance with e.g. Sumer et al. (2001) and Sumer et al. (2013) this is done at half the pile diameter above the bed, so for the pile used in this research this is at 25 mm above the bed level. The flow velocity here is measured 1.25 meter upstream from the pile. Disturbances from the approach slope on the bed pattern were visible just after the approach slope, but not around the pile, so the flow is assumed to flow undisturbed from edge effects there.

The near bed flow velocity is measured using an electromagnetic flow meter (EMS) of the type E30. The device measures the velocity components in two directions. Obviously, only the flow velocity in longitudinal direction is relevant. The output of the instrument is a voltage between -10 and +10 volt. For the setting of 1m/s every change of 1 V corresponds to 0.1 m/s. Because the measurement device shows some variation over time, the signal is averaged over 10 measurement points in time and it is stored every second. The accuracy is $\pm 1.5\%$ for the 1 m/s setting. Reference is made to appendix E and Delft Hydraulics (1990) for more information on this device. The EMS meters are sensitive to electromagnetic variations and temperature changes. Therefore the signal is calibrated every experiment run with stagnant water.

Furthermore the depth-averaged flow velocity is measured acoustically from the recirculation pipe. All the water is pumped through this pipe on which a Proline Prosonic Flow 91 discharge meter is installed. The signal from this device is between 2 volt in

absence of flow and 10 volt at maximum discharge (50 L/s). From the discharge of the pipe the depth average velocity can be easily determined by dividing with the water depth and flume width.

4.3.4 Water depth measurement

The water depth was measured manually during the experiment. After the flow in the flume was gradually switched on, it took approximately one minute to reach its intended magnitude. Switching it on directly would result in a wave going back and forth for some time. Then, based on a certain discharge, the water depth remained constant in time. Therefore, the water depth was measured once every test at five locations above the sand bed as defined in figure 34 and was averaged later. Among the various locations no significant difference could be found. This implies the height of the weir and the slope of the flume were chosen correctly. The slope of the flume was $55 \cdot 10^{-6}$. The state of the weir was not measured, because the flow was partially blocked by the recirculation pipe.

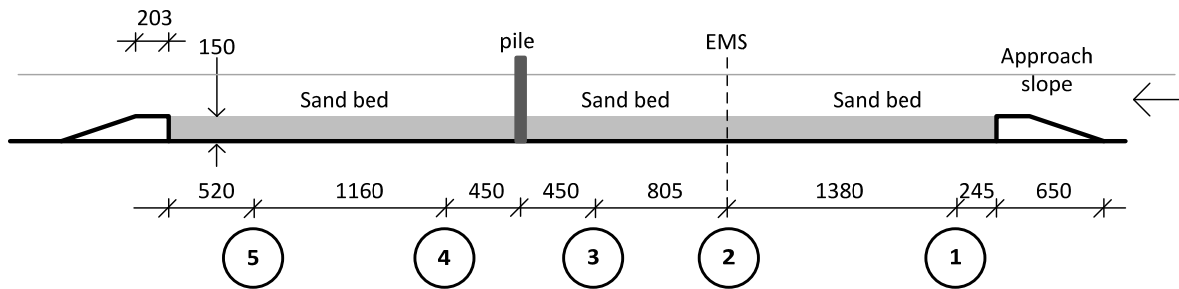


Figure 34: Five locations of the water height measurement (in mm)

4.3.5 Data acquisition

The data on pore water pressure, flow velocity and discharge was measured and stored automatically every second by DASYLab. Because the EMS signal is strongly fluctuating, the data is averaged over 10 measurements and stored every second. Details on the storage of the video images can be found in appendix C.3. Other data was measured manually.

4.4 Performed model tests

First one reference test is performed, where no excess pore water pressure (EPWP) is applied. Additionally five tests were performed with liquefied sediment. The reference test is used to see the effect of the EPWP and to compare with other studies. The conditions during all the test were aimed to be as shown in table 3.

Measurements show that among the various tests significant variation was present in the water depth, near bed flow velocity and depth-averaged flow velocity. Furthermore, the EPWP was varied among the different tests. Here the difference in water height of 52 cm was the minimum height that could be reached when the bucket was placed on top of the flume. Furthermore, 110 cm was considered to give a sound representation of the other extreme case. In table 4 an overview is shown of the different conditions per test.

Based on the sediment size the critical shields value was found to be $\theta_{cr} = 0.0405$. Note that the shields parameter based on the undisturbed bed friction velocity of test 1 is unintentionally below this value.

Table 3: Summary of design

Width of flume	b_{flume}	40 cm
Height of flume	h_{flume}	40 cm
Pile diameter	D	5 cm
Sediment height	h_{sed}	15 cm
Water height	h_w	21 cm
Grain size	d	260 μm
Average flow velocity in experiment	U	24 cm/s

Table 4: Overview of tests

Test no. [ID]	$\Delta h_{p,a}$ [cm]	$\Delta h_{p,od}(t=\infty)$ [cm]	h_w [cm]	U_c [cm/s]	\bar{U} [cm/s]	Re_p [-]	U_f [cm/s]	θ [-]	Fr [-]
1	0	0	20.3	1.9	26.0	9.6E+04	1.3	0.039	0.18
2	52	24	21.2	1.9	29.3	9.4E+04	1.4	0.049	0.20
3	55.8	19.5	21.5	1.9	28.8	9.5E+04	1.4	0.047	0.20
4	65.6	21	21.7	1.8	27.0	9.0E+04	1.3	0.041	0.18
5	71	24	19.0	2.0	30.8	9.8E+04	1.5	0.055	0.23
6	110	39	21.5	1.9	28.8	9.3E+04	1.4	0.048	0.20

The following steps are followed during the experiment:

1. Fill the flume with a small layer of water, so that the sand box is covered with water.
2. Remove the sand around the pile within the range of approximately 25 cm.
3. Fill the sediment box with sediment gently by hand, while rubbing the sediment between the fingers to ensure that it is free of air bubbles.
4. Equalise the bed.
5. Record a small data series with still standing water to calibrate the discharge and velocity signal.
6. Again switch on measuring devices, now including the camera in the pile.
7. Switch on the pressure in the porous stone and wait for approximately 5 minutes, so that the pore water pressure approaches equilibrium.
8. Switch on the current gradually.
9. Current is turned off when the equilibrium scour depth is reached. This is approximately after 2.5 hours.

In the reference experiment (test 1) step 7 is omitted.

5. Results

In this chapter the results of the experiments are given. Focus is put on the results of the scour depth in time and the pore pressure measurements. Besides these quantities other measurements were made like the water depth, depth-averaged flow velocity and undisturbed current velocity at the bed. These are considered as the circumstances of the experiment and are therefore given in section 4.4.

First the reference case is discussed. Subsequently, the tests with liquefaction are shown. Here a description is given of the process which took place during the experiments. This is supported by data of the scour depth evolution in time. Finally the results of the pore water pressure are shown.

5.1 Reference case

During the reference test the scour hole developed as expected according to the literature. First the scour depth increases rapidly, and as the scour hole grows, the scour rate decreases. This exponential behaviour agrees with literature (see section 2.4). Behind the scour hole a dune arose from sand that eroded from the scour hole. A photo of the scour hole is shown in figure 35.



Figure 35: Scour hole after reference test.

The time development of the scour depth is shown in figure 36. Here the scour depth is shown in dimensionless form as a function of a dimensionless time t^* , defined as

$$t^* = \frac{\sqrt{g(\rho_s - \rho)d^3 / \rho}}{D^2} t$$

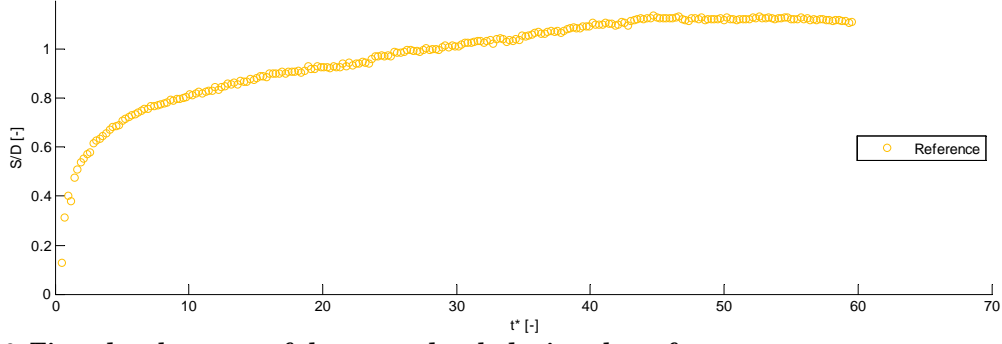


Figure 36: Time development of the scour depth during the reference case

The scour depth reached $S/D=1.13$ during the experiment. This is lower than the expected maximum scour depth under current $S/D=1.3$ that was presented by e.g. Sumer et al. (2002) and much smaller than $S/D=2.4$ as could be expected from the design method of Melville et al. (1999). Sumer et al. (2002) state that this value should be interpreted as an average value that can be obtained during their own tests and appeared to be the average value in literature. Also much larger values were found in other research. That the variability among the various studies had a “standard deviation” of $\sigma_{S/D}=0.7$. This is expected not to be caused by stochastic variability only, but can be caused by for instance scale effects, since Whitehouse et al. (2011) report that $S/D=1.3$ is already likely to overestimate the scour depth in the field due to the fact that various conditions occur. Raaijmakers et al. (2013) show variation of possible equilibrium scour depths over the North Sea, due to the variation of hydrodynamic conditions (see chapter 3).

When there is no scour at the start of an experiment, the scour depth in time $S_a(t)$ can be computed with

$$S_a(t) = S \left(1 - \exp\left(-\frac{t}{T}\right) \right)$$

The time scale T , or T^* in dimensionless form, can be estimated from literature and compared with the value derived from the above graph. Their definitions are given in section 2.4.3. T^* is estimated using Sumer et al. (1992) and Raaijmakers et al. (2008). Their values for the prevailing conditions are given in table 5. In figure 37 the development according these theories are added. Note that $S/D=1.13$ is taken as the equilibrium scour depth, so that both methods convert to the found equilibrium.

Table 5: Comparison with literature

	T_c^* [-]	T [min]	S/D [-]
Best fit reference experiment	7.66	1.13E+03	1.13
Sumer et al. (1992)	2.55	0.38E+03	1.3
Raaijmakers et al. (2008)	11.4	1.69E+03	1.5

Alternatively, the time scale can be estimated for the reference experiment with the best fit through the data, using the same exponential relation for the time development using

non-linear least squares as fitting method. This result is added in figure 36 (black line) and in table 5.

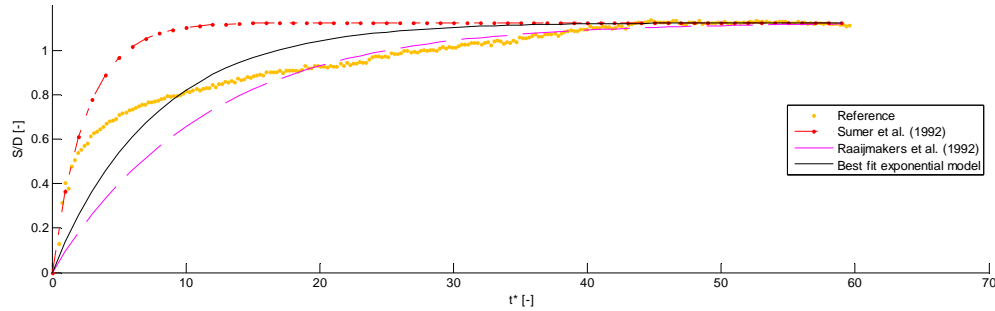


Figure 37: Time development of scour depth with prediction from Sumer et al. (1992) and with best fit

Finally it should be noticed that during all the experiments small waves were going back and forth. These waves were caused by slow horizontal movement of the recirculation pipe. The waves may have increased the scour rate during the experiment. Further discussion on this phenomenon can be found in section 6.1.

5.2 Results with liquefaction

5.2.1 Effects of liquefaction on the soil

Irrespective of the effect of liquefaction on scour, the effect of liquefaction caused by a monotonic excess pore water pressure (EPWP) has been investigated in preliminary tests. These tests were done with an aquarium instead of the flume. A more detailed description of the setup and outcomes is given in appendix F.

In these experiments, part of the soil is pressed upward after a certain time span and when the pore water pressure is large enough. The required waiting time depends on the applied pressure. This occurs in a shape similar to a saucer dome. The height gradually increases, implying the space of the pores becomes larger. Consequently the resistance to the upward flow decreases and the process is enhancing itself. Up to now the shape is relatively regular. This is schematised in figure 38a and 38b.

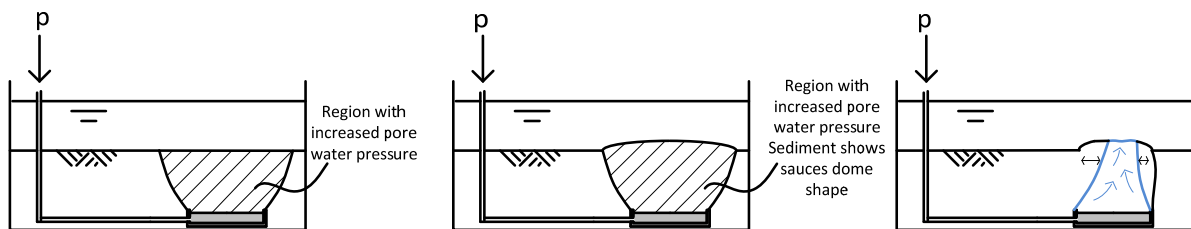


Figure 38: Schematisation of liquefaction process where: a) pore water pressure is increased, b) a saucer dome shape is arising, c) the blowout has taken place and the soil is liquefied.

After a certain moment the vertical resistance of the sand is lost and a current breaks through which transports sand as if it is in suspension. As soon this so-called blowout happened, the flow concentrates in one feeder, which may slowly move in horizontal direction and does not necessarily have a regular shape. Furthermore, it does not necessarily arise straight above the centre of the porous stone. The irregular shape could be explained by non-homogenous soil properties or an enclosed preference in the porous stone. The irregularity is more pronounced for smaller pressures. The height of the

liquefied region keeps being slightly higher than the surrounding. A photo is given in figure 39 and a schematisation is given in figure 38c.



Figure 39: Photo of liquefied region after blow out

After the upward flow is stopped, the sand keeps on being in a liquefied state for a while. This state may be assumed to follow the same behaviour as under wave-induced liquefaction from the moment that the liquefaction progressively dissipates, as was reported by Sumer et al. (2006). The negative pore water pressure gradient drives the water in the liquefied sediment upwards, whereas the sediment grains settle through the water until they come into contact with each other. This consolidation progresses as a line upwards through the sediment column (Sumer et al., 2006).

5.2.2 Liquefaction during the scour experiments

The same type of liquefaction behaviour could be expected during the scour experiments. To give the soil some time to adapt to the increased pore water pressure, the current was switched on approximately 300 seconds after the EPWP was added. The soil was not liquefied before the experiment started except for the test with $\Delta h_{p,a} = 110\text{cm}$. It was likely to occur during the experiment, since liquefaction takes some time to develop and at the location where the scour hole arose, the sediment column that provides the counteracting pressure to liquefaction decreased when the scour hole arises. Therefore, at a certain point a blowout was present in accordance to the situation without any flow. Since the scour hole had already some development, this blowout implied that the scour depth suddenly decreased significantly. Normally, the shape of the scour hole can be assumed constant throughout a scour experiment, even though the scour hole has not reached its equilibrium depth. This slope is the result of a balance between sliding sediment and erosion at the foot of the slope, see figure 15. Now, due to the loss of shear strength between particles, the sediment is no longer able to maintain this slope. Consequently, the scour hole partially collapses. Sediment from the surrounding is absorbed in the hole.

In the meantime, the soil around the pile has come into liquefaction and sediment is flowing along with the upwards flowing current. The liquefied sediment should be regarded as a fluid, now with different properties as relative soil density. The sediment

reacts immediately on the local pressure differences from vortices. Therefore it can principle be eroded more easily, since there is no shear strength left in the soil. This does not happen though, because the sediment should be transported away by the horseshoe and lee-wake vortices and this takes time. A new equilibrium arises, where a balance exists the erosion from vortices and added sediment from slope sliding. Just after liquefaction this balance may not be present, so the scour hole may still be able to grow, but the scour rate did not increase as a result of the liquefaction.

5.2.3 Effect on scour depth and time scale

These processes are confirmed by the data captured with the endoscope images. The measured scour depth in time for all experiments is given in figure 40. For every test 250 images from the endoscope data are represented by a point in this graph. The tests are also shown individually together with the reference tests scaled to their maximum. This is shown in figure 41 for the lowest excess pore water pressure (EPWP) till 45 for the highest EPWP. The EPWP is expressed as the head difference between the flume and the bucket connected to the porous stone and denoted as $\Delta h_{p,a}$. The individual tests are further elaborated here.

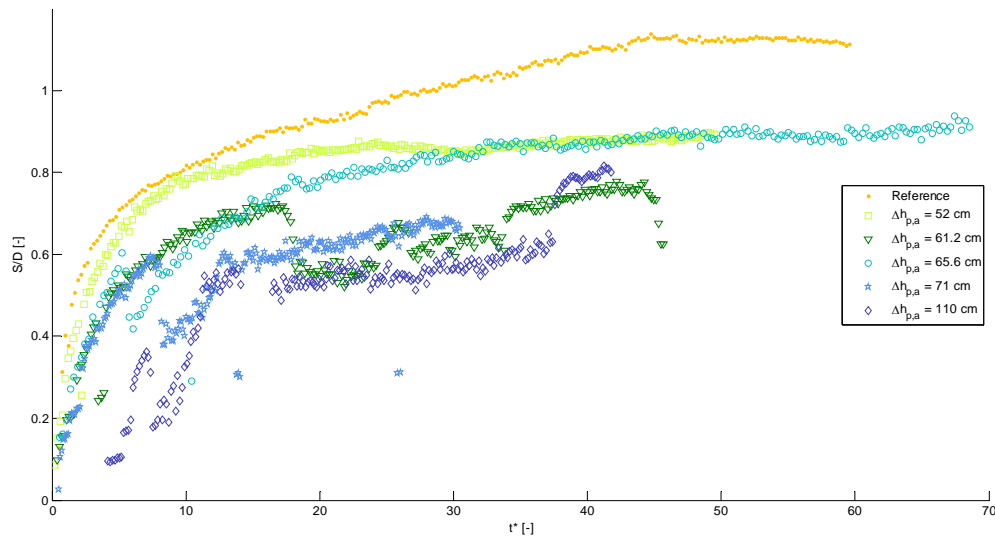


Figure 40: Scour depth in time with different values for the excess pore water pressure

The scour depth in time for the lowest EPWP is given in figure 41. The EPWP is $\Delta h_{p,a} = 52$ cm. This pressure was chosen as it is considered to be a pressure that was representative and still relevant for low pressure conditions.

Compared to the reference test, the scour depth develops quite similarly. Due to the EPWP no significant difference is shown in the initial development. It should be noted here that due to the low pressure the blowout happened quite late during the experiment and the sediment was not liquefied around the whole perimeter. Coincidentally the scour occurred neither at the location the scour depth is captured nor where the pore water pressure was measured, but at the other side of the pile. Therefore, a sudden decrease in the scour depth is not directly visible in the data. It can be seen though that from $t^* = 25$ the scour depth barely increased. So the liquefaction here did not significantly affect the rate of erosion, nor the time scale, but limits the equilibrium scour depth.

In figure 41 one measurement point shows at $t^* = 2$ a significantly lower value than the points surrounding it. This is an error which was caused by the processing of the images. Due to the black line which was visible due to a Plexiglas plate, the automatic capturing failed to recognise the correct light to dark transition. The same error can be seen in figure 41, 42 and 43. The Plexiglas plate is also the reason that in figure 42 and 44 the scour rate seems to slow down at approximately $t^* = 1$ and then makes a jump. This problem is further addressed in section 6.2.1.

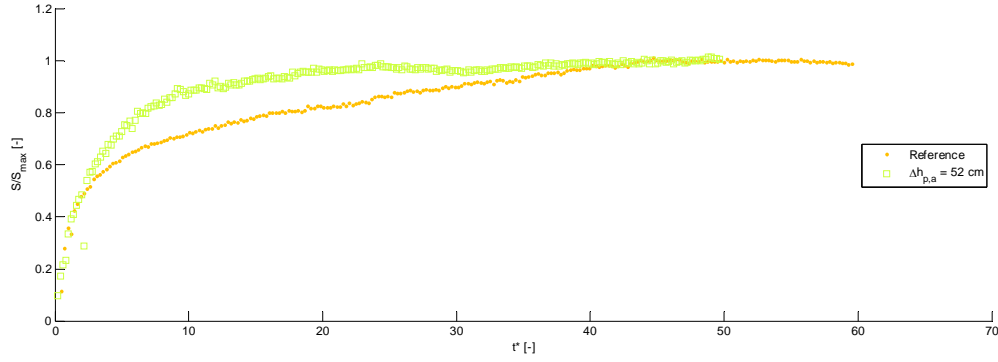


Figure 41: Scour depth in time for excess pore water pressure of $\Delta h_{p,a} = 52$ cm

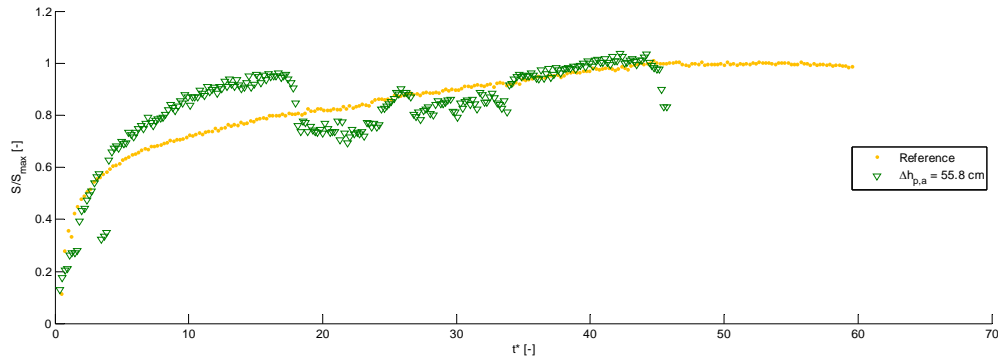


Figure 42: Scour depth in time for excess pore water pressure of $\Delta h_{p,a} = 55.8$ cm

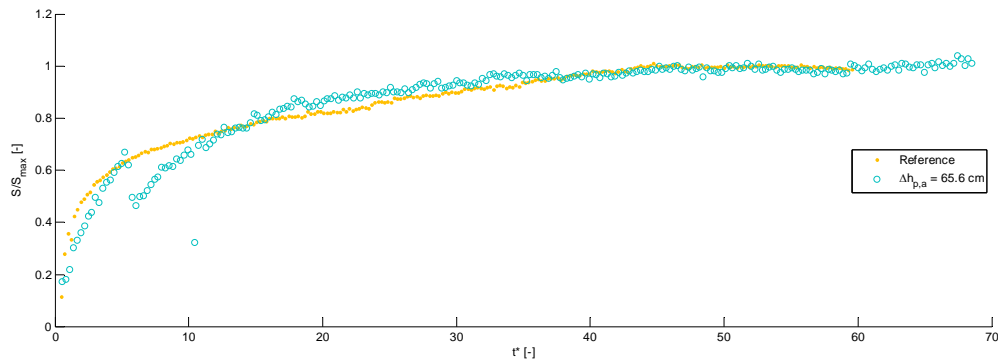


Figure 43: Scour depth in time for excess pore water pressure of $\Delta h_{p,a} = 65.6$ cm

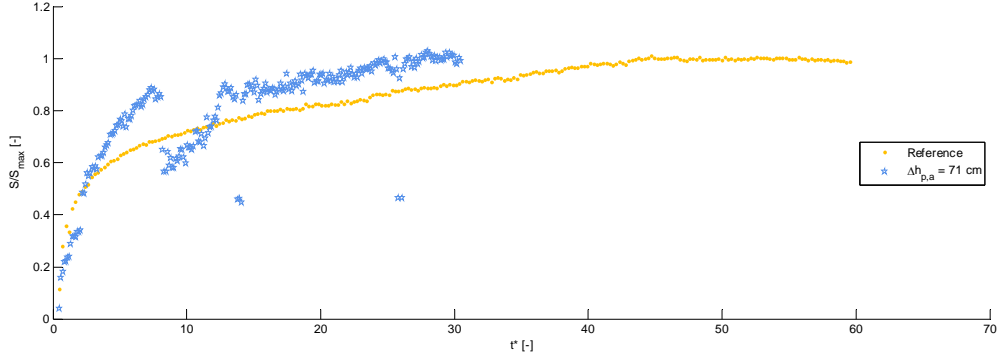


Figure 44: Scour depth in time for excess pore water pressure of $\Delta h_{p,a} = 71$ cm

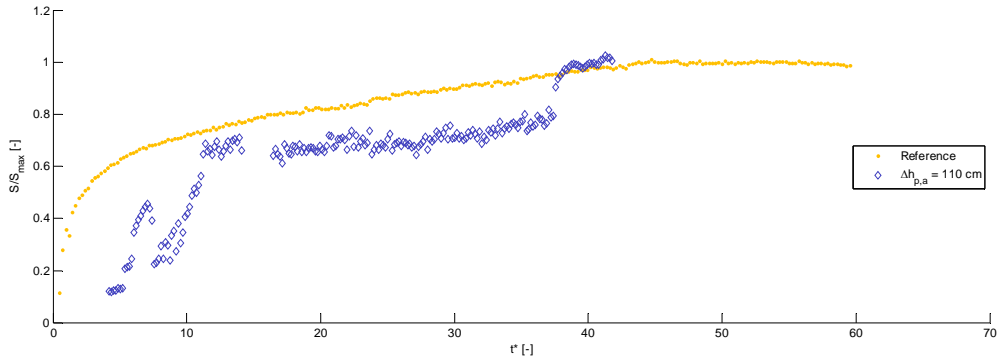


Figure 45: Scour depth in time for excess pore water pressure of $\Delta h_{p,a} = 110$ cm

Increasing the pressure to $\Delta h_{p,a} = 55.8$ cm, results in more or less the same pattern. The difference between the previous test is that the moment of blowout is better visible from the sudden decrease in scour depth. This sudden decrease is also visible from the images in figure 46 from just before and after the blowout.

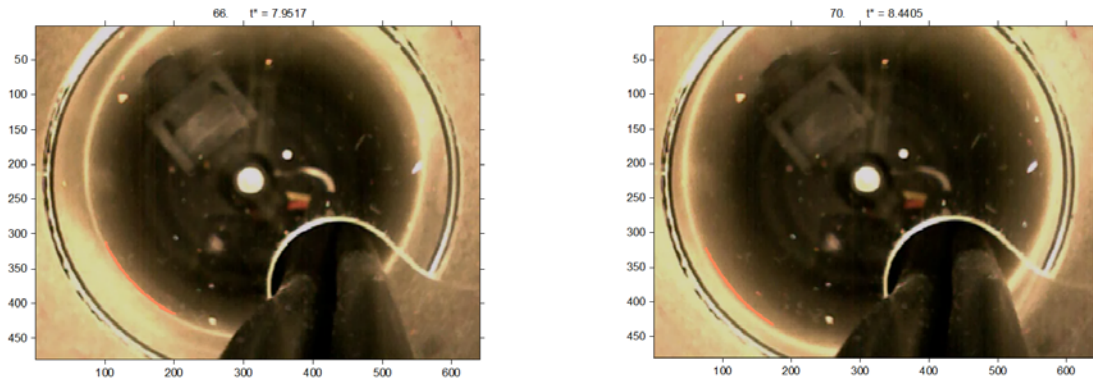


Figure 46: Image from endoscope a) before liquefaction of soil and b) after liquefaction of soil. The detected edge is shown by the red line, where only the upstream part of the perimeter is used to determine the scour depth.

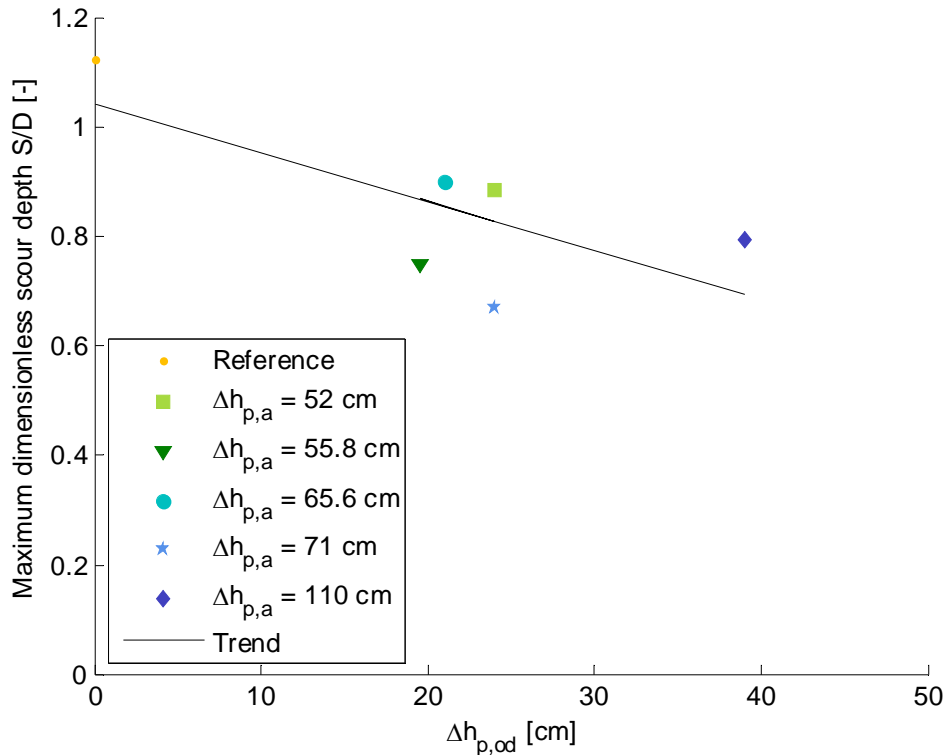
After this occurred, the scour depth is a bit more irregular in time. The scour hole continues to grow, even though the soil is in liquefaction. The final depth is lower than the under the test with the lowest pressure. This is with a lower angle so the scour width increases. This involves both $w_{upstream}$, $w_{downstream}$ and w_{side} .

Table 6: Maximum scour depth for every test

$\Delta h_{p,a}$ [cm]	$\Delta h_{p,od}$ [cm]	S [cm]	S/D [-]
0	0	5.65	1.13
52	24	4.43	0.89
61.2	19.5	3.75	0.75
65.6	21	4.50	0.90
71	24	3.35	0.67
110	39	4.88	0.98

The same pattern is visible for $\Delta h_{p,a} = 65.6$ cm, $\Delta h_{p,a} = 71$ cm and $\Delta h_{p,a} = 110$ cm. The last value is chosen as maximum since above this height, influence of the upward flow is enhanced even more without giving more information on scour. This is considered as an undesirable side effect and therefore falls beyond the scope of this research. Furthermore, the sediment is not expected to behave fundamentally different.

It can be concluded that for higher EPWP the sudden drop in scour depth occurs earlier with a higher EPWP. The test with $\Delta h_{p,a} = 110$ cm makes an exception here, because the soil was already in liquefaction when the current was put on. Therefore an increased bed level was present conform figure 38. Because this fell beyond the range of the camera, this is not present in figure 45 as negative scour depth. This is also the reason this graph seems to start from $t^* \approx 5$. Furthermore, this test shows a number of sudden changes, which could not be explained from the observations. The maximum scour depth of all experiments is given in table 6 and plotted in figure 47. The final scour depth is generally lower as the EPWP is higher.

**Figure 47: Relative scour depth as function of the excess pore water pressure**

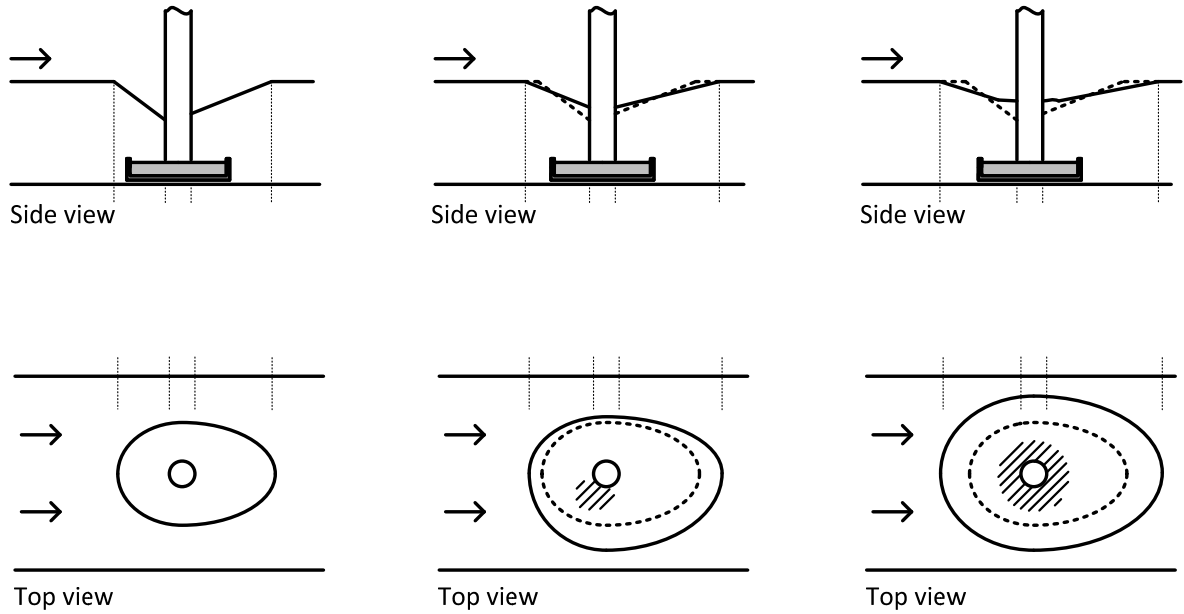


Figure 48: Characteristic changes in the shape of the scour hole due to liquefaction

Among the tests the area of liquefaction was different. This area is larger and more regular when the EPWP is higher. When the pressure is low the liquefied area is only at one side of the pile. This is shown schematically in figure 48. The dune that arose from eroded sand did not significantly change among the tests and extended over 20 cm downstream.

5.3 Results of the pore water pressure

The result of the pore water pressure in the piezometer 1 is shown in figure 49. This piezometer is the closest one to the porous stone. The time development of the pore water pressure at the other piezometers is given in figure A.13 till A.16 of appendix D.3.

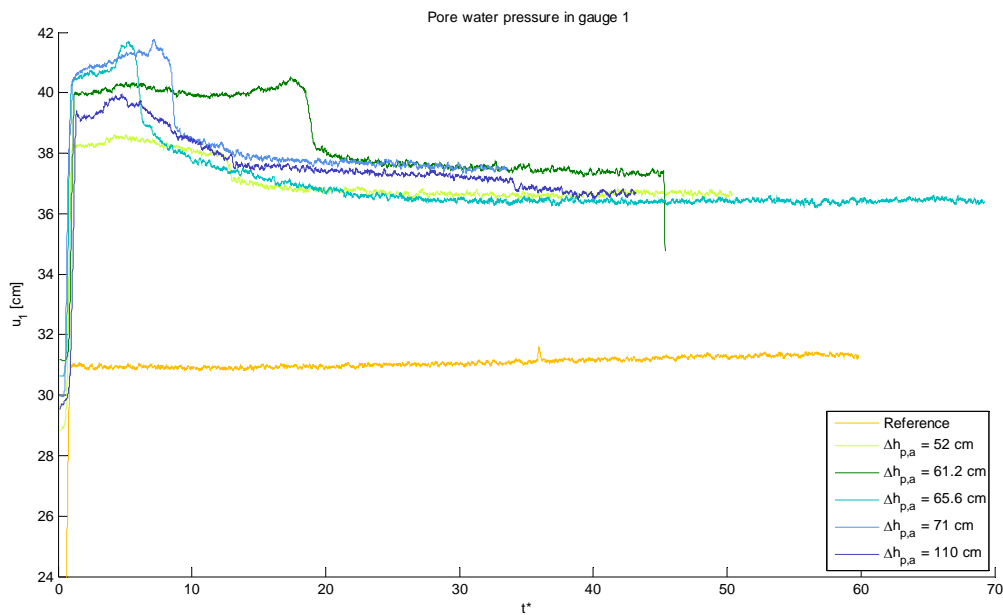


Figure 49: Time development of pore water pressure in piezometer 1 (bottom one)

Figure 49 shows that the pore water pressure is maximum just after the EPWP is applied. It barely takes time for the pore water pressure to adapt, since it increases almost immediately after EPWP is put on. This holds for all piezometers. So it can be concluded that it does not take much time for the soil to adapt to a pressure change.

Sudden drops are visible in the pore water pressure when liquefaction starts and the scour hole collapses. Then, the resistance of the soil is lost and is able to flow more easily. Consequently, the pressure decreases in the lower piezometers. Closer to the bed level, the pore water pressure should converge to the hydrostatic pressure, so there this effect is less noticeable.

Because the resistance from the soil is lost, the discharge of water provided from the porous stone increases. Due to the increased flow velocity in the tube between the bucket and porous stone, the resistance in this tube is increased.

For a certain moment of time the pore water pressure development over the vertical coordinate z can be drawn. Here the original bed level is defined as $z = 0$. This is done at $t^* = 2.7$, $t^* = 5.4$, $t^* = 7.42$, $t^* = 14.8$, $t^* = 27$ and $t^* = 33.1$, since these fall in between the pressure drops that are noticeable in figure 49. Other moments in time could be chosen too, but are not expected to give any new insight. Part of the result is given in figure 50, 51 and 52, while the complete set of graphs is given in appendix D.3.

At every moment of time the pore water pressure shows a linear relationship. Differences between the various tests are small. In the graphs the hydrostatic pressure distribution of the reference case is added, since this should coincide with the pressure distribution during the reference test. In the beginning this is indeed true, but as the time elapses, the pore water pressure at the top increases with respect to its theoretical value. It should be noticed here that the sand has been eroded around the piezometer measuring this pressure. It is likely this has affected the distribution somehow.

Furthermore, the pore water pressure of the other tests should be approximately the same at the upper piezometer at the end of the tests. It can be seen that this is indeed the case. The reference test is slightly lower which can be explained from the somewhat lower water depth.

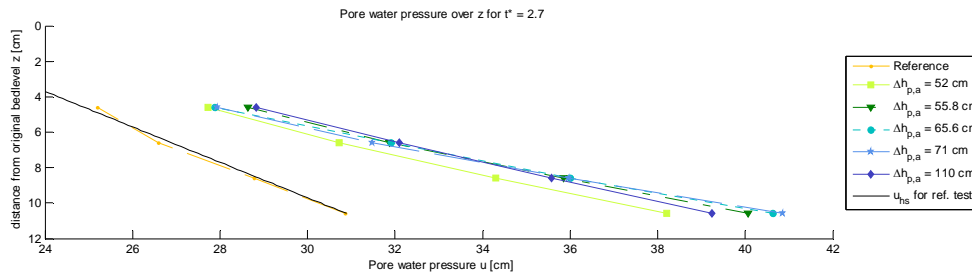


Figure 50: Pore water pressure distribution over depth at $t^* = 2.7$

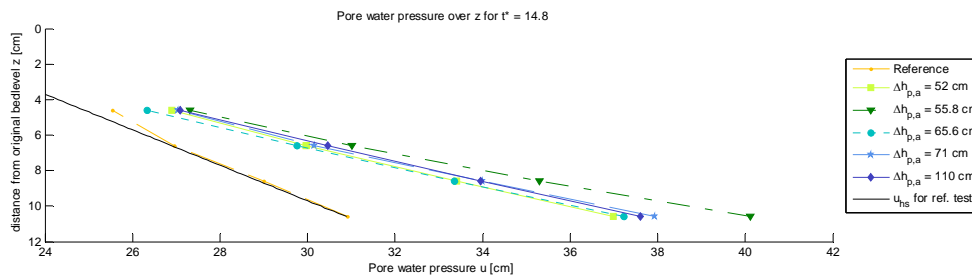


Figure 51: Pore water pressure distribution over depth at $t^* = 7.42$

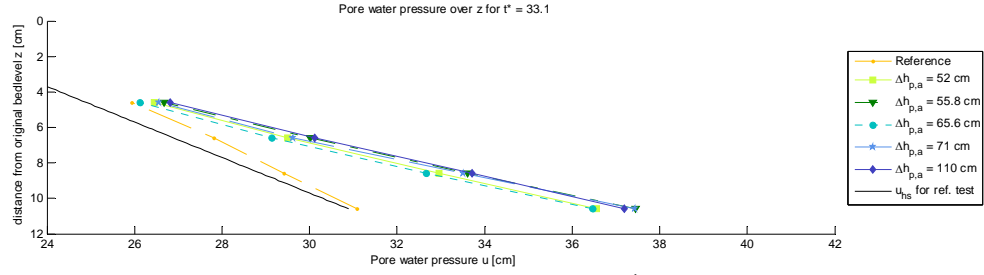


Figure 52: Pore water pressure distribution over depth at $t^* = 33.1$

From these graphs it is difficult to notice temporal differences in the pore pressure distribution. Therefore the pore water pressure is drawn for one test at the moments as defined before. The result is shown in appendix D.3. The graphs for the reference test, the lowest pressure and the highest pressure are given in figure 53, 54 and 55. Here the hydrostatic pressure, based on the water depth is added for the specific tests.

Figure 53 shows an increase in the pore pressure gradient, as was remarked earlier. From the other tests it can be concluded that the pore water pressure decreases in time, but the gradient remains more or less constant, since the lines remain parallel.

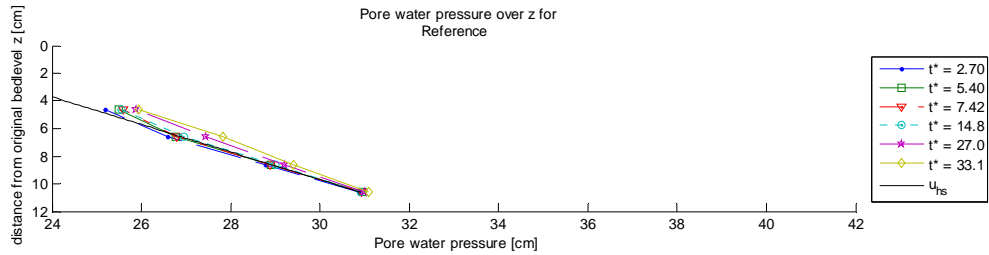


Figure 53: Pore water pressure distribution over depth during reference test

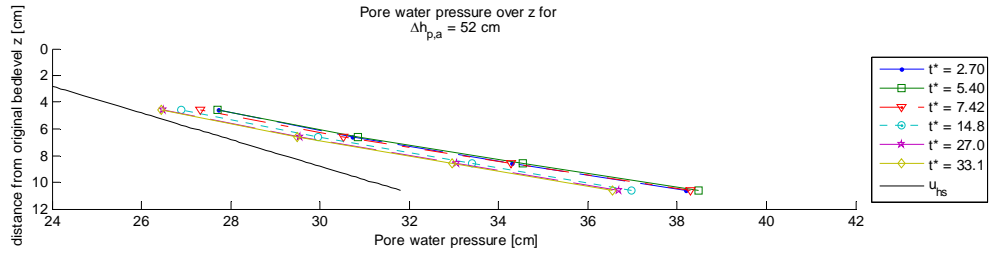


Figure 54: Pore water pressure distribution over depth during test with smallest EPWP

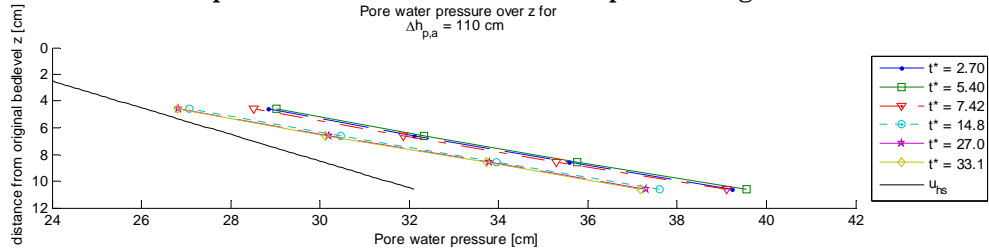


Figure 55: Pore water pressure distribution over depth during test with largest EPWP

6. Discussion

The scour experiments in this research have been performed in order to see the effect of liquefaction on scour. A number of remarks can be made on the results. For the observed behaviour this is done in section 6.1, whereas comments on the functioning of the setup are made in section 6.2. Besides this qualitative allocation of possible improvements, the most significant measurement errors are quantified in section 6.3. Next, in section 6.4 additional comments are made on the pore water pressure. Finally, the validity of the conclusions for field situations rather than laboratory conditions is discussed in section 6.5.

6.1 Behaviour of scour during experiments

The scour depth obtained during the reference test was somewhat lower than the values presented in literature, but large variance is reported in literature so no significant aberrance is found.

Furthermore, the time evolution of the scour depth had a different shape and could therefore not be fitted so well to the data from the reference test. From figure 36 it can be concluded that the agreement between the reference case and Sumer et al. (1992) is reasonable. Sumer et al. (1992) estimate the time scale from the time development by calculating the slope of the tangent line to $S_a(t)$ at $t=0$. Initially, the presented experiments show good agreement. However, after $t^* \approx 2$ the scour velocity decreases for the experiments. It takes significantly longer before the equilibrium scour depth has been reached. Furthermore, Raaijmakers et al. (2008) found the scour depth converging slower to the equilibrium scour depth, since their relation for the time scale results in higher values of T and consequently does not show full agreement. The actual performance depends on the capability of prediction at different scales and most importantly on prototype scale. It may be not feasible to determine the time scale very accurately, but it is important to get the right order of magnitude (Raaijmakers et al., 2008).

The best fit to the exponential model lies in between both Sumer et al. (1992a) and Raaijmakers et al. (2008), but still does not show a precise fit. It can be concluded here that the exponential relation for $S_a(t)$ appears to be not the best way to describe the current data. It is considered premature to draw strong conclusions based on one test, but the same problem has been observed by Harris et al. (2010) and Qi et al. (2012). More data is desired though to give strong conclusions on the scour development in time.

One of the possible reasons might be that a small grained fraction was present in the sediment, causing slight cohesive behaviour. This contingency is supported by the presence of a small fraction of sediment in suspension, making the water slightly turbid, while sediment with the median grain size was just in motion as bed load.

It might also be possible that the scour was not in a live-bed condition. Even though the ambient bed showed sediment movement and bed forms arose, the Shields parameter, calculated from the undisturbed bed friction velocity, is just below the critical shield value. $\theta / \theta_{cr} = 0.0388 / 0.0405 = 0.96$. Based on these values, the sediment motion should not have been present in the ambient bed conditions, while it was observed. Ripples arose over the whole bed. Furthermore, according to Melville et al. (2000) the time the

experiment would take to reach equilibrium is much larger for clear-water scour, i.e. in the order of a few days.

Accordingly it might have been possible that the flow condition were in a certain transition, where part of the sediment is in motion and part of it is not. Consequently, armouring may have had a relatively large influence in spite of the steep sediment gradation. Obviously, the experiment was not designed precisely at this transition but with live-bed conditions. The discharge during the experiments was slightly lower under the reference test compared to the others. Therefore, the tests with liquefaction did not face this problem.

During the tests small waves were observed going back and forth through the flume. This could have led to decreased equilibrium scour depth, as has been shown in experiments by e.g. Sumer et al. (2001). These waves were caused by vibrations of the recirculation pipe, which was partially blocking the outflow from the flume. The water height is normally arranged by a weir only, but in this case part of the area of outflow was blocked by the recirculation pipe. Therefore the motion of the recirculation pipe can lead to water motion in the flume. The magnitude of this effect depends on the discharge in the flume. Larger discharge in the flume led to more air in the recirculation pipe, which was enhancing this effect.

Furthermore, resonance was found around a certain discharge. Initially, additional tests were planned, where the flow velocity was aimed to be just below the critical flow velocity, so that clear water scour would appear. With this flow velocity resonance occurred and the amplitude of waves became so large that this was obviously the dominant eroding power. Due to the waves the ambient bed was in motion during part of the wave cycle. Alternatively, without modifications on the flume, a lower flow velocity could have been used to prevent the resonance, but this would have extended the duration of the test to a number of days. Consequently, no successful test on this flow velocity can be presented.

Finally, it should be noted here that among various experiments the soil density is very sensitive for the way the soil is put in the flume. Before every experiment the sand is taken out within a range of 25 cm around the pile. Next, the sand is again brought in while rubbing the grains between fingers and in the end the bed is equalised with a square trowel. The way this is done can make a large difference in the relative soil density. It is expected that this was fairly constant among the presented tests as this was done by the same person.

6.2 Functioning of setup

The functioning of the setup falls apart in a number of elements which have been used and are described in chapter 4. This includes the functioning of the endoscope camera to measure the scour depth, the constant pressure as driving force to cause liquefaction and the porous stone to apply the pressure. Apart from that, some critical notes are made with regard to the measurement of the quantities as were defined in chapter 4.

6.2.1 Endoscope camera

The endoscope camera is used successfully to derive a time curve of the scour depth. This data of the scour depth is obtained from the upstream side of the perimeter. From literature this was found to be the location with the largest scour depth. However, the

reason to use the endoscope camera was to measure the scour depth around the whole perimeter.

Furthermore, the endoscope camera only measures the depth around the perimeter. This is not necessarily a good indicator for the shape of the scour hole. Without liquefaction the angle of repose of the scour hole already differed among the different directions with respect to the flow velocity. However, at the start of the experiment these changes were not expected, so no measurements were made on this quantity. The shape of the scour hole appears to be a parameter that was changed due to the liquefaction. The shape of the scour hole is therefore recommended to be measured in the future. A bed profiling system can more easily provide the shape of the scour hole. Sumer et al. (1992) and Raaijmakers et al. (2008) argued that these measurement devices does not function well in a strongly mobile bed, where a substantial part of the sediment is transported in suspension. In the presented research, the ambient bed was just in motion so these problems for bed profile measurements are not expected to be significant.

The data from the images have been translated to a scour depth using a number of procedures from the Image Processing Toolbox from Matlab. This worked quite well for the presented tests, but a number of comments should be made on the quality of the data.

First of all, part of the perimeter is not covered by the images due to the presence of the pore water pressure gauges and wiring. This may be undesirable for further research when the scour depth data is desired around the whole perimeter. Symmetry with respect to the flow direction can be used to cover the whole perimeter.

Besides, it appeared to be important to properly fix the wires to the rest of the pile. An early design turned out to be insufficient because wires were broken off from the soldered connection as a result of the weight and the movement of the wires. Therefore, a new pile had to be made from scratch. In the new pile a small Plexiglas plate was glued to prevent the wires from horizontal movement. In addition they were connected to the pile at the top to prevent for both horizontal and vertical movement.

The Plexiglas plate, which was installed due to these practical considerations, turned out to cause persistent difficulties and errors in the translation from the scour depth records to the scour depth data. The edges were namely within the range the scour depth could reach. To increase the reliability of the endoscope records this must be prevented in the future.

The difficulties are illustrated in figure 56, where two images are given for the red circled errors as is shown in figure 57. The sharp dark to light edge is clearly visible in figure 56. In the image processing the ring from the Plexiglas plate is also selected. When the average distance to the centre of the pile in the image is calculated, these erroneous lines are taken into account. Consequently, around $S/D = 0.25$ the curve tends to hold up till it makes a jump and dropouts may be present later in the curve.

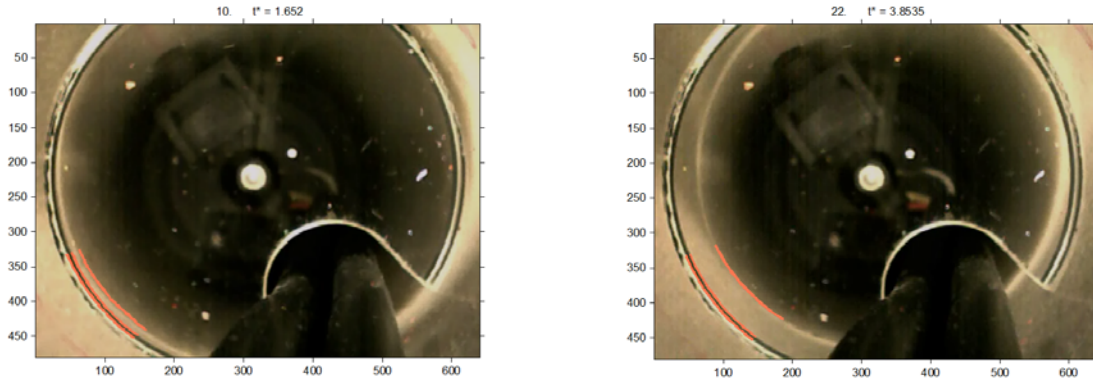


Figure 56: Error due to Plexiglas plate at a) $t^* = 1.65$ and b) $t^* = 3.85$

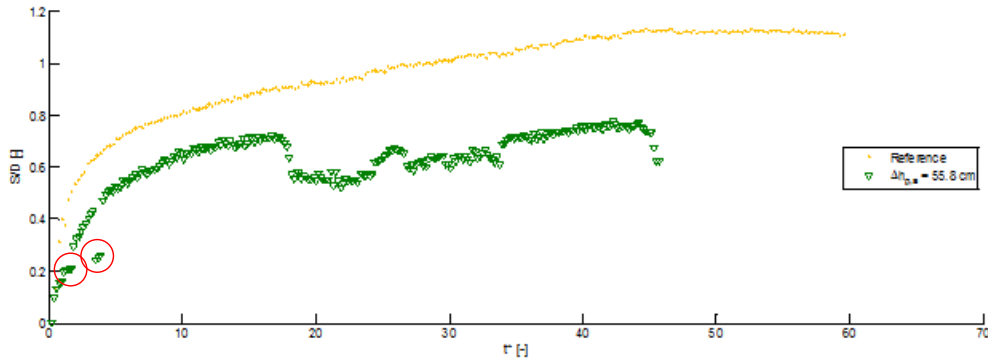


Figure 57: Problems due to the small Plexiglas plate in the pile

In order to minimise this type of errors, much effort is put to select the right grayscale threshold for every test. The selected grayscale threshold also had a strong effect on whether the dark-light edge is detected at the right place. If the selected grayscale threshold is too dark this results for example in the situation of figure 58a, while if the grayscale threshold is too light, this results in too many dropouts like in figure 58b. For further research it is strongly recommended to make sure the Plexiglas plate is placed higher in the pile and is out of the sight of the camera. Much effort can be saved and the quality of data can be improved.

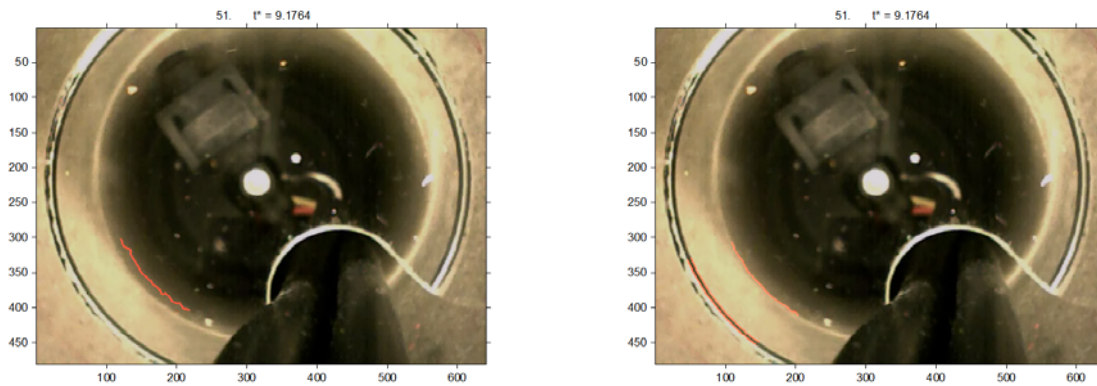


Figure 58: Detected edge when the selected grayscale threshold is a) too high and b) too low

The grayscale threshold was different among the various tests, because the amount of light was different among the tests. Moreover, this can be the reason of the problems with the dropouts. The corresponding images of the dropouts in for example figure 56 were brighter than the others. It is likely that during the tests clouds and sunshine were

alternating. Furthermore, maintenance on the lights was carried out in the same period as the tests were executed. This implied that the light may have been turned off for part of an experiment and a bridge crane was moving back and forth. This can also be the reason that a number of strange jumps were found in the test with $\Delta h_{p,a} = 110$ cm, see figure 45.

6.2.2 Constant pressure as liquefaction mechanism

Applying a monotonic excess pore water pressure (EPWP) caused some side effects which does not take place in the field. In case liquefaction is caused in the field, for example by waves, it is expected that the rest of the bed is also in a liquefied state. During the test the excess pore pressure creates a negative gradient in the pore water pressure. This makes that the water has to flow upwards. Because the water takes the path of minimum resistance, it concentrates in one feeder, see figure 38 in section 5.2.1. In this feeder the soil is behaving as a liquid, but in the surrounding it is not.

The fact that the liquefaction only locally takes place, can be prevented by applying the EPWP over a larger area i.e. over a much larger area than the sediment height. However, the soil is still transported upwards by the water and due to the weight of the sediment some is also transported downwards again. This flow pattern was found similar to a flow field under Rayleigh-Bénard convection and was also observed during preliminary tests when a high pressure was applied in the porous stone and a large area was liquefied. This is also considered to be an unrealistic side effect.

The soil was observed to behave more realistically as soon the pressure in the porous stone was turned off. Initially, the soil was still liquefied and consequently had reduced shear strength. This is only temporarily and after sufficient time has passed, the excess pore water pressure is dissipated while the soil is left compacted in a similar procedure as described by Sumer et al. (2006) (see section 2.5.1). Measurements on this behaviour were not made but are interesting for further research as it can indicate the influence of the soil density on scour.

A problem with the current setup is that due to a certain pressure, as soon as the soil starts to become liquefied, the process is enhanced due to the reduced resistance of the soil. Therefore, a stable state with the soil just liquefied is not possible to reach with a monotonic pressure. This might be improved though when the flow towards the porous stone is discharge regulated. As soon the soil starts to liquefy, the pressure decreases because the flow has to remain constant then.

6.2.3 Porous stone

The porous stone is used to introduce the EPWP evenly to the soil. This was done satisfactorily, though in the test with $\Delta h_{p,a} = 52$ cm the liquefied region was on one side of the pile only. The irregular shape could be explained by non-homogenous soil properties or an enclosed preference in the porous stone. The last is more likely, because the same preference was observed several times after the soil was taken away and brought in the flume again while rubbing soil grains. When there is an enclosed preference in the porous stone, the result is likely to be biased when the EPWP is decreased even further than $\Delta h_{p,a} = 52$ cm.

6.2.4 Resistance in tube and porous stone

As described in section 4.2.2 there is a large resistance in the tube between the porous stone and the bucket with constant water level. This resistance depends on the flow velocity in this tube, but it was found to be significantly high already during the preliminary tests (see appendix F). Therefore, besides the water level difference between the bucket and the water level in the flume, denoted as $\Delta h_{p,a}$, the pressure height just before the porous stone is measured with an additional tube. This height is denoted as $\Delta h_{p,od}$. The head in the porous stone was measured just after the current was switched on (so at $t \approx 0$) and when the scour hole was in equilibrium ($t \rightarrow \infty$). The results are given in figure 59.

This graph stresses that the resistance is indeed significant. A clear trend is visible between $\Delta h_{p,a}$ and $\Delta h_{p,od}$, but the applied pressure head is approximately two to three times higher than the pressure measured in the porous stone. Most of the resistance originated not from the tube itself, but from the connections that were used, since the inner diameter of these connections was lower than the tube.

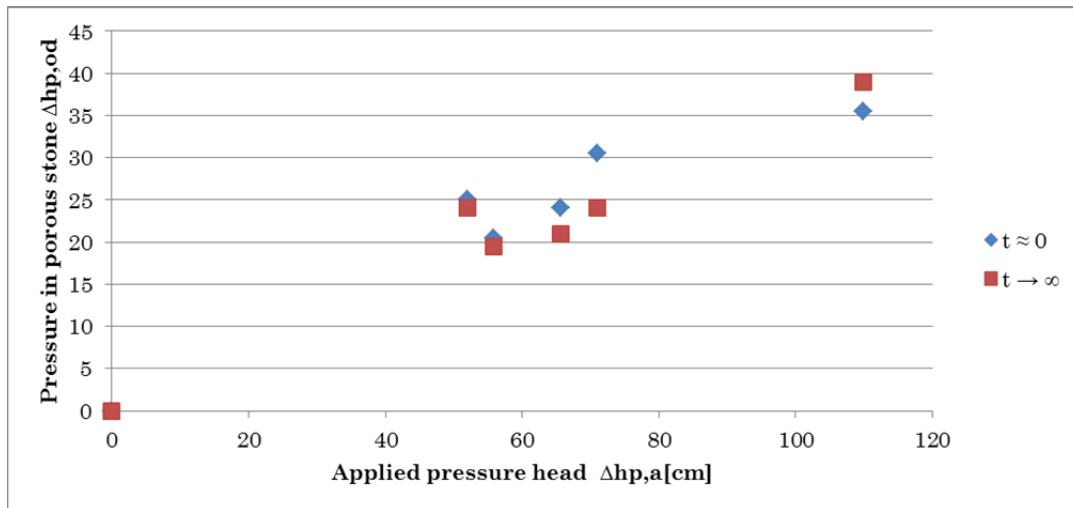


Figure 59: Difference between applied pressure difference and pore water pressure in porous stone

Next, the graph makes clear that the applied pressure is representative for the pressure in the porous stone, because it shows a linear relationship. It is considered more ideally though that the pressure in the porous stone is used as independent variable and that this pressure is kept constant in time, while the graph shows little variation. It was observed that the measurement at the start of the experiment strongly depended on how long the pressure was applied and how far the soil is in the liquefaction process. Figure 49 (section 5.3) shows that after the soil comes in liquefaction, a strong drop in the pressure is observed in the lower piezometers.

This can be improved by increasing the tube diameter and the diameter of the connections. Furthermore the length of the tube can be decreased a bit. Then the resistance from the tube is aimed to become insignificant with respect to the resistance of the soil, which imply that both $\Delta h_{p,a}$ and $\Delta h_{p,od}$ have approximately the same value.

6.2.5 Discharge measurement and bed velocity measurement

The discharge measurements and bed velocity measurements suffered from thread breakage. Therefore, during a number of tests part of the data series was erroneous, but during all the presented tests valid data points were present for part of the series and this data could be used without compromising the validity. After discovery this problem was repaired.

6.3 Measurement errors

6.3.1 Measurement of the scour depth

The largest uncertainty is expected around the detection of the sand water boundary in the endoscope images. The measurement errors are maximum when the scour depth is at its maximum, because in the endoscope images the same amount of pixels is divided here over a larger vertical distance of the pile, while this is actually the most relevant quantity. The measurement error for r is estimated to be $e_r = 12$ pixels in the worst case. The measurement error of the vertical coordinate of the bed level along the pile z is referred to as e_z and is defined as

$$e_{z,image} = z_{image}(r + e_r) - z_{image}(r).$$

This can be calculated for the value of r that corresponds to the maximum scour depth during the experiments $r = 173$ pixels. Consequently $e_{z,image}(r = 173) = 0.78$ cm

Besides, uncertainty exists in the measurement of the initial bed level. This is done manually. At the sides of the flume the intended initial bed level was marked with black tape on the flume walls. Despite the effort to equalise the bed carefully, small irregularities were present at the start of every experiment. In principle this does not influence the scour depth significantly, since this evens out after the flume is switched on, but if a sediment surplus or deficit is present over a larger part of the flume, this leads to an error in scour depth. This error is denoted as $e_{h, sed}$ and is estimated to be $e_{h, sed} = 0.3$ cm maximum.

The thickness of the porous stone and pile diameter could be measured rather precisely, so they are not expected to give significant measurement error compared to the other quantities. Following

$$\frac{S}{D} = \frac{h_{sed} - h_{od} - z}{D}$$

The maximum error in the dimensionless scour depth is expect to be

$$e_{S/D} = \frac{0.3 + 0.78}{5} = 0.216$$

Compared to the maximum dimensionless scour depth of $S/D = 1.13$ this is approximately 20%, so fairly significant. Conversely, it is not enough to invalidate the conclusions on the decreasing effect on the scour depth as a consequence of liquefaction.

6.3.2 Other measurement errors

Another significant measurement error is enclosed in the measurement of the water depth. The water height was measured manually at five locations. Due to the small waves from the recirculation pipe this was not just one value, but the water height was estimated from a moving water level. The waves had an amplitude of approximately 0.5 cm. Since the time averaged value is taken, part of the measurement error cancels out. The measurement error on the water height is estimated to be $e_{h,w} = 0.4$ cm.

The curve of the undisturbed current velocity at distance $D/2$ from the bed is shown in figure 60 and may indicate another measurement error. The manufacturer of the EMS devices promises a maximum measurement error of 1.5 %, which corresponds to 0.03 cm/s. Therefore, the variability is ascribed to the variability in flow velocity. Only the time-averaged value is used, so any variation is expected to cancel out.

Measurement errors should therefore be expected from calibration errors. At the start of every experiment an offset was detected, so the EMS device was calibrated every time before the experiment with 5 minutes record of still water. Nevertheless, it is possible this offset slowly rises during the experiment. This is illustrated with the time series of this data in figure 60, where the moving average is added as black line. It can be seen that at approximately $t = 2000$ s the flow velocity slightly decreases somehow. This can be due to errors in the measurement. Alternatively, this is caused by the influence of migrating ripples. This can be prevented by measuring a bit further from the bed.

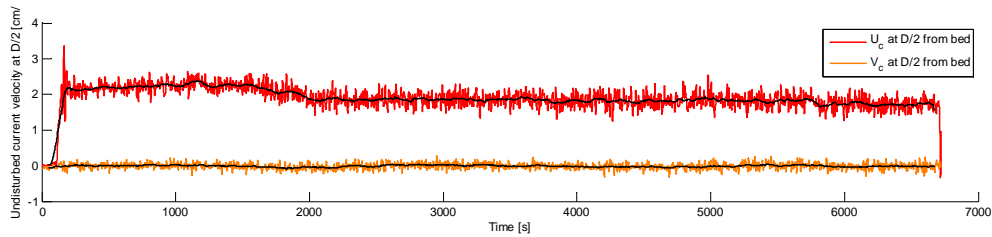


Figure 60: Undisturbed current velocity at distance $D/2$ from bed for $\Delta h_{p,a} = 55.8$ cm

Measurement errors on the discharge or depth-averaged flow velocity can be expected from the problems with the wiring as was addressed in section 6.2.5. Besides this, the device measures within the limit of 2% (Endress+Hauser, 2006). For the depth-averaged flow the error in the water height should be added.

Next, a measurement error of approximately 1 cm can be found in the measurement of the applied pressure in the porous stone, both for the applied pressure $\Delta h_{p,a}$ and actual pressure in the porous stone $\Delta h_{p,od}$. This is a measurement error of approximately 2% and 5% respectively. These quantities were difficult to measure since proper geometric references were lacking and the distance from the bucket or riser to the water could not be measured in a straight way. Furthermore the water level in the bucket may have fluctuated a bit during the tests.

6.3.3 Overview measurement errors

An overview of the estimated significant measurement errors is given in table 7.

Table 7: overview of significant measurement errors

Radial coordinate in images	r	6.9%
Sediment height	h_{sed}	2%
Water height	h_w	2%
Applied height difference bucket water level in flume	$\Delta h_{p,a}$	2%
Measured hydraulic head in porous stone	$\Delta h_{p,od}$	5%
Vertical coordinate from images	z_{image}	11%
Equilibrium scour depth	S	19%
Undisturbed current velocity at $D/2$ from the bed	U_c	1.5%
Depth-Average flow velocity	\bar{U}	4%

With these measurement errors figure 47 can be drawn again while giving the estimated bandwidth of the maximum error that could occur, see figure 61. This is done for both the dimensionless scour depth and for the pressure in the porous stone. The figure makes clear that the pressure in the porous stone does not significantly dispute any observation, while the bandwidth on the scour depth does. Only when $\Delta h_{p,a} = 71$ cm the error bar does not have any overlap with the reference test. It should be noted though that the conclusions are supported with visual observations during the tests.

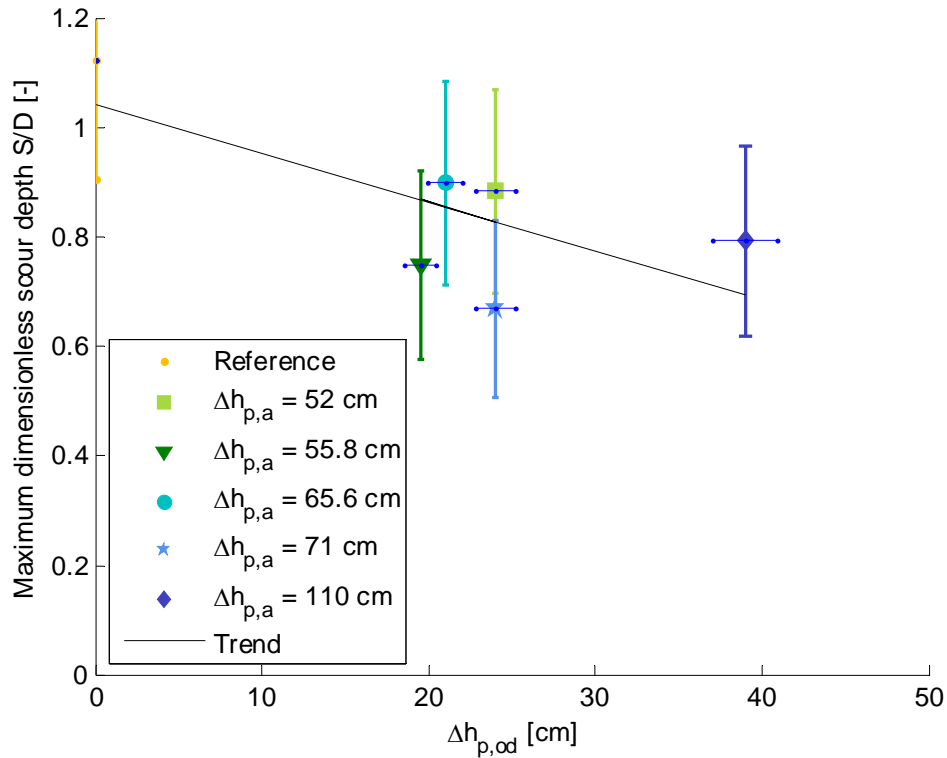


Figure 61: Accuracy of equilibrium scour depth

6.4 Pore pressure analysis

An analysis of the pore water pressure starts with the distribution of stresses as a consequence of the water column and the saturated soil. The effective vertical stress $\sigma'_v(z, t)$ follows from vertical stress $\sigma_v(z, t)$ and pore water pressure $u(z, t)$.

$$\sigma'_v(z,t) = \sigma_v(z,t) - u(z,t) = (\gamma_s - \gamma_w)z$$

Where γ_s and γ_w is the bulk unit weight of the soil and water. Assuming the soil to be in rest at $t=0$, the pressure distribution in the soil is drawn in figure 62. Now, as a consequence of the pressure added in the porous stone the pore water pressure was found to increase at a certain moment of time t . This is added in figure 62 in green. In the same time the scour depth is known to change the pressure distribution in the soil. This is shown in figure 63.

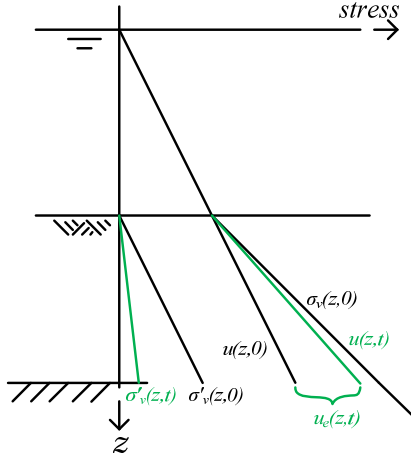


Figure 62: Pressure distribution of the soil, where the green line is the result of upward pressure

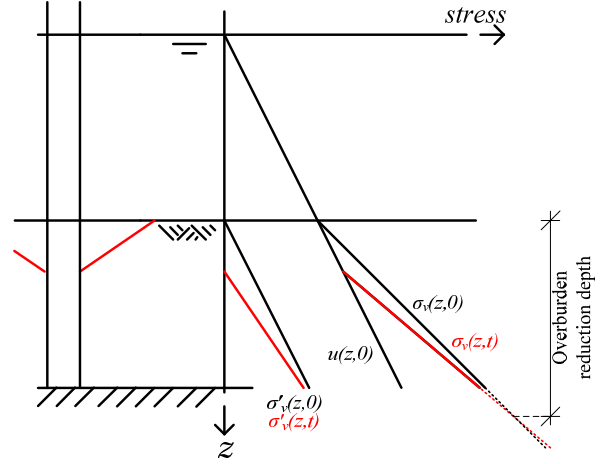


Figure 63: Pressure distribution of the soil, with in red the consequence from scour (after Zaaier and Tempel, 2004)

The difference between the initial and actual pressure is defined as the excess pore water pressure. In order to cause liquefaction the excess pore water pressure should be larger or equal larger to the initial vertical stress as long as the water height is constant, i.e.

$$\sigma'_v(z,0) \leq u_e(z,t) = u(z,t) - u(z,0)$$

The pressure development for the test with $\Delta h_{p,a} = 52$ cm together with the static water pressure are drawn again in figure 64 just after pressure was in balance at $t^* = 1.42$ and at the end of the experiment at $t^* = 33.1$. The measurements are extrapolated linearly to the bed level at $z = 0$ and to the top of the porous stone at $z = z_{od} = 12.6$ cm.

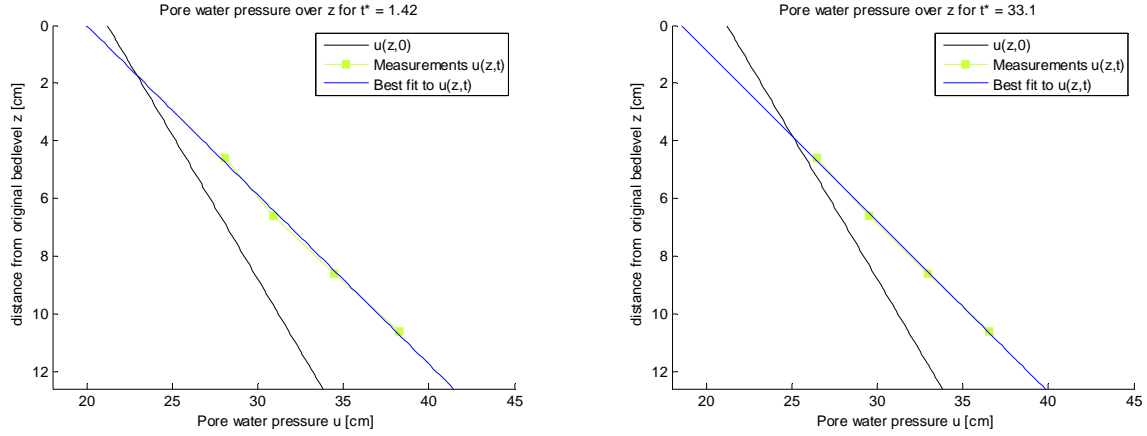


Figure 64: Pore water pressure development over sediment for a) $t^* = 1.42$ and b) $t^* = 33.1$

The extrapolated measurements should intersect with $u(z,0)$ at the bottom of the scour hole. Since at $t^* = 1.42$ the scour depth already developed till a certain extent, this intersection moved a bit downward, even more as the scour hole has developed. For $t^* = 33.1$ this intersection moved downwards. The intersection is at $z = 3.9$ cm. The final scour depth was $S = 4.4$ cm, so a small difference is observed. This is dedicated to the fact that the scour depth is not retrieved at the same location around the pile perimeter.

Furthermore, the interpolated pressure at the porous stone can be compared to the measured hydraulic head just before the porous stone. For the test with $\Delta h_{p,a} = 52$ cm was found:

$$u(z = 12.6, t^* = 33.1) = 39.8 \text{ cm}$$

The pressure in the porous stone is

$$u_{p,od} = h_w + \Delta h_{p,od} + z_{od} = 21.2 + 24 + 12.6 = 57.8 \text{ cm}$$

A significant difference is observed, so unless the pore water distribution close to the porous stone cannot be assumed to be linear, it can be concluded that significant resistance is present in the porous stone.

Based on the measured pressure it is difficult to predict the horizontal pressure distribution, because in the liquefied region the permeability strongly changed. A horizontal gradient should be present though, because further away from the pile the pore water pressure should converge to the pressure distribution $u(z,0)$. The magnitude of the horizontal flow depends on the change in permeability of the liquefied soil.

6.5 Implications of results for liquefaction in field

During the experiments the value of the Shields parameter was relatively low, namely $\theta / \theta_{cr} \approx 1.1$. So the bed was just in live condition. Practically this means for the scour that it takes longer to reach the equilibrium scour depth. The Froude number was somewhat higher during the experiments, but below one.

The behaviour in the field can be deduced from the presented results till a certain extent. For liquefaction in the field it is plausible that it has an equalising effect on the bed. Since liquefied soil reacts as a liquid with a relative soil density between water and non-liquefied soil it is likely to sink into the a scour hole when this is developing. This means that under the presented conditions the same behaviour is expected, despite that the fact that the extent is unknown.

Moreover, the impact to other types of turbine foundations are expected to be larger than for monopile foundations. These include the suction piles and gravity based structures as are shown in figure 65. Because the foundation depth is less deep while excess pore water pressure is able to build up under structural vibrations irrespective of the relative soil density. Therefore, the impact on the structural stability can be expected to be much larger.

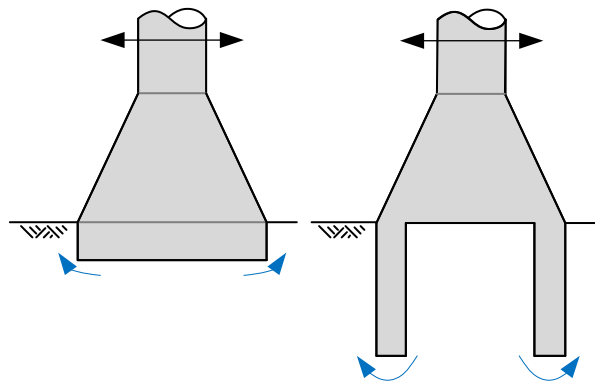


Figure 65: gravity based foundation and suction pile foundation

However, it is questionable whether the conditions during the tests are representative in the field. First of all, liquefaction was only present in part of the soil. This may be a realistic assumption when the liquefaction is caused by the vibrations of the monopile as a consequence of wind or waves, while it is unrealistic when it is caused by waves. Then the top layer of the bed is liquefied, but it can be expected to be present over a larger part of the seabed. If the liquefaction is present over the whole bed the equalising effect of the liquefaction may be much stronger. Maybe the scour hole does not even manage to arise as was reported in Sumer et al. (2007).

Secondly, considering liquefaction from structural vibrations, only little is known about the liquefying potential. The vibrations may not be large enough or the liquefied region may be small. From the literature information on this topic is scarce. For example Sumer et al. (2002), Sumer (2005) and Groot et al. (2006) indicate that liquefaction as a consequence of structural vibrations is possible, but are lacking case specific analysis or support with experimental data. More research is necessary to cover this topic.

In addition, it can also be relevant to investigate the influence of the relative soil density. Due to structural vibrations the soil can be compacted. Sumer et al. (2007) indicated that also the relative soil density affects the scour behaviour around a monopile. Denser silty soils tended to have a larger angle of repose and can lead to increased scour depths. It should be noted though that this was concluded from tests with dense and medium dense silt only. This effect can also be present for sandy soils.

Furthermore, looking from the scope of structural stability, it is unknown to what extent the structure is affected by the liquefaction. Scour is known to affect structural stability

in a negative way, so scour protection is often applied to avoid these effects. In the case of liquefaction, the scour depth may decrease somewhat as was shown in the presented research, but it is not very likely this is actually favourable for the structures stability. Since the soil around the structure has barely any shear strength left and is behaving as a liquid, it is more likely that a monopile foundation does not experience any resistance from this soil. Then, even if there is any scour, this is no longer so relevant, since the area and the depth at which liquefaction takes place is much more important. The only contribution of the sediment is the weight of sediment that still contributes to the stability of the soil at a larger depth. So, also here it is concluded that more research should be done on the potential of liquefaction and to the effects of the liquefied soil on the structural stability.

In the experiments only current-induced scour is investigated. The results can be extended to wave induced scour. The flow pattern due to waves depends on the wave frequency in proportion to the pile diameter, so whether vortices can fully develop under a wave cycle. The largest scour depth can be expected when the horseshoe vortices get enough time to develop with a similar flow pattern as under current only. When during a substantial part of the wave cycle the vortices are absent, the scour depth does not develop during part of the time and the scour hole will be less deep. The equalising effect is therefore expected to increase further, as the eroding force of the waves is less, while the sliding of sediment still continues. Consequently, the equilibrium scour depth decreases. Unless waves caused the liquefaction, scour is still expected to rise, since again a balance will be found between the erosion from the flow and down sliding of sediment along the slope of the scour hole.

7. Conclusions and recommendations

Current induced scour around an offshore wind turbine is simulated in a laboratory flume, where current-induced scour arose as a consequence of horseshoe vortices, lee-wake vortices and flow contraction. In the presented research the effects of vibrations in a monopile foundation leading to residual liquefaction have been simulated through its effects on the pore water pressure. To maintain the soil in liquefied state during the whole experiment, a constant excess pore water pressure is introduced at the bottom of the flume. Five tests were performed with a different excess pore water pressure in order to induce liquefaction, besides one reference test without added pressure.

In section 7.1 the conclusions are drawn in accordance with the research questions. The recommendations fall apart in recommendations for further research (section 7.2) and recommendations on improvements on the used experimental setup (section 7.3).

7.1 Conclusions

1. What are the observed effects of liquefaction on the scour depth and time scale of scour development?

- The equilibrium scour depth is lower when liquefaction is induced with a higher excess pore water pressure. A new equilibrium is established between sliding of sediment and the eroding action from the vortices. The angle of repose decreased consequently.
- After liquefaction it is still possible for the scour hole to grow until it reaches its new equilibrium.
- The time scale of scour hole development is not influenced significantly by liquefaction.
- The pore water pressure in the liquefied area has a linear development over the height. This did not change neither much in time nor with different excess pore pressures.

2. How is the functioning of the experimental setup?

Scaled laboratory experiments are commonly used for investigations on scour. For this research a number of elements were added to such an experiment, including e.g. the use of a monotonic pore water pressure to induce liquefaction and the use of an endoscope camera to measure the scour depth.

With the presented experimental setup it is possible to show the development of the scour depth in time. The endoscope camera measures the scour depth from within the pile. This was found to be an appropriate way to monitor the scour depth in time around the whole perimeter. In the presented research the largest source of measurement errors was found in the translation from the endoscope images to the scour depth data, but further improvements can be made as is shown in the recommendations on the research setup in section 7.3.

In the experiment the excess pore water pressure was applied with a porous stone below the pile. Liquefaction was present after an abrupt break through and the sediment remained liquefied over time. This was desirable but caused side effects.

The behaviour as was observed in the reference test was satisfactory in accordance with the behaviour reported in literature and the conclusions on the effects of liquefaction

could be drawn without loss of validity. There were a number of differences. The equilibrium scour depth obtained during the reference test was lower than most studies show in literature. Besides, the development of the scour hole in time is commonly found to behave according to the solution to a relaxation problem and the actual scour depth is converging exponentially to the equilibrium scour depth. Initially, the scour depth in the reference test followed this development, where the time scale was computed according to Sumer et al. (1992b). As the scour hole developed, the time development started to deviate from the expected behaviour. Hence the exponential relation was found to be not the best way to describe the acquired data.

3. To what extent can the result from the laboratory be considered to be representative for the effect of vibrations of offshore wind turbines in the field?

- The equalising effect of liquefaction on the scour hole is also expected to occur in the field, but the degree is unknown.
- The potential gain of reduced scour depth is limited, since the liquefied soil behaves as a liquid, it may not be expected to provide a strong contribution to the stability of the structure.
- Waves superimposed on a current normally decrease the equilibrium scour depth. It is expected that the equalising effect of liquefaction is further enhanced as the value of Kc decreases, since the scour hole has less time during a wave cycle for development.

7.2 Recommendations for further research

This research contributes to the knowledge on the effects of structural vibrations on the stability of an offshore monopile foundation. The approach to induce liquefaction with a monotonic excess pore water pressure was motivated by the fact that it excludes effects on the soil density due to vibrations. Structural vibrations can also influence the scour development through densification of the bed. Information on the effects of the soil density is still scarce, so more research on the influence of the relative soil density is recommended.

Next to this, it is unknown to what extent movements in a monopile foundation are a threat through liquefaction. Here the problem is two sided.

On the one hand, case specific validation of available design methods is lacking to determine when structural vibrations of a wind turbine can cause liquefaction and whether these vibrations are large enough to do so. This can be done locally by using a calculated acceleration of the structure and making use of the method of Seed et al. (1983). This method is developed for earthquakes and validation for structural vibrations is not known to the author. The acceleration can also be calculated further away from the pile and the method of Seed et al. (1983) can be applied there to determine locally when the soil liquefies. This method does not describe what further happens in time. Finite element calculations on the development of the pore water pressure in time and space take excessive non-linear computational efforts and are not possible yet.

On the other hand, it is uncertain how large the resistance of the soil is to horizontal movements when the soil is liquefied. So to what extent the liquefied soil still contributes to the stability of the structure. This can also be examined by first liquefying a soil and then test its horizontal resistance, both to slow and fast motion.

In addition, research can be performed on other types of foundations like gravity based foundations and suction pile foundations. Liquefaction may also occur here and because of the limited foundation depth, the impact of soil liquefaction may be significant.

7.3 Recommendations on experimental setup

A number of recommendations can be made with respect to the research setup.

- The shape of the scour hole was not measured, because it was not expected this would be influenced, while observations showed the angle of repose decreased as a consequence of liquefaction. For further experiments it is recommended to measure the scour width, both to describe the size of the scour hole and to see the impact of liquefaction on the angle of repose. Preferably this is measured continuously with a bed profiling system in combination with the more accurate data on the maximum scour depth. This data can also be used to derive whether the eroded volume changed due to the liquefaction.
- Because of the monotonic excess pore water pressure a strong instability was present in the liquefaction process. After the abrupt break through the scour hole partially filled again due to the decreased angle of repose. The liquefied area concentrated to one feeder, which may move horizontally in time. Here sediment was in strong motion. This is considered to be unrealistic. For further research it is recommended to examine the possibility of applying the liquefaction discharge regulated instead of pressure regulated.
- Significant resistance was present in the tube between the bucket with constant water level and the porous stone, especially due to the small inner diameter of the connections. This can be solved by increasing the inner diameter of the tube and connections and reduce the tube length as much as possible. Most ideally the resistance is negligible and the pressure in the porous stone is equal to the head difference of the bucket and flume.
- The time development was not found to behave according to the exponential relation of Sumer et al. (1992b), while this relation is generally accepted. It is recommended to present this time development in further research.
- During the reference test the value of the shields parameter was just below its critical value. Even though ripples arose over the whole bed, the scour could have been in the clear-water range. It is advised to use higher flow velocities to provide certainty that $\theta/\theta_{cr} > 1$ and live-bed conditions prevail during the whole experiment. This was not possible with the current flume as the discharge could not exceed 25 L/s. This implies that a larger flume should be used or the geometry should be scaled down. The last is restricted by the minimum pile diameter to be able to install the endoscope camera and wiring of the piezometers.
- To improve the accuracy of the scour depth data, it is recommended to increase the resolution of the camera. If the scour depth data is required at a predefined side of the pile, the accuracy can further be increased by using a mirror as was done by e.g. Raaijmakers et al.(2008) and Sumer et al. (2013).
- Elements of the setup were blocking the field of vision of the endoscope camera. This is acceptable if this in the vertical direction. By making use of symmetry scour depth can be computed around the whole perimeter. If disturbances extent in horizontal direction, like from the Plexiglas plate, this causes persistent difficulties in computing the scour depth from the endoscope images.
- Small waves caused by vibrations of the recirculation pipe were going back and forth and may have influenced the scour development. This should be prevented. In this light it is recommended to make continuous measurements of the water depth.

References

- Angus, N.M., & Moore, R.L. (1982). Scour repair methods in the Southern North Sea. *Proceedings of the 14th Annual Offshore Technology Conference*, Houston, Texas.
- Baker, C.J. (1980). The turbulent horseshoe vortex. *Journal of Wind Engineering and Industrial Aerodynamics*, 6, 9 – 23.
- Bergman, M., Duineveld, G., Daan, R., Mulder, M., & Selma, U. (2012). *Impact of OWEZ wind farm on the local macrobenthos community, Final report*. Retrieved 4 June 2013 from NoordzeeWind, website: <http://www.noordzeewind.nl/kennis/rapporten-data/>.
- Breton, S.P., & Moe, G. (2009). Status, plans and technologies for offshore wind turbines in Europe and North America. *Renewable Energy*, 34, 646 – 654.
- Breusers, H.N.C., Nicollet, G., & Shen, H.W. (1977). *Local scour around cylindrical piers*. *Journal of Hydraulic Research*, 15 (3), 211 – 252.
- Chern, S., & Chang, T. (1995). Simplified procedure for evaluating soil liquefaction characteristics. *Journal of Marine Science and Technology*, 3 (1), 35 – 42.
- Day, R.W. (2002). *Geotechnical earthquake engineering handbook*. McGraw-Hill, New York, USA.
- Delft Hydraulics (1990). *Electromagnetic Flow Meter, an instrument for current analysis, Users manual*. Delft Hydraulics, Delft.
- Diamantidis, D., & Arnesen, K. (1986). Scour effects in piled structures – a sensitivity analysis. *Ocean Engineering*, 13 (5), 497 – 502.
- DNV (2013). *Design of offshore wind turbine structures, Offshore Standard NSV-OS-J101*. Retrieved 18 January 2013 from Det Norske Veritas (DNV), website: <http://www.dnvkema.com/services/ces/wind-energy/standards-guidelines.aspx>.
- Dutch Ministry of Infrastructure and Environment (2013). *Ontwerp-rijksstructuurvisie windenergy op zee, partiële herziening van het Nationaal Waterplan Hollandse kust en Ten Noorden van de Waddeneilanden*. Teltar Media, Pijnacker.
- Eadie, R.W., & Herbich, J.B. (1986). Scour about a single, cylindrical pile due to combined random waves and a current. *Proceedings of the 20th Coastal Engineering Conference*. American Society of Civil Engineers, New York, 1858 – 1970.
- Endress+Hauser (2006). Proline prosonic flow 91, Ultrasonic flow measuring system, operating instructions. Retrieved on 14 December 2013 from website <http://www.nl.endress.com/#product/91W?tab=documents&filter=010.030>.
- Fischer, T., Vries, W. de, Schmidt, B. (2010). *Upwind design basis, wp4: offshore foundations and structures*. Retrieved 4 June 2013 from UpWind, website: http://www.upwind.eu/pdf/WP4_DesignBasis.pdf.

- Geremew, A.M. (2011). Pore-water pressure development due to wave-induced cyclic loading in deep porous formation. *International Journal of Geomechanics*, 13, 65 – 68.
- Gómez, M.Á. (2007). *Load verification of the Arklow Bank offshore wind farm*. Delft University of Technology, Delft.
- Groot, M.B. de, Bolton, M.D., Foray, P., Meijers, P., Palmer, A.C., Sandven, R., Sawicki, A., & Teh, T.C. (2006). Physics of liquefaction phenomena around marine structures. *Journal of waterway, port, coastal and ocean engineering*, 132, 227 – 243.
- Harris, J.M., Whitehouse, R.J.S., Benson, T. (2010). The time evolution of scour around offshore structures. *Maritime Engineering*, 163, 3 – 17.
- Hartvig, P.A., Thomsen, J.M., Frigaard, P., & Andersen, T.L. (2010). Experimental study of the development of scour and backfilling. *Coastal Engineering Journal*, 52 (2), 157 – 194.
- Henderson, A.R., Morgan, C., Smith, B., Sørensen, H.C., Barthelmie, R.J., & Boesmans, B. (2003). Offshore wind energy in Europe – A review of the state-of-the-art. *Wind Energy*, 6, 35 – 52.
- Hjorth, P. (1975). *Studies on the nature of local scour*. Bulletin Series A no. 46, Lund, Sweden.
- Hughes, S.A. (1993). *Physical models and laboratory techniques in coastal engineering*. Advanced Series on Ocean Engineering volume 7, World Scientific, New Jersey, USA.
- Høgendal, M., & Hald, T. (2005). Scour assessment and design for scour for monopile foundations for offshore wind turbines. *Proceedings Offshore Wind Conference*, Copenhagen, Denmark.
- Khawairakpam, P., Ray, S.S., Das, S., Das, R., Mazumdar, A. (2012). Scour hole characteristics around a vertical pier under clear-water scour conditions. *Journal of Engineering and Applied Sciences*, 7 (6), 649 – 654.
- Klinkvort, R.T., & Hededal, O. (2011). Centrifuge modelling of offshore monopile foundations. In Gourvenec, S., & White, D., *Frontiers in Offshore Geotechnics II* (pp. 581 - 586). Taylor & Francis Group, London.
- Knighton, D. (1988). *Fluvial forms and processes, a new perspective*. Hodder Education, London, UK.
- Louwersheimer, W.F. (2007). *Scour around an offshore wind turbine*. Delft University of Technology, Delft.
- Marcuson, W.F. (1978). Definition of terms related to liquefaction. *Journal of the Geotechnical Engineering Division*, 104 (9), 1197 – 2000.

- Melville, B.W. (1975). *Local scour at bridge sites*. University of Auckland, school of engineering, Auckland.
- Melville, B.W., & Chiew, Y. (1999). Time scale for local scour at bridge piers. *Journal of Hydraulic Engineering*, 125, 59 – 65.
- Melville, B.W., & Coleman, S.E. (2000). *Bridge scour*. Water Resources Publications LLC, Colorado, USA.
- Melville, B.W., & Sutherland, A.J. (1988). Design method for local scour at bridge piers. *Journal of Hydraulic Engineering*, 114, 1210 – 1226.
- Nielsen, A.W., & Hansen, E.A. (2007). Time-varying wave and current-induced scour around offshore wind turbines. *Proceedings of the 26th International Conference on Offshore and Arctic Engineering*, San Diego, California, USA.
- NoordzeeWind (2008). *Offshore windfarm Egmond aan Zee, general report*. Retrieved 24 May 2013 from NoordzeeWind, website: <http://www.noordzeewind.nl/kennis/rapporten-data/>.
- Offshore Wind Energy (2008). *Map of existing and planned wind farms in North-West Europe*. Retrieved 19 February 2013 from website <http://www.offshorewindenergy.org>.
- Petersen, T.U., Sumer, B.M., & Fredsøe, J. (2012). Time scale of scour around a pile in combined waves and current. *Proceedings of the 6th International Conference on Scour and Erosion*, Paris, France.
- Qi, W., Gao, F., Han, X., & Gong, Q. (2012). Local scour and pore-water pressure around a monopile foundation under combined waves and currents. *Proceedings of the 22nd International Offshore and Polar Engineering Conference*. International Society of Offshore and Polar Engineers (ISOPE), Rhodes, Greece.
- Raaijmakers, T., & Rudolph, D. (2008). Time-dependent scour development under combined current and wave conditions – Laboratory experiments with online monitoring technique. *Proceedings of 4th International Conference on Scour and Erosion*, Japan.
- Raaijmakers, T., Joon, T., Segeren, M.L.A., & Meijers, P. (2013). Scour: to protect or not to protect, that's the question! Feasibility of omitting scour protection. *Proceedings of the International Conference European Wind Energy Association 2013*, Frankfurt, Germany.
- Reese, L.C., & Wang, S.T., & Long, J.H. (1989). Scour from cyclic lateral loading of piles. *Proceedings of the 21st Annual Offshore Technology Conference*, Houston, Texas.
- Roulund, A., Sumer, B.M., Fredsøe, J., & Michelsen, J. (2005). Numerical and experimental investigation of flow and scour around a circular pile. *Journal of Fluid Mechanics*, 534, 351 – 401.

- Sakai, T., Hatanaka, K., & Mase, H. (1992). Wave-induced effective stress in seabed and its momentary liquefaction. *Journal of waterway, port, coastal and ocean engineering*, 118, 202 – 206.
- Seed, H.B., Idriss, I.M., & Arango, I. (1983). Evaluation of liquefaction potential using field performance data. *Journal of Geotechnical Engineering*, 109, 458 – 482.
- Sheppard, D.M., & Albada, E. (1998). Local scour under tidal flow conditions. *Proceedings of the International Water Resources Engineering Conference*, Memphis, Tennessee.
- Soulsby, R. (1997). *Dynamics of marine sands*. Thomas Telford Publications, Kent.
- Steedman, R.S. (1998). *Initial earthquake centrifuge model experiments for the study of liquefaction, final technical report*. European office of the US Army, London, England.
- Sun, X., Huang, D., & Wu, G. (2012). The current state of offshore wind energy technology development. *Energy*, 41, 298 – 312.
- Sumer, B.M., Fredsøe, J., & Christiansen, N. (1992a). Scour around vertical pile in waves. *Journal of Waterway, Port, Coastal and Ocean Engineering*, 118, 15 – 31.
- Sumer, B.M., Christiansen, N., & Fredsøe, J. (1992b). Time scale of scour around a vertical pile. *Proceedings of the 2nd International Offshore and Polar Engineering Conference*, San Francisco, United states.
- Sumer, B.M., & Fredsøe, J. (1997). *Hydrodynamics around cylindrical structures*. Advanced Series on Ocean Engineering volume 12. World Scientific, New Jersey, USA.
- Sumer, B.M., Fredsøe, J., Christensen, S., & Lind, M.T. (1999). Sinking/floating of pipelines and other objects in liquefied soil under waves. *Coastal Engineering*, 38, 53 – 90.
- Sumer, B.M., & Fredsøe, J. (2001). Scour around pile in combined waves and current. *Journal of Hydraulic Engineering*, 127, 403 – 411.
- Sumer, B.M., & Fredsøe, J. (2002). *The mechanics of scour in the marine environment*. Advanced Series on Ocean Engineering volume 17. World Scientific, New Jersey, USA.
- Sumer, B.M. (2005). Liquefaction around marine structures, Limas, an EU research program. In Cheng, L., & Yeow, K. (Eds.), *Hydrodynamics VI: theory and applications*. Leiden, The Netherlands, Balkema Publishers.
- Sumer, B.M., Hatipoglu, F., Fredsøe, J., & Sumer, K. (2006). The sequence of sediment behaviour during wave-induced liquefaction. *Sedimentology*, 53, 611 – 629.
- Sumer, B.M., Hatipoglu, F., & Fredsøe, J. (2007). Waves scour around a pile in sand, medium dense and dense silt. *Journal of Waterway, Port, Coastal and Ocean Engineering*, 133, 14 – 27.

- Sumer, B.M., Petersen, T.U., Locatelli, L., Fredsøe, J., Musumeci, R.E., & Foti, E. (2013). Backfilling of a scour hole around a pile in waves and current. *Journal of Waterway, Port, Coastal and Ocean Engineering*, 139, 9 – 23.
- Van der Walle, B. (2011). Offshore windmolens en het belang van een degelijke fundering. *De Grote Rede*, 29, 19 – 24. Oostende, Vlaams Instituut voor de Zee (VLIZ).
- Whitehouse, R.J.S. (1998). *Scour at marine structures*. Kent, Thomas Telford Publications.
- Whitehouse, R.J.S., Dunn, S.I., Alderson, J.S., & Vun, P.L. (2004). Testing of the interaction of coastal windfarm foundations with the seabed: scour and liquefaction. *Proceedings of the 29th International Conference on Coastal Engineering*, Lisbon, Portugal.
- Whitehouse, R.J.S., Harris, J.S., Sutherland, J., & Rees, J. (2011). The nature of scour development and scour protection at offshore wind farm foundations. *Marine Pollution Bulletin*, 62, 73 – 88.
- Zaaijer, M. B., & Tempel, J. van der (2004). Scour protection: a necessity or a waste of money? *Proceedings of the 43rd IEA Topical expert meeting*, Stockholm, Totalförsvarets forskningsinstitut FOI.
- Zen, K., & Yamazaki, H. (1993). Wave-induced liquefaction in a permeable seabed. *Report of the Port and Harbour Research Institute*, 31 (5), 155 – 192.

Influence of liquefaction on scour around offshore monopile foundations

Msc Thesis

March 2014

Appendices

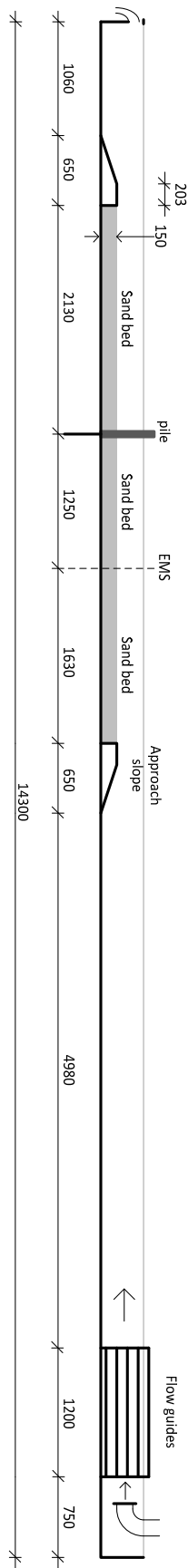


Ferdinand van den Brink

UNIVERSITEIT TWENTE.



Appendix A: Side view flume



Appendix B: Design considerations for the experiment

In this appendix the design of the pile dimensions and flow conditions is elaborated. First, the design constraints are given combined with the practical recommendations found in literature. These are used as point of departure for the design of the experiment. Most important quantities to design for are the pile diameter D , median grain size diameter d , the water height h_w and the depth averaged flow velocity \bar{U} . These are determined here and the result is summarised in the end of this appendix.

Points of departure for the design of the experiment

A number of assumptions have been made for the experiment. The flume, which is available for the tests, has a width of $b_{flume} = 40$ cm, an height of $h_{flume} = 40$ cm and a length of 14.30 meter. A constant current will be used to induce scour around a pile because of practical reasons. Other important assumptions for the design are:

- A constant current is used to cause scour around the vertical pile.
- The conditions are such that the ambient bed is in motion. This implies that $\theta > \theta_{cr}$.
- Sand with normal density is used as bed material and water is used as fluid.
- The water level in the flume should be approximately 4 cm below the top edge as margin.
- 8 cm is required to provide space for the mechanism to liquefy the soil and to be able to measure the pore water pressure.
- The slope of the scour hole α is assumed to be 1:2.5. This is based on the shape as reported by Hartvig et al. (2010).
- The maximum depth of the scour hole is 1.3D based on e.g. Sumer et al., (2002) and DNV (2013).

For the design of the experiment a number of restrictions are mentioned in Whitehouse et al. (1998):

- The area of the model in the cross-section should not be larger $\frac{1}{6}$ of the total area of cross-section. Since the pile is present over the whole water height this leads to the restriction $D < \frac{1}{6} b_{flume}$.
- In order to prevent water depth effects, the water depth should be large enough, which is $h_w \geq 4D$.
- The median grain size of sediment should be larger than 100 μm in order to be non-cohesive.
- The sediment should not be widely graded.

Other restrictions are:

- The width of the scour hole w_{side} should be smaller than the width of the flume. Therefore $w_{side} \leq b_{flume}$.
- The time span of the experiments should be limited to a few hours.
- Liquefaction should last long enough so that the soil is in liquefaction during the whole experiment.
- The Reynolds number should be in the turbulent range, so above 4000 so that viscous forces have become independent of the Reynolds number.
- The pump in the experiment should have enough capacity to provide the required flow rate during the experiment. Consequently $Q \leq Q_{max, flume}$.

Design quantities of setup

Mean grain size

The mean grain size is chosen to be $d = 260 \text{ } \mu\text{m}$. This is larger than the minimal $100 \text{ } \mu\text{m}$ and is chosen for practical reasons, since it is in the order of magnitude of other experiments on liquefaction used and was already available in the laboratory.

Water height

The most demanding geometric restriction in the design appears to be $h_w \geq 4D$ and $b_s \leq b_{flume}$. Both the water depth and the width of the scour hole are influenced by the water depth.

The water depth that is still available in the flume, taking into account the margin from the topside (4 cm) and the minimal height of sediment below the scour hole (8cm), depends on the pile diameter D .

$$S_{\max} = 1.3D$$

$$b_s = 2 \cdot 2.5S_{\max} + D$$

$$h_w = h_{flume} - 4 - 8 - S_{\max}$$

Flow velocity

The flow velocity is determined from the requirement that the shields parameter is above the critical shields parameter. The requirement that $Re > 3 \cdot 10^4$ is easily fulfilled.

The critical value for the shields parameter follows from an algebraic expression from Soulsby (1997), representing the Shields curve.

$$\theta_{cr} = \frac{0.30}{1 + 1.2D_*} + 0.055[1 - \exp(-0.02D_*)]$$

Where

$$D_* = d \left(\frac{g \left(\frac{\rho_s}{\rho} - 1 \right)}{v^2} \right)^{1/3}$$

The actual value for the shields parameter is

$$\theta = \frac{U_f^2}{g \left(\frac{\rho_s}{\rho} - 1 \right) d}$$

Where U_f is the undisturbed bed friction velocity, calculated through

$$U_f = \frac{\bar{U}}{2.5 \left[\ln \left(\frac{30h}{k_s} \right) - 1 \right]}$$

k_s is the Nikuradse roughness. The flow velocity at its critical value U_{cr} corresponds with $\theta = \theta_{cr}$. Furthermore the Froude number and Reynolds number are calculated through

$$Fr = \frac{\bar{U}}{\sqrt{gh_w}}$$

$$Re = \frac{\bar{V}D}{\nu}$$

These quantities are given in table A.1 for a number of pile diameters. It can be seen here that the pile diameter cannot be larger than 5.0 cm.

The experiments should not last too long, so the parameters should be chosen accordingly. The time scale of scour is described in section 2.4.3. For live-bed conditions and current induced scour the dimensionless time scale is estimated to be (Sumer et al., 1992b):

$$T_c^* = \frac{1}{2000} \frac{\delta}{D} \theta^{-2.2}$$

And is made dimensionless through

$$T_c^* = \frac{\sqrt{g(\rho_s / \rho - 1)d^3}}{D^2} T_c$$

When a scour experiment is assumed to stop at 99% of the equilibrium since it follows an exponential function, the elapsed time can be derived from

$$\frac{S_a}{S} = \left(1 - \exp\left(-\frac{t_{95\%}}{T}\right) \right) = 0.99$$

This can be rewritten to be

$$t_{95\%} = -T_c \ln(0.01)$$

For clear water scour different relations have to be used. The time it takes to attain the equilibrium scour depth is (Melville et al., 2000):

$$t_e (days) = \begin{cases} 48.26 \frac{D}{\bar{U}} \left(\frac{\bar{U}}{\bar{U}_{cr}} - 0.4 \right) & \text{for } \frac{h_w}{D} > 6, \frac{\bar{U}}{\bar{U}_{cr}} > 0.4 \\ 48.26 \frac{D}{\bar{U}} \left(\frac{\bar{U}}{\bar{U}_{cr}} - 0.4 \right) \left(\frac{h_w}{D} \right)^{0.25} & \text{for } \frac{h_w}{D} \leq 6, \frac{\bar{U}}{\bar{U}_{cr}} > 0.4 \end{cases}$$

Also the result on the total time is shown in table A.1, although no strict requirements are raised. Based on this calculation the design is chosen and summarised in table A.2.

Table A. 1: Calculation on design quantities.

constants								
density of water	ρ	kg/m ³	1000					
density of sediment	ρ_s	kg/m ³	2650					
acceleration due to gravity	g	m/s ²	9,81					
kinematic viscosity	ν	m ² /s	1,0E-06					
Assumptions								
Angle in scour hole	α	-	1:2,5					
Minimal height of sediment below scourhole		m	0,08					
Margin from topside		m	0,04					
Input								
Grain size	d	m	260E-06	5.5 cm	5 cm	4.5 cm	4 cm	5cm
Pile diameter	D	m	0,06	0,055	0,05	0,045	0,04	0,05
width of flume	b_{flume}	m	0,4	0,4	0,4	0,4	0,4	0,4
maximum discharge	Q_{max}	L/s	30	30	30	30	30	30
Output								
maximal scour depth	S	m	0,078	0,0715	0,065	0,0585	0,052	0,065
sediment height	h_{sed}	m	0,158	0,1515	0,145	0,1385	0,132	0,145
water height	h_w	m	0,202	0,2085	0,215	0,2215	0,228	0,215
width scour hole	b_s	m	0,45	0,4125	0,375	0,3375	0,3	0,375
Dimensionless grain size	D^*	-	6,58	6,58	6,58	6,58	6,58	6,58
critical shields	θ_{cr}	-	0,041	0,041	0,041	0,041	0,041	0,041
critical velocity	U_{cr}	m/s	0,266	0,267	0,268	0,269	0,270	0,268
Choice flow velocity								
Depth-averaged flow velocity	\bar{U}	m/s	0,28	0,28	0,28	0,28	0,28	0,24
Further output								
Froude number	Fr	-	0,20	0,20	0,19	0,19	0,19	0,17
Nikuradse roughness	k_s	m	650E-06	650E-06	650E-06	650E-06	650E-06	650E-06
Undisturbed bed friction velocity	U_f	m/s	0,0138	0,0137	0,0137	0,0136	0,0136	0,0117
Reynolds number	Re	-	16800	15400	14000	12600	11200	12000
shields at bed	θ	-	0,045	0,045	0,044	0,044	0,044	0,033
Discharge	Q	m ³ /s	0,0226	0,0234	0,0241	0,0248	0,0255	0,0206
Discharge	Q	L/s	22,6240	23,3520	24,0800	24,8080	25,5360	20,6400
Dimensionless time scale (live-bed)	T_c^*	-	1,5470	1,7720	2,0434	2,3767	2,7950	-
Time scale (live-bed)	T_c	s	330	318	303	285	265	-
Time for 95% of scour hole evolvement (live-bed)	$t_{95\%}$	min	25,3	24,4	23,2	21,9	20,3	-
Time to reach equilibrium (clear-water)	t_e	days	-	-	-	-	-	4,6
Requirements								
$h_w > 4D$			REJECT	REJECT	OK	OK	OK	OK
$A_{model} > A_{flume}$			OK	OK	OK	OK	OK	OK
$b_{scour} < b_{flume}$			REJECT	REJECT	OK	OK	OK	OK
$\theta > \theta_{cr}$ for live-bed scour			OK	OK	OK	OK	OK	REJECT
$\frac{1}{4}\theta < \theta < \frac{3}{4}\theta_{cr}$ for clear water scour			REJECT	REJECT	REJECT	REJECT	REJECT	OK
$Q < Q_{max}$			OK	OK	OK	OK	OK	OK
$Re > 4000$			OK	OK	OK	OK	OK	OK

Table A. 2: Summary of design

Width of flume	b_{flume}	40 cm
Height of flume	h_{flume}	40 cm
Pile diameter	D	5.0 cm
Sediment height	h_{sed}	15 cm
Water height	h_{water}	21 cm
Grain size	d	260 μ m
Average flow velocity in experiment	U	0.24 m/s

Appendix C.1: Notes on optical measurement on the scour depth

Design

Initially the height of the camera was estimated based on the desired sight during the experiment. An estimate was based on the estimated range of the sediment level around the pile and the specifications of the camera. The highest sediment level is the initial bed level. The smallest bed level that should be possible to capture is under the maximum scour depth. The maximum scour depth is estimated at $1.3D$, based on literature (e.g. Sumer et al., 2002a). Larger scour depths should be possible to measure too, but with reduced accuracy.

$$S_{\max} = 1.3 \cdot D = 1.3 \cdot 50 = 75 \text{ mm}.$$

As can be seen in appendix C.2 the used camera has a field of vision of 54° . Furthermore it needs 60 cm to have sharp vision and has a resolution of 480×680 pixels.

The range of the interesting region for the images is shown in figure A.1. The minimal height of the camera is calculated to be 49.1 mm above the original sediment level or 175.1 mm above the bottom of the pile. The interesting area has a distance to the camera of 55 – 127 mm. Note that minimal distance is out of focus. This is accepted, because the images are expected to be good enough to recognise the contrast between sand and water.

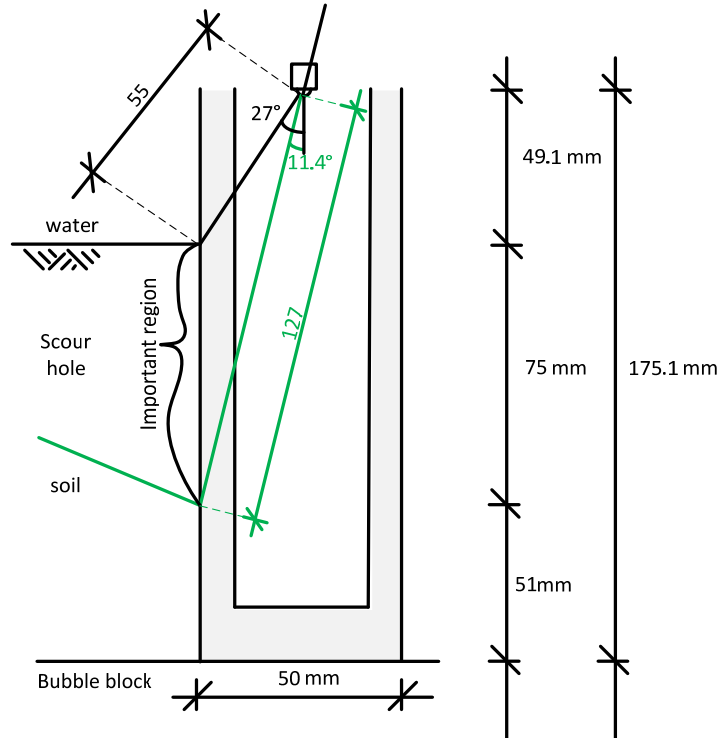


Figure A. 1: Visual range (green line is at maximal scour)

Practice

The above described calculation on the field of vision is performed to give an estimation only. In practice the image appeared to deviate from this estimation significantly due to a number of reasons:

- The camera recorded under a slight angle or offset. It decreases the range the image can record, so the camera should be put a bit higher. The angle and offset are not a problem for the processing later on, since it is small enough and is taken into account with the calibration.
- The Plexiglas may slightly distort the visual lines through refraction.
- The field of vision may not be exactly 54° .
- Initially it was aimed to have complete sight over the hole perimeter at every moment of time. This implied that the accuracy at larger scour depth was too low. This could be solved by moving the camera down and accept that the initially non-eroded bed is not visible over the whole perimeter, but only in the corners as in figure A.4. This is considered not to give any problems, since the height of the initial bed level is known.

As a result it was decided to place the camera approximately 29 mm lower. This is illustrated with the images in figure A.2 and A.3 from respectively before and after lowering. Here the a black and white striped paper was placed around the pile where the stripes were exactly 10 mm thick. Numbers were printed on the paper, to see the distance from the bottom.

Calibration

The image in figure A.4 is used for calibration. This is done in the flume, just before the sand was added, in order to be sure the location of the pile and the location of the camera remained the same. Throughout the experiments the camera was kept on a fixed position.

The image is much darker than the foregoing one, because it is taken after the pile was placed in the flume and less light was present there. A red stripe is drawn at the pile at a distance of 122 mm from the bottom of the pile to make corrections possible in case of any distortion during the experiments. Distortions did not occur though.



Figure A. 2: Calibration image according to design



Figure A. 3: Image as is used for calibration



Figure A. 4: Result at the start of experiments

Calibration is done by linking the pixels in the image to a vertical height. From the middle of the pile, recognisable from the white circle, the location of every black white edge on the red lines in figure A.5 is denoted. Here polar coordinates have been found to be convenient.

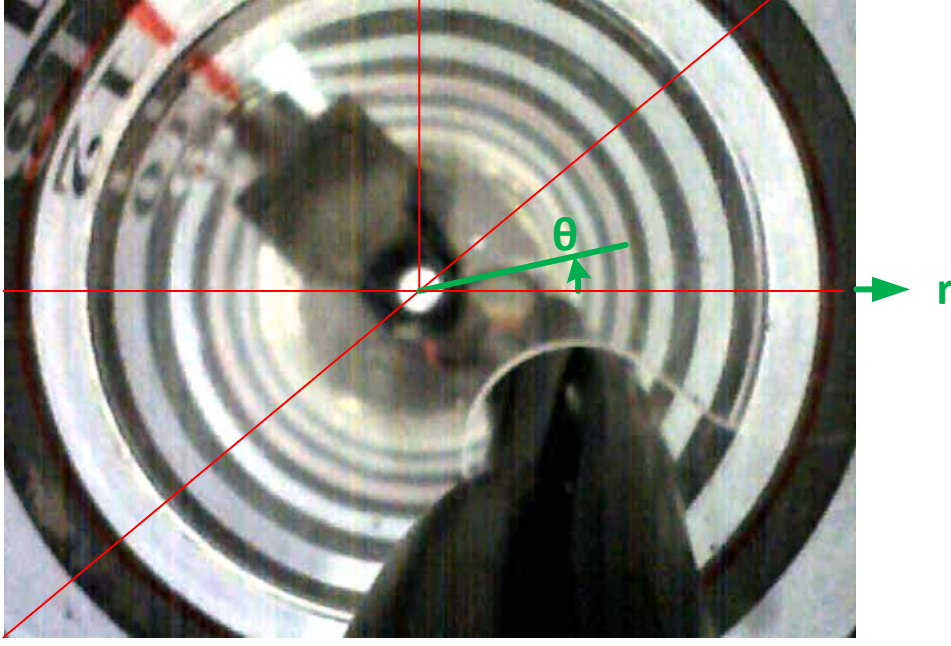


Figure A. 5: Definition of polar coordinates in calibration image (green) and lines used for calibration (red).

This results in four curves, which are shown in figure A.6. The curves nicely fall over each other, implying that the camera is not filming under an angle and that one relationship can be used for the relation between radius r and vertical height with respect to the bottom z_{image} . This most representative relation is obtained by fitting a fourth order polynomial through all the points in figure A.6.

$$\frac{z_{image}}{D} = -31.8 \left(\frac{r}{h_{image}} \right)^4 + 82.9 \left(\frac{r}{h_{image}} \right)^3 + -83.2 \left(\frac{r}{h_{image}} \right)^2 + 403 \left(\frac{r}{h_{image}} \right) + 5.67$$

Here $h_{image} = 480$ pixels, so the height of the image expressed in pixels. This relation should be determined every time the camera moves inside the pile, but since this pile was fixed during all the experiments, this relation is valid for all the experiments.

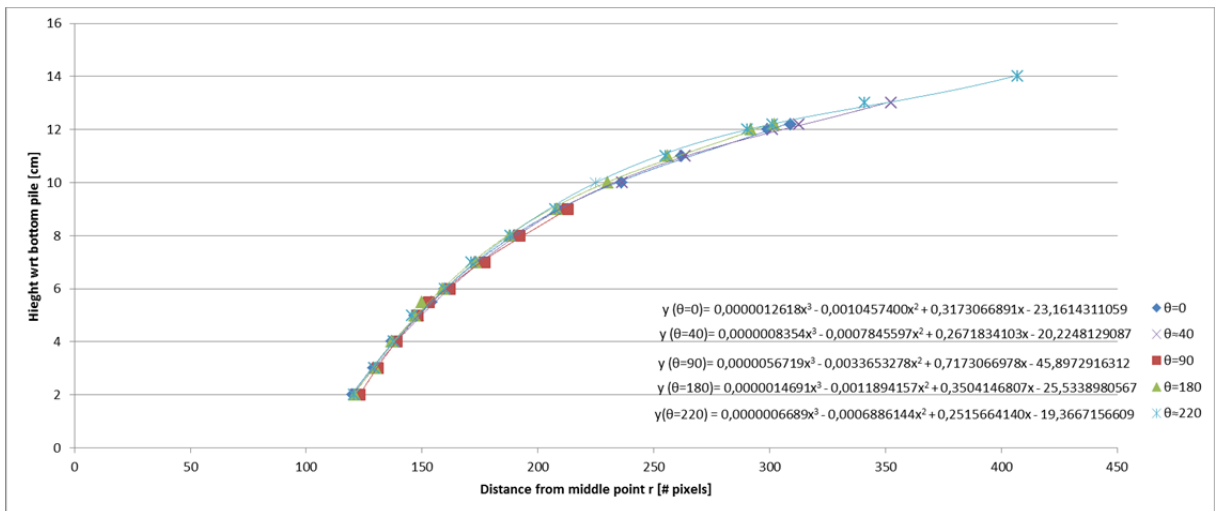



Figure A. 6: Result of calibration of the relation between pixel location and vertical height

Appendix C.2: Endoscope Voltcraft SB 16

Operating instructions and technical specifications of the used endoscope. This endoscope was chosen because it has a USB connection plug, so it can be recorded directly on a computer.



® OPERATING INSTRUCTIONS

BS-16 USB ENDOSCOPE

ITEM NO.: 51 69 61

INTENDED USE

This endoscope is a visual aid for optical fault diagnostics and inspection of deenergised systems and equipment.

The gooseneck including camera head is waterproof and suitable for use in watery liquids (but not acids or lyes). The handle itself is not waterproof and must not be exposed to or immersed in any liquid.

With its flexible gooseneck, the colour camera at the tip of the device can also reach into inaccessible positions.

The image transfer to the computer and its power supply are provided via an USB interface on the computer.


For safety and approval purposes (CE), you must not rebuild and/or modify this product. If you use the product for purposes other than those described above, the product may be damaged. In addition, improper use can cause hazards such as short circuiting, fire, electric shock etc. Read the instructions carefully and keep them. Make this product available to third parties only together with its operating instructions.

This product complies with the statutory national and European requirements. All company names and product names are trademarks of their respective owners. All rights reserved.

DELIVERY CONTENT

• Endoscope	• Software CD
• Magnet attachment	• Case
• Mirror attachment	• Operating instructions
• Hook attachment	

SAFETY INSTRUCTIONS

 Read the operating instructions carefully and especially observe the safety information. If you do not follow the safety instructions and information on proper handling in this manual, we assume no liability for any resulting personal injury or damage to property. Such cases will invalidate the warranty/guarantee.

a) Persons / Product

- The device is a precision tool. Do not drop it and do not subject it to any impacts.
- The basic device is not water-tight and therefore cannot be used underwater. Protect the base unit from splash water.
- The endoscope must only be used for inspection in powered-down systems. The camera head is made of metal and can lead to short-circuit.
- For reasons of safety, power down all system parts before any inspection.
- Always store the endoscope and its accessories in the case when not using them.
- Sensitive surfaces (with furniture polish, etc.) may cause chemical reactions with the casing.
- Never switch on the device immediately after it has been taken from a cold to a warm environment. Under adverse conditions, the resulting condensation could destroy the device. Allow the device to reach room temperature before switching it on.
- Attention, LED light: Do not look directly into the LED light! Do not look into the beam directly or with optical instruments!
- On industrial sites, the accident prevention regulations of the association of the industrial workers' society for electrical equipment and utilities must be followed.
- The device is not a toy. Keep it out of the reach of children and pets.
- Do not leave packaging material lying around carelessly. These may become dangerous playing material for children.
- Protect the product from extreme temperatures, direct sunlight, strong jolts, high humidity, moisture, flammable gases, vapours and solvents.
- Do not place the product under any mechanical stress.
- If it is no longer possible to operate the product safely, take it out of operation and protect it from any accidental use. Safe operation can no longer be guaranteed if the product:
 - is visibly damaged,
 - is no longer working properly,
 - has been stored for extended periods in poor ambient conditions or
 - has been subjected to any serious transport-related stresses.
- Please handle the product carefully. Jolts, impacts or a fall even from a low height can damage the product.
- Also observe the safety and operating instructions of any other devices which are connected to the product.

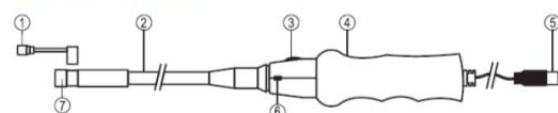
b) Miscellaneous

- Consult an expert when in doubt about operation, safety or connection of the device.
- Maintenance, modifications and repairs are to be performed exclusively by an expert or at a qualified shop.

If you are not sure about the correct connection or use, or if questions arise which are not covered by these operating instructions, please do not hesitate to contact our technical support or another qualified specialist.

Voltcraft®, Lindenweg 15, D-92242 Hirschau, Tel. +49 180/586 582 7.

OPERATING ELEMENTS



SYSTEM REQUIREMENTS

Pentium® III 200 MHz or higher
min. 32 MB RAM
40 MB free hard drive space
CD or DVD drive
Operating systems: Microsoft® Windows 98, ME, 2000, XP, Vista™, 7, 8

SOFTWARE

a) Installation


1. Ensure the endoscope is not connected to the computer.
2. Start your computer. Place the CD provided in your CD or DVD drive. Administrator rights are required for installation.
3. The installation will start automatically after the software CD has been inserted. If this is not the case, go to your CD-ROM drive and double-click on the "Telescope_Driver.exe" file to start the installation.
4. The security prompt for the "Windows Logo Test" will be displayed. This test will warn you that Windows® does not recognise the software. Click "Continue anyway" for confirmation. If you want to abort the installation, click the "Stop installation" button.
5. After confirmation of the security prompt, the installation will be automatically completed. A restart may be necessary, depending on the operating system. For this, read the Help section of Microsoft® Windows.

➔ The "Amcap" application is a universal program for a range of different devices. All menu items that are not described in these operating instructions are not part of the endoscope's range of functions.

b) Uninstallation

1. Navigate to the "Telescope Driver" menu folder in the Windows menu.
2. Click on "Uninstall" to start uninstalling and follow the instructions of the uninstall manager to complete the uninstallation.

OPERATION

 Only immerse the camera head and gooseneck in liquids that are deenergised. The gooseneck is not to be submerged further than the marking "IP67 max. water level".

The endoscope may only be used for inspection of deenergised systems. The camera head is made of metal so can lead to short-circuiting. For safety reasons, disconnect all system parts from the power supply before every inspection.

Do not go under the minimum bending radius of 60 mm.


a) Connecting the endoscope and starting software up

1. Turn your computer on and connect the USB connection plug (5) to a free USB port on your computer.
2. The computer will notify you of new hardware when connecting it for the first time. Follow the Windows instructions to install the drivers for the telescope.
3. Start the "Amcap" program from the "Telescope Driver" menu folder in the Windows menu.
4. Navigate to the "Devices" tab and select "Telescope Driver". Navigate to the "Options" tab and activate the menu item "Preview". The image will be displayed.

➔ If another USB camera has already been installed, it is possible that an error message comes up during the program start. In this case, in the main menu item "Devices" select the "Telescope Driver" driver.

b) Turning the camera lighting on

With the lighting control LED (3), you can set the camera head lighting intensity by turning it.



c) Main menu bar

File	Set Capture File...	Select storage location for video recordings (avi). The file must have the extension ".avi". You will be prompted to enter the file size.
	Allocate File Space...	Set storage size, and the available size will be displayed. In the "Capture File Size" menu item the size in megabyte (MB) can be entered.
	Save Captured Video...	Store a recorded video sequence.
	Exit	Exit program.
Devices	Telescope Driver	Select the menu item "Telescope Driver" for this product.
Options	Preview	Turn image display on and off
	Video Capture Filter...	see "d) Image settings"
	Video Capture Pin	<u>Video format:</u> <ul style="list-style-type: none"> Video standard (not changeable), Frame rate (set frame rate, do not alter 30 frames/sec), Colour space / Compression (preset to RGB 24, do not alter), Output size (preset to 640 x 480, do not alter) <u>Compression:</u> not changeable Confirm settings with "Apply" and then "OK".
Capture	Start Capture	Starts a video recording. Confirm with "OK", cancel with "Cancel".
	Stop Capture	End recording.
	Set Frame Rate...	Set frame rate for the recording (frames/sec). Leave the setting at 30 frames/sec. Confirm with "OK", cancel with "Cancel".
	Set Time Limit...	Input a maximum recording length in seconds. We recommend that this setting not be changed. Confirm with "OK", cancel with "Cancel".

Below the main image, the number of pictures captured is displayed in the status bar.

➔ The driver included in delivery is "TWAIN32-compatible". The camera can thus be operated with any program that supports this interface.

d) Image settings

Stream Property (Confirm settings with "OK", cancel with "Cancel")	<u>Image Control:</u> <ul style="list-style-type: none"> Image mirror (mirror image), Image flip (flip image around), Brightness (set brightness), Contrast (set contrast), Gamma (set contrast colour), Hue (set hue), Sharpness (set sharpness), VGA snap size (set image size, leave setting on 640 x 480), Zoom (set zoom in %) <u>Auto Mode Control (auto setting):</u> Leave ticked settings to achieve best possible image quality. <u>Default (basic settings):</u> <ul style="list-style-type: none"> Reset (reset settings), Save (save settings), Restore (restore basic settings) <u>In/Out Door (indoor/outdoor area):</u> <ul style="list-style-type: none"> Indoor (indoor area), Outdoor (outdoor area), <u>Flicker (flicker rate):</u> Set flicker rate <u>Extra Control (extras):</u> <ul style="list-style-type: none"> Backlight compensation (backlight), B/W Mode (black/white mode)
	<u>Effect (effects):</u> <ul style="list-style-type: none"> Disable, Invert, Black/White, Green Mono, Gray Scale, Blue Mono, Red Mono, Emboss, Find Edge, Mosaic, Wind, Solarize, Sepia, Bathroom, Sketch, Oil Paint, DistortH, DistortV, Monitor <u>Frame:</u> <ul style="list-style-type: none"> Disable, Flowers, Paper, Snipe (Sniper), Snowman

e) Snapshot

To make snapshots press the snapshot button **SNAP** (6). A further window with the snapshot picture will open:

File(F)	Save image in ".jpg" format (Save) Exit (Exit)
Rotate Orientation	Rotate image in selected angular degree.
Help(H)	Show information about program

➔ The snapshot function can only be carried out with administrator rights. Contact your system administrator for this.

f) Attachments

Carefully open the mounting ring of the attachments (1) for installation and attach it at the thin recess below the camera head. When opening, do not excessively bend the accessories (risk of breakage).

- The magnet attachment helps locate lost metal objects.
- The mirror attachment can extend the field of vision into areas that would otherwise be hardly accessible to the camera head.
- The hook attachment allows grasping small objects.

MAINTENANCE AND CLEANING

Do not submerge the main product in water!

The product requires no servicing aside from occasional cleaning. Use a soft, anti-static and lint-free cloth for cleaning.

Thoroughly rinse the endoscope's gooseneck after each use in liquids, using clean water and drying it before storing it in the case.

DISPOSAL



Electronic devices are recyclable waste and must not be disposed of in the household waste. At the end of its service life, dispose of the product according to the relevant statutory regulations.

You thus fulfil your statutory obligations and contribute to the protection of the environment.

TECHNICAL DATA

Operating voltage	5 V/DC via USB, 200 mA
USB interface	min. USB1.1
Camera sensor	CMOS 1/6"
Camera resolution	640 x 480 pixel (VGA)
Frame rate	30 fps
White balance	automatic
Exposure	automatic
Video format	AVI
Camera lighting	4 LEDs, white
Operating conditions	0 to +45 °C, 15 – 85 % RH
Storage conditions	-10 to 50 °C, 15 – 85 % RH
Bend radius	>60 mm
Camera head Ø	11.5 mm
Field of vision	54°
Focus	>60 mm
Gooseneck length	approx. 96 cm
Cable length	approx. 200 cm
Operating systems	Windows® 98, ME, 2000, XP, Vista™, 7, 8
Dimensions (L)	approx. 115 cm (without cable)
Weight	approx. 415 g

© Legal notice

These operating instructions are a publication by Volkcraft®, Lindemweg 15, D-82242 Hirschau/Germany. Phone +49 180/586 582 7 (www.volkcraft.de).

All rights including translation reserved. Reproduction by any method, e.g. photocopy, microfilming, or the capture in electronic data processing systems require the prior written approval by the editor. Reprinting, also in part, is prohibited.

These operating instructions represent the technical status at the time of printing. Changes in technology and equipment reserved.

© Copyright 2013 by Volkcraft®

Appendix C.3: Operations by Matlab to determine the scour depth

The measurement of the scour depth around the circumference of the pile is done with the endoscope. The endoscope is placed in the pile as described in appendix C.1. The movie is recorded with the provided software AMCAP. The raw records were recorded with a frequency of 15 frames/s and were extremely large in disk space since the data was not saved with an efficient Codec. Therefore the movies were converted with “Any Video Converter”, using an MPEG4 codec. This reduced the required hard disk space from 25 – 140 GB per test to 0.28 – 0.65 GB. This is without any significant data loss, since both the frame rate and the number of pixels were remained at 15 frames/s and 640 x 480 respectively.

The scour depth around the circumference is calculated by using Matlab. The operations that were necessary are explained here shortly.

The principle of the images is that from a pixel location, a vertical height can be found. Through the Plexiglas pile the border between the sand (dark tint) and the water (lighter tones) is clearly visible. The gray tone around the periment was unequal, because in the longitudinal direction of the flume more light was available. A calibration is performed before the execution of the experiments, see appendix C.1.

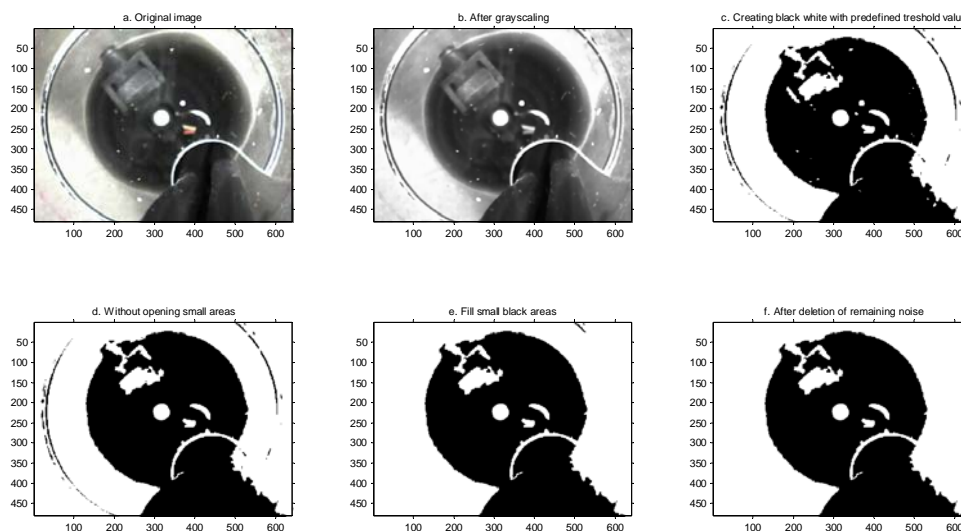


Figure A. 7: Procedure of image processing

Detection of the border

For the detection of the border in one image, the image is transformed to a grayscale threshold image (figure A.7a). Then a black and white image is made by making use of a threshold value. Above the threshold the result is white; below the threshold black is returned.

In the image still a number of disturbances are present. This includes:

- small white spots caused by dust;
- irregular larger white spots by reflections of the upper piezometer and a small white uncovered wire;

- the circular line shaped disturbance caused by reflexion of the Plexiglas plate which is used in the pile to prevent horizontal movement of the wires; and
- the part of the circumference that cannot be investigated due to wires and a piezometer.

In order to overcome most of the problems a number of measures are taken:

- The small noise is filtered out by filling them, using a minimum number of pixels that forms an area. If the area is smaller than a given value, it is filled. The results is figure A.7d
- In the same way the black noise is filtered away (see figure A.7e).
- Some black spots remain, because they are connected to a side of the image. These are removed by filling the area of manually chosen points (figure A.7f or A.8a).
- In order to filter out the left disturbances, an area is selected in which the images are considered to be reliable enough. The selected area is shown in figure A.8b). Now the edge is determined within the predefined area (figure A.8c). The selected edge is projected on the original image in figure A.8d.

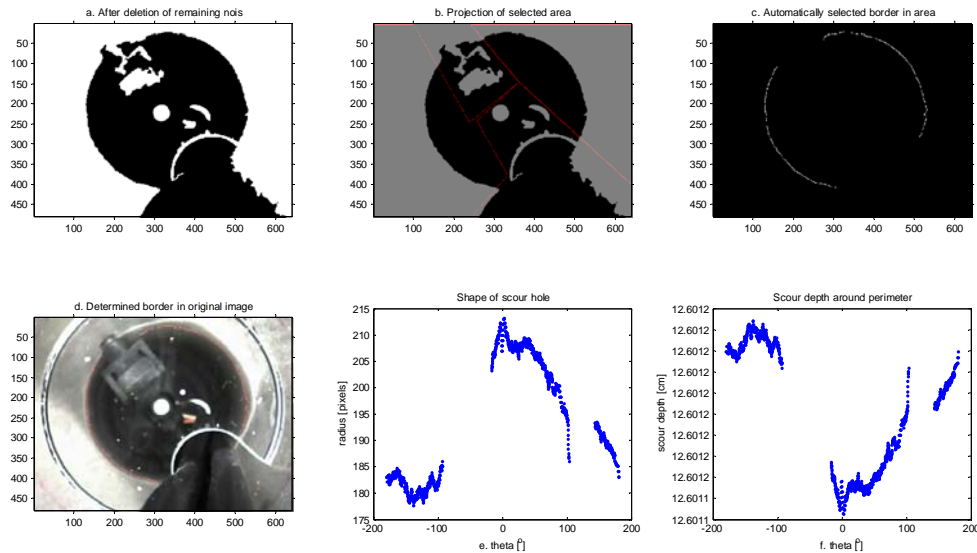


Figure A. 8: Continued procedure of image processing

Now for every white pixel, as shown in figure A.8c, the distance to the centre is determined. This is still a distance, expressed in number of pixels. In figure A.6 (appendix C.1) the graph is shown for the calibration of the images. This graph shows the relation between the distance in pixels and the scour depth. This distance is used to determine the plot of the scour depth over the perimeter (figure A.8f)

Detection of middle of pile

The centre of the pile is used in the procedure to determine the scour depth. This is also retrieved automatically from the images. From an arbitrary image from the movie, shown in figure 9a, a manually defined region is selected in which the centre is searched for (figure 9b). The figure is transformed in a grey scaled image, where the grey tone is a number between 0 and 1. The middle white circle is captured by defining a threshold level which returns the middle circle (figure A.9c). For this circle the middle is calculated. The result is the border of the circle as shown in figure A.9d to be able to check the edge detection and the location of the middle of this circle.

The coordinates, expressed in pixels can be used to check whether the camera didn't move throughout the experiments. This indeed did not happen. In case the pile would have moved this is corrected directly, since the middle is determined automatically in every test.

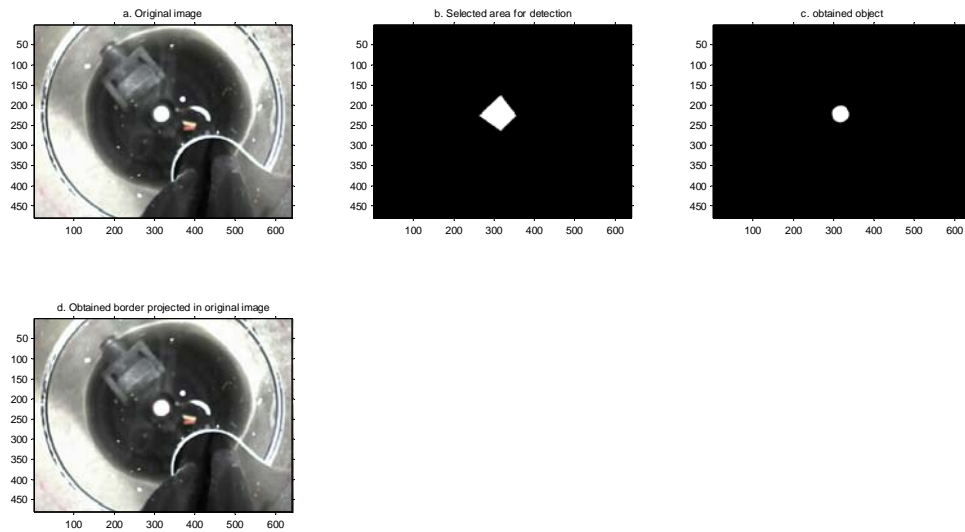


Figure A. 9: Detection of the centre of the pile in the images

Appendix C.4: Matlab script on determination scour depth

```

%%% LOAD MOVIE WITH SCOUR DATA AND IMAGE PROCESSING TO TIME CURVE
%Made by Ferdinand van den Brink
%Thesis project: Effect of liquefaction on scour around offshore monopile foundations
clc; close all; clear all; tic;

%% Settings
setting.saveit = 0; % Safe scour depth data || 0=uit 1=aan
setting.nFrames = 250; % Number of frames to show in time curve
setting.minpix = 500; % Minimum number of pixels for image processing. Discard otherwise
setting.level = 0.45; % Determine grayscalelevel for for black-white. Lower is darker.
setting.midlevel= 0.75; % Determine grayscalelevel for for black-white for middetection.
setting.begin_t = 130; %1*60 +00; % in seconds. MIN*60 + SEC
setting.testnum = '018'; % Number of the test which is going to be examined

%% Constants
const.g = 9.81 ;% m/s
const.rhos = 2650 ;% kg/m3
const.rho = 1000 ;% kg/m3
const.d = 260*10^-6;% m
const.D = 0.05 ;% m

%% Load data
addpath(path, 'D:\Ferdinand\School\Universiteit\Afstuderen\DataScourDepth\Video\Omgezet');
% addpath(path, 'D:\Ferdinand\School\Universiteit\Afstuderen\DataScourDepth\Video');
film = VideoReader(['Test' setting.testnum '.avi']);
setting.framert = film.NumberOfFrames/film.Duration;
Calibrations; %Load calibration
data. Here only for transformation to St

%% Determine middle of images
mid.beeld = read(film, film.numberofFrame/2); %Use frame halfway during the
series.
mid.bewerkt = bwareaopen(im2bw(rgb2gray(mid.beeld),setting.midlevel),
setting.minpix);
% points = [1 2 3 4 ]; %Region of intrest
mid.row = [173 224 263 224]; %Region of intrest
mid.col = [315 353 315 262]; %Region of intrest
mid.select = (roipoly(mid.beeld, mid.col, mid.row)); %make an area of pointsmaak
gebied van punten
mid.obj = mid.select.*mid.bewerkt; %Use only data within area
mid.kleur = ind2rgb(edge(mid.obj), [0.0, 0.0, 0.0; 0.0, 1.0, 0.0]); %Make the
figure black with red line
mid.rand = imadd(mid.beeld, uint8(round(mid.kleur*255))); %Add red line to
original image
mid.center = regionprops(mid.obj,'Centroid'); %Determine the coordinates of
the centre

%% Image processing
% Create empty structure to transfer data to
beeld(1:setting.nFrames) = struct('cdata', zeros(film.Height, film.Width,3 , 'uint8'),...
'colormap', []);
for k = 1:setting.nFrames % Processing for every image
temp.FrameID = round(setting.begin_t*setting.framert) + round(((film.numberofFrames -
(setting.begin_t*setting.framert))/(setting.nFrames-1))*(k-1));
if temp.FrameID < 1
temp.FrameID = 1;
elseif temp.FrameID > film.numberofFrames
temp.FrameID = film.numberofFrames;
else
end
beeld(k).cdata = read(film, temp.FrameID);
temp.a = beeld(1,k).cdata;
temp.c = im2bw(rgb2gray(temp.a),setting.level); %Make grayscaled
temp.d = imcomplement(bwareaopen(imcomplement(bwareaopen(temp.c,
setting.minpix)), setting.minpix)); % Fill small white and black spots.
temp.f = imcomplement(bwselect(imcomplement(temp.d),300,300,4));%Select only
middle region to prevent undesired points on the border

% Define area of intrest
% punt = [1 2 3 4 5 ];
rand.row = [480 350 250 350 480 ];
rand.col = [1 1 250 300 100 ];
rand.select = (roipoly(temp.a, rand.col, rand.row));

```

```

        rand.rand      = rand.select.* edge(temp.f,'canny');          %Determine edge within selected
region
        rand.randfig(k).cdata= imlincomb(0.85, temp.a, 1, uint8(round(ind2rgb(edge(rand.rand),
[0.0, 0.0, 0.0; 1.0, 0.0, 0.0])*255))); %Add red line on original images
        [rand.leeg.row, rand.leeg.col, rand.leeg.val] = find(rand.rand);          %Find pixel
coordinate of the border
        rand.r          = sqrt((rand.leeg.row - mid.center.Centroid(2)).^2 + (rand.leeg.col -
mid.center.Centroid(1)).^2); %Determine radial coordinate of pixel
        rand.theta      = atan2d(-(rand.leeg.row - mid.center.Centroid(2)),rand.leeg.col -
mid.center.Centroid(1)); %Determine theta of pixel
        for i = 1: length(rand.theta); %Make theta always larger than 0
            if rand.theta(i)<0;
                rand.theta(i) = rand.theta(i) + 360;
            end
        end

        % Filter out erroneous points
        rand.indweg      = find (abs(rand.r - mean(rand.r))>0.2* mean(rand.r));
        rand.r(rand.indweg)      = NaN;
        rand.theta(rand.indweg)  = NaN;
        res.r(k)      = mean (rand.r);          %Use the mean of all pixels for the radius
        res.theta(k)   = mean (rand.theta);
        res.t(k)       = (temp.FrameID/setting.framert) -
round(setting.begin_t*setting.framert)/setting.framert;
        end

        res.St          = (15 - 2.4 - (cal.calS(1).* res.r.^4 + cal.calS(2).* res.r.^3 +
cal.calS(3).* res.r.^2 + cal.calS(4).* res.r + cal.calS(5) )); %Calculations of S
        res.t_sec       = [res.t];
        res.t_dimles     = res.t_sec.*sqrt(const.g.*((const.rhos-
const.rho)./const.rho).^3)./const.D.^2;
        res.t_min        = res.t_sec./60; % tijd omgerekend naar minuten

%% Save time development of scour data
if setting.saveit == 1 && setting.nFrames > 200;
    disp(' ')
    disp('Time curve scour was saved')
    St = res.St;
    t_sec = res.t_sec;
    titel=(['Scourdepth_Test' setting.testnum '.txt']);
    save(titel,'-ascii','St','t_sec');
    clear St t_sec;
elseif setting.saveit == 1 && setting.nFrames<=200;
    disp(' ')
    fprintf(2,'ERROR: Number of frames too small to save data series \n');
    disp('Time curve scour was NOT saved')
else
    disp(' ')
    disp('Time curve scour was NOT saved')
end

rmpath('D:\Ferdinand\School\Universiteit\Afstuderen\DataScourDepth\Video\Omgezet');

```

Appendix D.1: Water pressure gauge – Technical specifications

The water pressure sensors that have been used are 0.5psi non-compensated Straight pressure sensors measuring the differential between the two ends of the sensors. By the fabricant these gauges are shortly denoted as 24PCEFA6D.

Relevant technical information can be found in the information leaflet as given below.

Pressure Sensors

24PC Series

Gage and Differential/Unamplified-Noncompensated

SENSOR SELECTION GUIDE

2 Product Family	4 Circuit Type	PC Pressure Transducer	A Pressure Range	F* Type of Seal	A Type of Port	2 Termination Style	G Pressure Measurement
2 20PC family	4 Noncom- pensated		A 1 psi B 5 psi C 15 psi D 30 psi E 0.5 psi F 100 psi G 250 psi	F Fluorosilicone	A Straight B Barbed C Luer D Modular H M5 Thread I 90° Port J Needle M 1/4 - 28 UNF Thread	1 1 x 4 2 2 x 2	G Gage D Differential

Example: 24PCAFA2G

Standard, non-compensated 1 psi sensor with fluorosilicone seal, straight port, 2 x 2 terminals, and Gage pressure measurement.

*Other media seal materials may be available.

ACCESSORIES SELECTION GUIDE

Catalog Listing	Description
PC10182	Steel lockring (Included with Port Style A, 1 x 4 terminals only)
PC10949	Single hole plastic bracket (Must be separately ordered)

Not all combinations are established.
Contact 800 number before final design.
The following listings are typically
stocked in small quantities.

Unamplified

Pressure Sensors

Gage and Differential/Unamplified-Noncompensated

24PC Series

Basic Sensors



FEATURES

- Lowest priced pressure sensor
- Miniature package
- Variety of gage pressure port configurations - easily and quickly modified for your special needs

- Choice of termination for gage sensors
- 2 mA constant current excitation significantly reduces sensitivity shift over temperature*
- Can be used to measure with vacuum or positive pressure

24PC SERIES PERFORMANCE CHARACTERISTICS at 10.0 ±0.01 VDC Excitation, 25°C

	Min.	Typ.	Max.	Units
Excitation	---	10	12	VDC
Null Offset	-30	0	+30	mV
Null Shift, 25° to 0°, 25° to 50°C	---	±2.0	---	mV
Linearity, P2 > P1, BFSL	---	±0.25	±1.0	%Span
Sensitivity Shift, 25° to 0°, 25° to 50°C	---	±5.0*	---	%Span
Repeatability & Hysteresis	---	±0.15	---	%Span
Response Time	---	---	1.0	msec
Input Resistance	---	5.0 K	---	ohms
Output Resistance	---	5.0 K	---	ohms
Stability over One Year	---	±0.5	---	%Span
Weight	---	2	---	grams

ENVIRONMENTAL SPECIFICATIONS

Operating Temperature	-40° to +85°C (-40° to +185°F)
Storage Temperature	-55° to +100°C (-67° to +212°F)
Shock	Qualification tested to 150 g
Vibration	Qualification tested to 0 to 2 kHz, 20 g sine
Media (P1 & P2)	Limited only to those media which will not attack polyetherimide, silicon and fluorosilicone seal

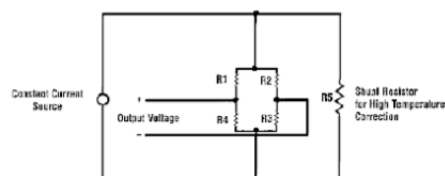
24PC SERIES ORDER GUIDE

Catalog Listing	Pressure Range psi	Span, mV			Sensitivity mV/psi Typ.	Overpressure psi Max.
		Min.	Typ.	Max.		
24PCE Type	0.5	24	35	46	70	20
24PCA Type	1.0	30	45	60	45	20
24PCB Type	5.0	85	115	145	23	20
24PCC Type	15	165	225	285	15	45
24PCD Type	30	240	330	420	11	60
24PCF Type	100	156	225	294	2.25	200
24PCG Type	250	145	212	280	0.85	500

* Non-compensated pressure sensors, excited by constant current instead of voltage, exhibit temperature compensation of Span. Application Note #1 briefly discusses current excitation.

Constant current excitation has an additional benefit of temperature measurement. When driven by a constant current source, a silicon pressure sensor's terminal voltage will rise with increased temperature. The rise in voltage not only compensates the Span, but is also an indication of die temperature.

Constant Current Excitation Schematic



Pressure Sensors

Gage and Differential/Unamplified

22/24/26PC Series

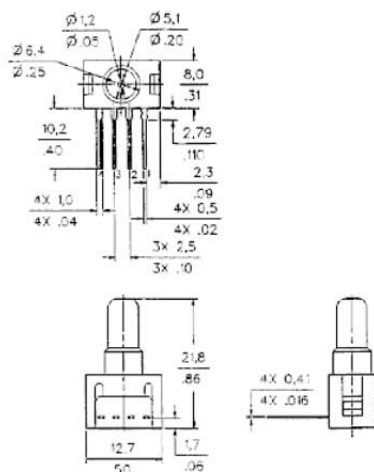
MOUNTING DIMENSIONS (for reference only)

GAGE SENSOR

Pressure is applied to port P2.
Port P1 vents to ambient pressure.

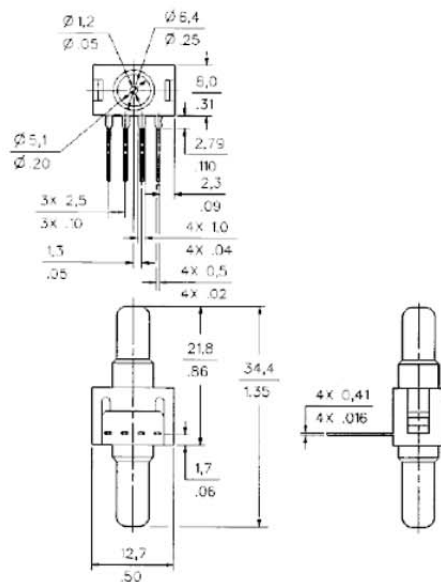
"1 x 4" Termination (Style 1), Port Style A, Straight

Pin 1 is notched, and is shown at the right of the package.
Pin 2 is next to pin 1, etc.



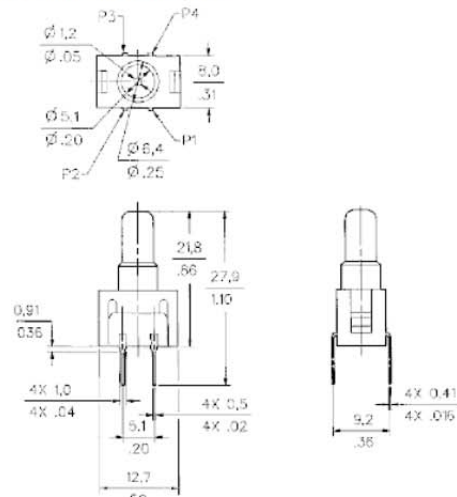
DIFFERENTIAL SENSOR

Straight Port, 1 x 4 termination (Style 2) ONLY
Port P1 is near terminals.



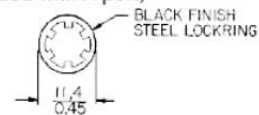
"2 x 2" Termination (Style 2), Port Style A, Straight

Pin 1 is notched, and is shown at lower right corner.
Pins 2, 3 and 4 are clockwise.

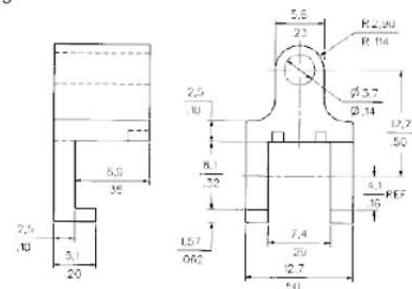


ACCESSORIES

Locking (included with A port)
PC10182



Single hole Plastic Bracket (purchase separately)
PC10949

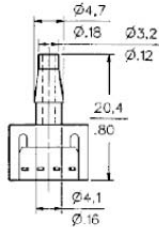


Gage and Differential/Unamplified

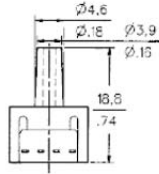
22/24/26PC Series

OTHER GAGE SENSOR PORT STYLES (2 x 2 or 1 x 4 Termination)

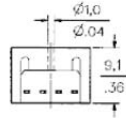
B Barbed



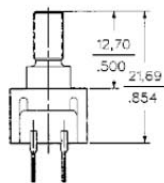
C Luer



D Modular



H M5 Thread



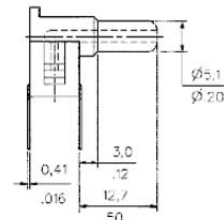
O-Ring

Size 007

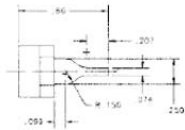
O-Ring Counterbore

.040" deep $\pm .005 \times .30 \pm .003$ "

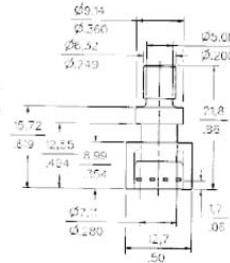
190°



J Needle



M 1/4-28 UNF Thread



O-Ring

Size 009

O-Ring Counterbore

.040" deep \pm .002 \times .360" \pm .003"

20PC SERIES CIRCUIT - NOTES

1. Circled numbers refer to Sensor Terminals (interface pins).
2. V_0 increases with pressure change.
3. $V_0 = V_2 - V_4$
4. Pin 1 designated with a notch.

Pin Designation

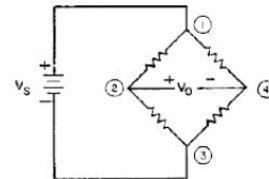
Pin 1 $V_S (+)$

Pin 2	Output (+)
Pin 3	Output (-)

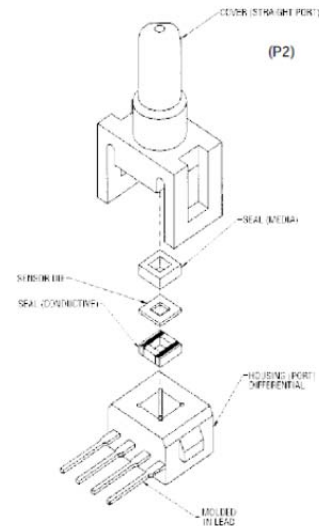
Pin 3	Ground (-)
Pin 4	Output (+)

Pin 4 Output (-)

EXCITATION



20PC Construction



Unamplified



**Instruction Leaflet
Bedienungsanleitung
Feuille d'instructions**

Uncompensated Pressure Transducers

G

Nichtkompensierte Druckmeßumformer

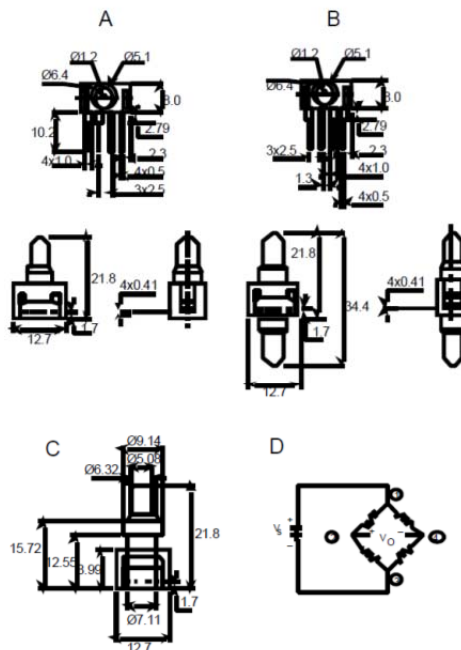
I

Trasduttori di pressione non compensati

I

Figures / Abbildung / Figura

①



G

Mounting dimensions

- A. Gauge style-
Pressure is applied to port P2.
Port P1 vents to ambient pressure.
Pin 1 is notched, and is shown at the right of the package.
Pin 2 is next to pin 1, etc.
- B. Differential style-
Port 1 is near terminals
- C. Gauge style, 100 & 250psi only.
1/4-28 UNF Thread
- D. Electrical connections
Both types

Notes:-

1. Circled numbers refer to sensor terminals
2. Vo increases with pressure change P2>P1

Terminals:-

1. Pin 1 = Vs (+)
2. Pin 2 = Output (+)
3. Pin 3 = Ground (-)
4. Pin 4 = Output (-)
- Pin 1 is notched, labeled on plastic.
Pin 2 next to Pin 1, etc.

I

Einbaumaße

- A. Manometerausführung-
Der Druck wird auf den Anschluß P2 angelegt.
Der Anschluß P1 sorgt für den Umgebung-sdruck.
Stift 1 ist eingekerbt und auf der rechten Seite dieser Ausführung abgebildet.
Stift 2 befindet sich in der Nähe von Stift 1 usw.
- B. Differentialausführung
Anschluß 1 befindet sich in der Nähe der Klemmen.
- C. Manometerausführung nur 100 & 250psi. 1/4 -28 UNF Gewinde
- D. Elektrische Anschlüsse
Beide Ausführungen

Hinweise:

1. Die eingekreisten Ziffern beziehen sich auf Sensoranschlüsse.
2. Vo steigt bei Druckänderung P2>P1 an.

Anschlüsse:

1. Stift 1 = VS (+)
2. Stift 2 = Ausgang (+)
3. Stift 3 = Erde (-)
4. Stift 4 = Ausgang (-)
- Stift 1 ist eingekerbt, auf Kunststoff markiert.
Stift 2 in der Nähe von Stift 1 usw.

I

Dimensioni di montaggio

- A. Modello a indicatore-
La pressione viene applicata alla porta P2.
Porta P1 per lo sfogo alla pressione ambiente.
Il piedino 1 è intagliato ed è mostrato sulla destra della confezione.
Il piedino 2 è accanto al piedino 1, ecc.
- B. Modello a differenziale -
La porta 1 è vicina ai terminali
- C. Modello a indicatore, solo 100 e 250psi.
Filettatura UNF 1/4-28
- D. Collegamenti elettrici
Entrambi i modelli

Note:-

1. I numeri nei cerchietti si riferiscono ai terminali del sensore
2. Vo aumenta con il cambiamento di pressione P2>P1

Terminali:-

1. Piedino 1 = Vs (+)
2. Piedino 2 = Uscita (+)
3. Piedino 3 = Massa (-)
4. Piedino 4 = Uscita (-)
- Il piedino 1 è intagliato ed è etichettato su plastica.
Il piedino 2 è accanto al piedino 1, ecc.

V10591



RS Stock No.

Gauge 235-5762, 235-5784, 235-5807
235-5829, 235-5841, 235-5863, 235-5891
Differential 235-5778, 235-5790, 235-5813
235-5835, 235-5857, 235-5885, 235-5908

General

These pressure transducers are available in either a gauge or differential package. They are all based on a four active element piezo resistive bridge construction.

The gauge sensors use atmospheric pressure as a reference whereas the differential sensors will accept two independent pressure sources simultaneously.

Most sensors are supplied complete with steel locking, however, the gauge versions of 100psi and 250psi have threaded parts (1/4 - 28UNF) to assist in pipeline connections.

Measurand

Input media are limited to those media which will not attack polyetherimide, fluorosilicone, or silicon.

Soldering

Limit soldering temperature to 315°C for 10 seconds duration maximum.

Cleaning

Apply cleaning fluids appropriate to the contaminants to be removed.

Selection chart

Type	RS stock no.
Gauge	
0.5psi	235-5762
1.0psi	235-5784
5.0psi	235-5807
15psi	235-5829
30psi	235-5841
100psi (1/4 - 28 unf)	235-5863
250psi (1/4 - 28 unf)	235-5891
Differential	
0.5psi	235-5778
1.0psi	235-5790
5.0psi	235-5813
15psi	235-5835
30psi	235-5857
100psi	235-5885
250psi	235-5908

Technical Specification

(All figure are typical unless otherwise stated)

	0.5psi	1.0psi	5.0psi	15psi	30psi	100psi	250psi
Full scale output;mV	35	45	115	225	330	225	212
Sensitivity per psi, mV	70	45	23	15	11	2.25	0.85
Overpressure (max)	20	20	20	45	60	200	500
Recommended Excitation	10v	10v	10v	10v	10v	10v	10v
Input resistance ohms	5k	5k	5k	5k	5k	5k	5k
Media Compatibility	Limited to those which will not attack polyetherimide, silicon or fluorosilicone						

RS Components shall not be liable for any liability or loss of any nature (howsoever caused and whether or not due to RS Components negligence) which may result from the use of any information provided in RS technical literature.



RS Best-Nr.

Manometer 235-5762, 235-5784, 235-5807
235-5829, 235-5841, 235-5863, 235-5891
Differential 235-5778, 235-5790, 235-5813
235-5835, 235-5857, 235-5885, 235-5908

Allgemeines

Diese Meßwertumformer sind entweder in Manometer- oder Differentialausführung erhältlich. Die Basis dieser Umformer bildet eine aus vier aktiven Elementen bestehende piezoresistive Meßbrückenkonstruktion.

Die Manometersensoren benutzen atmosphärischen Druck als Referenz, während die Differentialsensoren gleichzeitig zwei unabhängige Druckquellen akzeptieren.

Die meisten Sensoren werden komplett mit Sicherungsring aus Stahl geliefert. Die Manometerausführungen 100psi und 250psi haben Gewindeteile (1/4 - 28UNF), was ihren Einsatz in Pipeline-Verbindungen ermöglicht.

Medienverträglichkeit

Es dürfen nur Mittel eingelassen werden, die weder Polyetherimid noch Siliziumfluor oder Silizium angreifen.

Löten

Die Löttemperatur ist auf 315°C für die Dauer von max. 10 Sekunden begrenzt.

Reinigen

Je nach Art der Verschmutzung entsprechende Reinigungsmittel auftragen.

Bestelltablelle

Typ	RS Best Nr.
Manometer	
0.5psi	235-5762
1.0psi	235-5784
5.0psi	235-5807
15psi	235-5829
30psi	235-5841
100psi (1/4 - 28 unf)	235-5863
250psi (1/4 - 28 unf)	235-5891
Differential	
0.5psi	235-5778
1.0psi	235-5790
5.0psi	235-5813
15psi	235-5835
30psi	235-5857
100psi	235-5885
250psi	235-5908

Technische Daten

(Gelten für alle Bestellnummern, wenn nichts anderes angegeben ist)

	0.5psi	1.0psi	5.0psi	15psi	30psi	100psi	250psi
Vollbereichendwert;mV	35	45	115	225	330	225	212
Empfindlichkeit nach psi, mV	70	45	23	15	11	2.25	0.85
Überdruck (max.)	20	20	20	45	60	200	500
Empfohlene Versorgung	10v	10v	10v	10v	10v	10v	10v
Eingangswiderstand in Ohm	5k	5k	5k	5k	5k	5k	5k
Medienkompatibilität	Ist auf diejenigen begrenzt, die Polyetherimid, Silizium oder Siliziumfluor nicht angreifen.						

RS Components haftet nicht für Verbindlichkeiten oder Schäden jedweder Art (ob auf Fahrlässigkeit von RS Components zurückzuführen oder nicht), die sich aus der Nutzung irgendwelcher der in den technischen Veröffentlichungen von RS enthaltenen Informationen ergeben.

Appendix D.2: Water pressure gauge – Calibration

After the water pressure gauges are installed in the Plexiglas pile, the gauges are calibrated. For different water heights the amplified signal from the gauges is measured with volt meters. The water height is measured with respect to the bottom of the pile. The amplification of the signal is 125. The water height was determined with respect to the bottom of the pile, but are transformed to piezometric pressure based on the geometry of the pile. The location of the water pressure gauges is shown in detail sketch in figure A.10. A photo from the pile is shown in figure A.11. Note that above piezometer 4 a Plexiglas plate is installed to provide for horizontal stability of the cables.

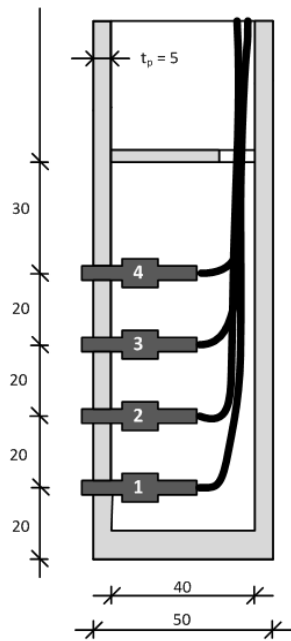


Figure A. 10: Geometry of the location of the piezometers (in mm)



Figure A. 11: Pile with piezometers

The result of the calibration is shown in figure A.12.

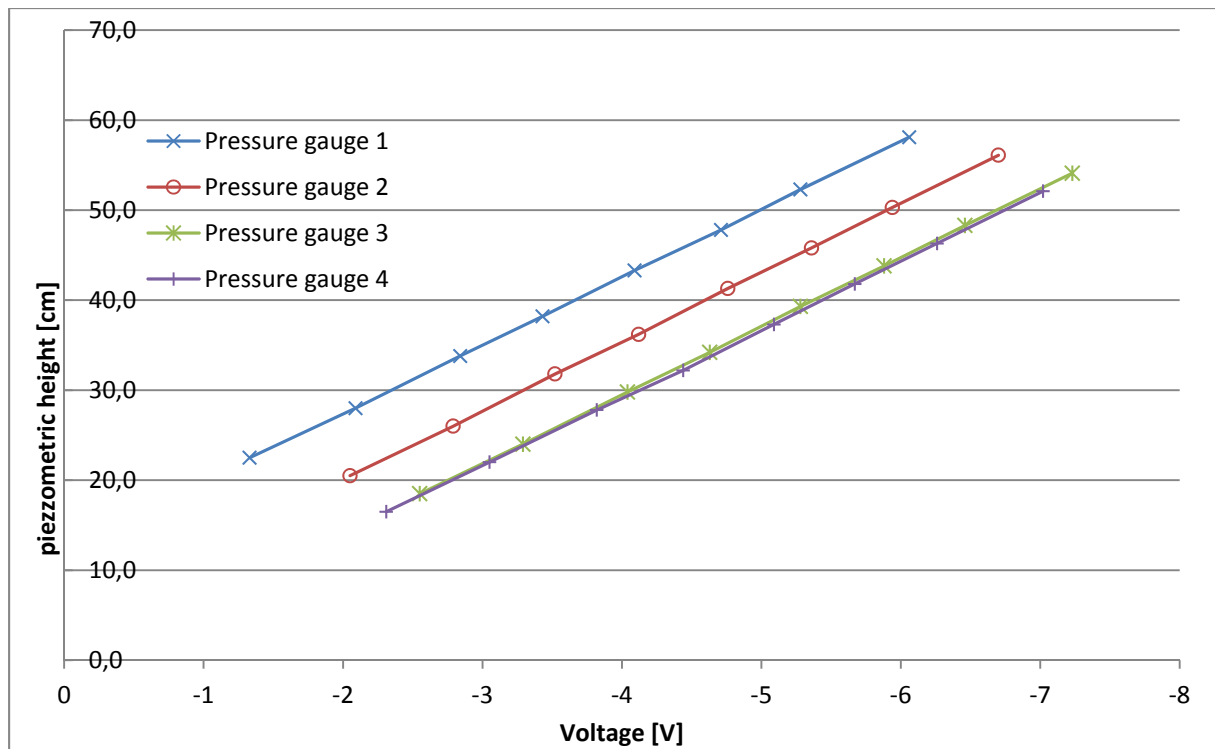


Figure A. 12: Calibration of piezometric height

Appendix D.3: Result of pore water pressure measurements

The result of the pore water pressure measurement is shown per piezometer in figure A.13 till A.16. Finally, the pore water pressure distribution is given at $t^* = 2.7$, $t^* = 5.4$, $t^* = 7.42$, $t^* = 14.8$, $t^* = 27$ and $t^* = 33.1$ in figure 17 till 22. The time development of the pore water pressure distribution is given per test in figure A.23 till A.28.

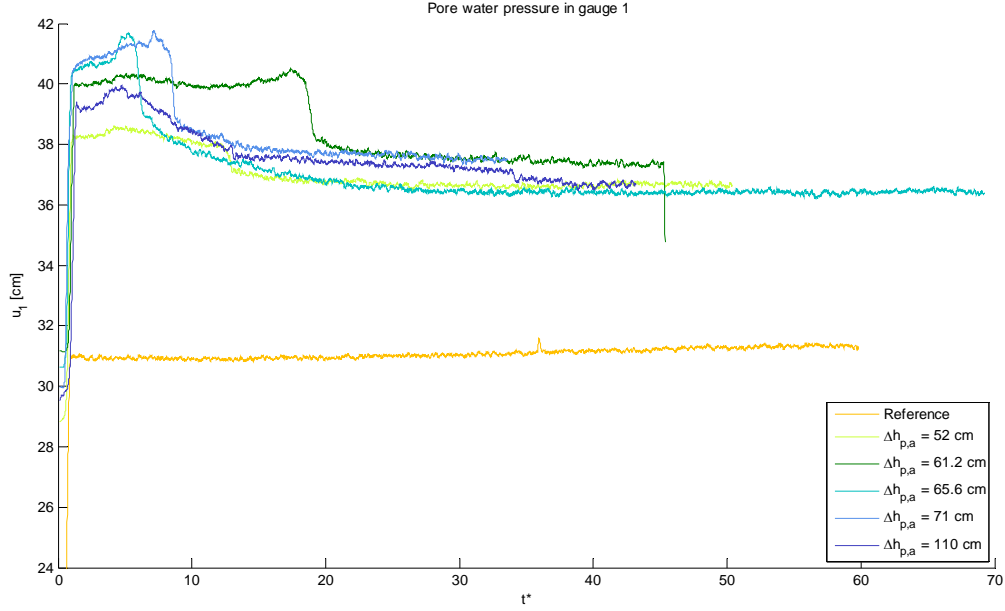


Figure A. 13: Time curve of pore water pressure in piezometer 1 (bottom one)

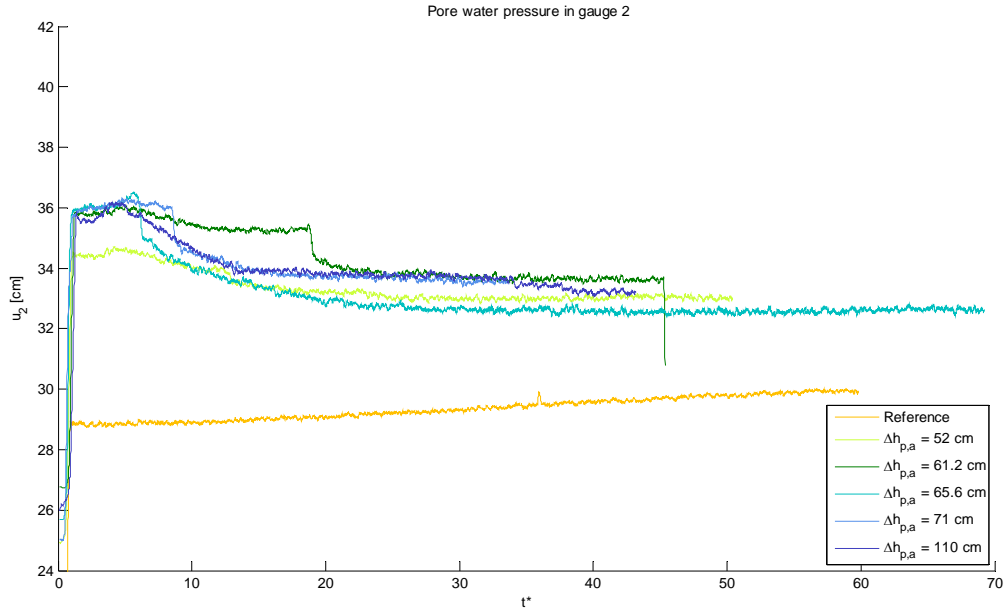


Figure A. 14: Time curve of pore water pressure in piezometer 2

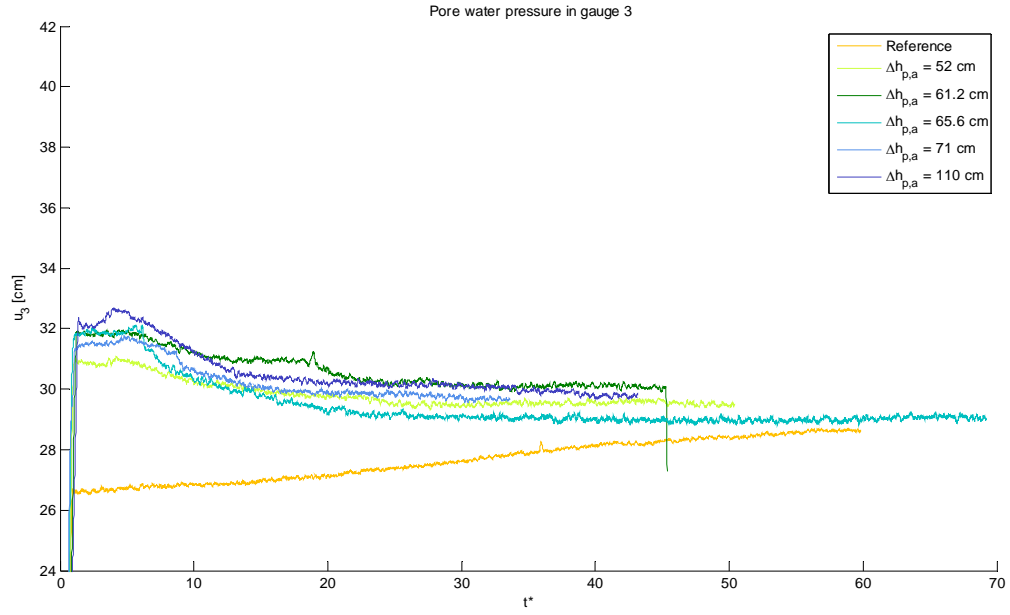


Figure A. 15: Time curve of pore water pressure in piezometer 3

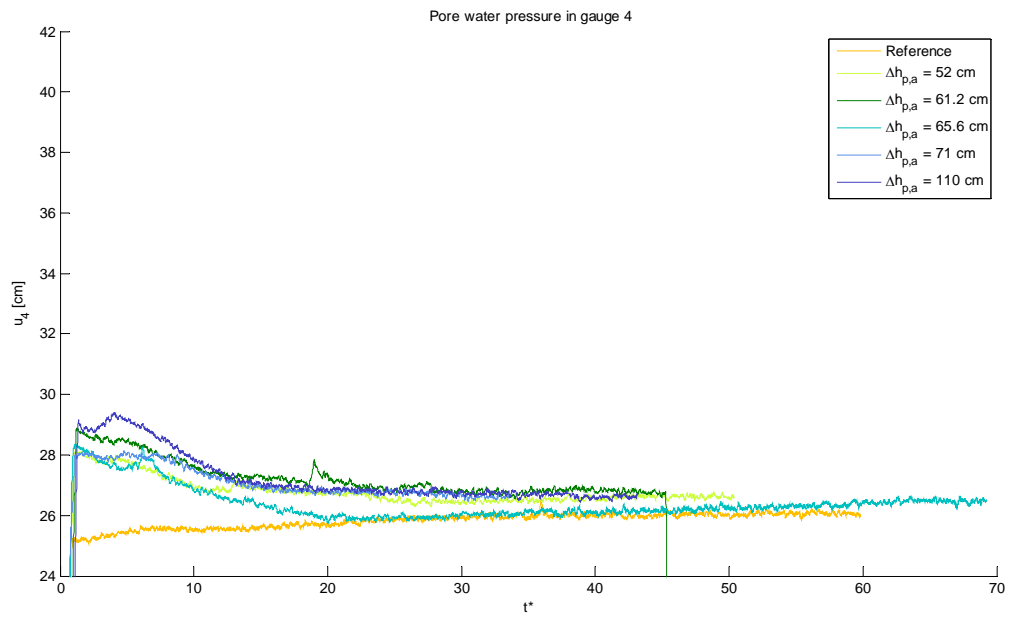


Figure A. 16: Time curve of pore water pressure in piezometer 4 (top one)

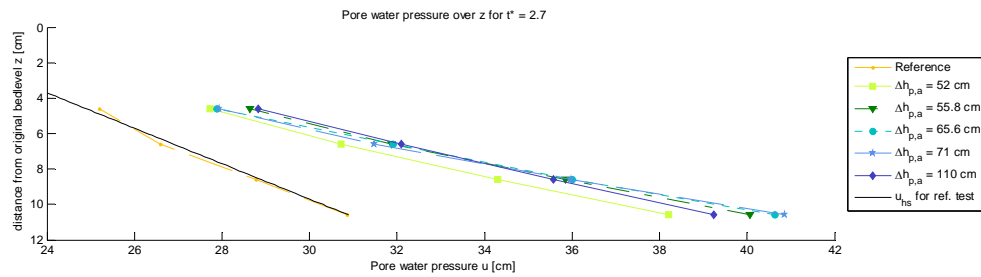


Figure A. 17: Pore water pressure distribution over depth at $t^* = 2.7$

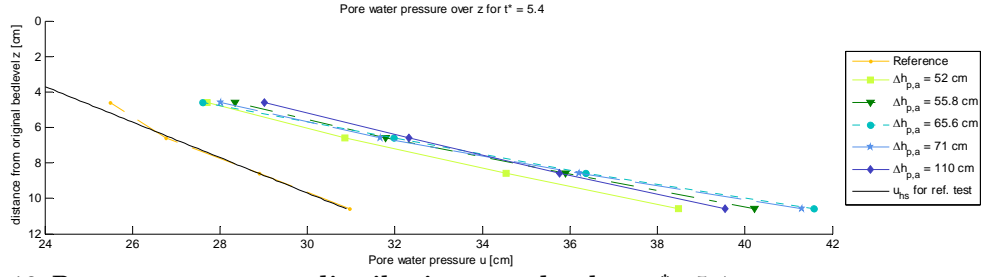


Figure A. 18: Pore water pressure distribution over depth at $t^* = 5.4$

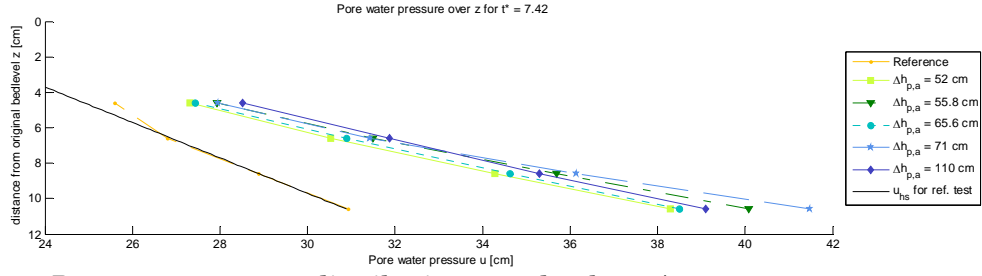


Figure A. 19: Pore water pressure distribution over depth at $t^* = 7.42$

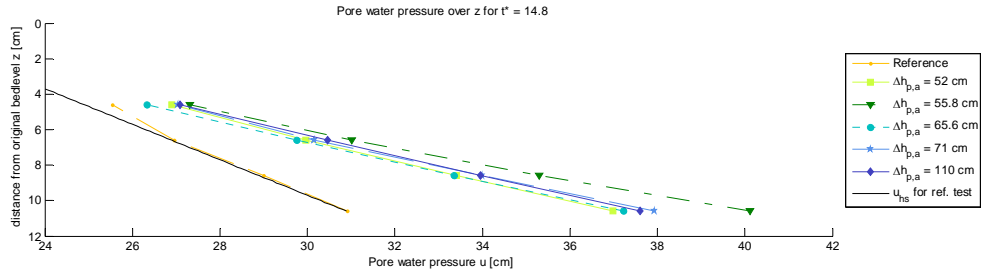


Figure A. 20: Pore water pressure distribution over depth at $t^* = 14.8$

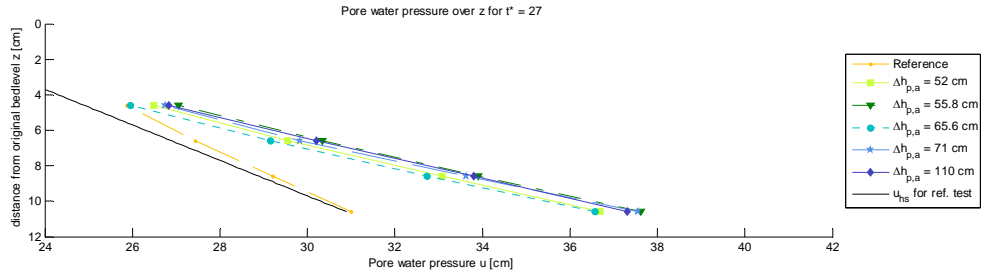


Figure A. 21: Pore water pressure distribution over depth at $t^* = 27$

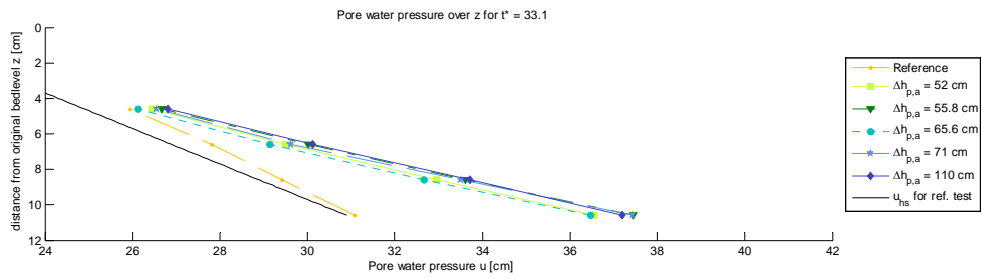


Figure A. 22: Pore water pressure distribution over depth at $t^* = 33.1$

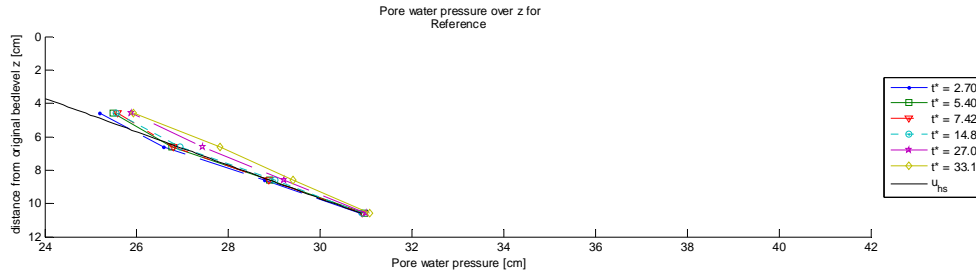


Figure A. 23: Pore water pressure distribution over depth during reference test

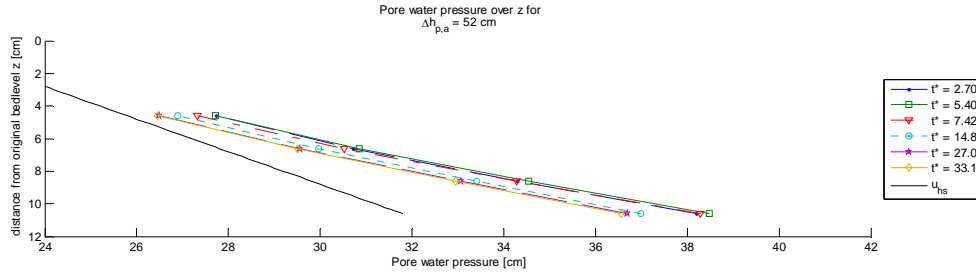


Figure A. 24: Pore water pressure distribution over depth during test with smallest excess pore water pressure

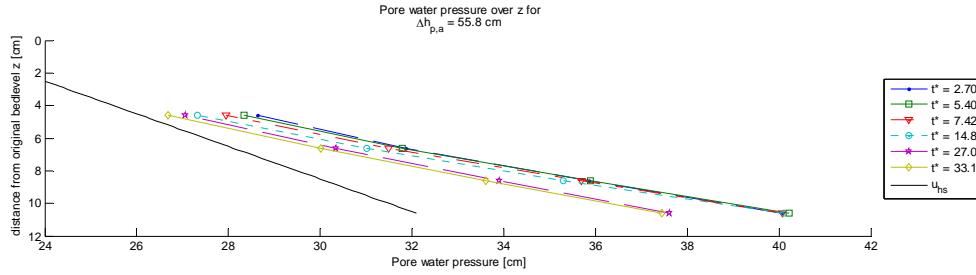


Figure A. 25: Pore water pressure distribution over depth during test with $\Delta h_{p,a} = 61.2$ cm

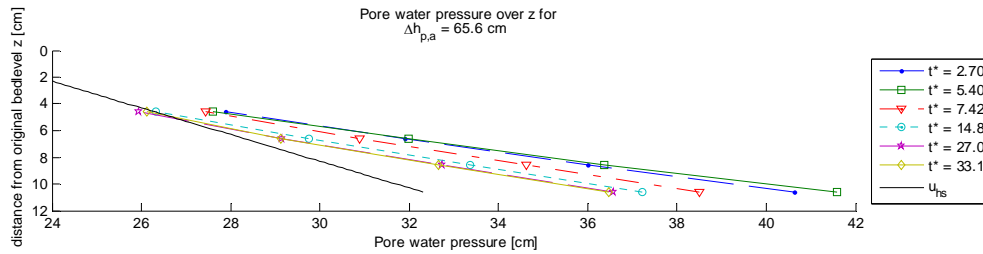


Figure A. 26: Pore water pressure distribution over depth during test with $\Delta h_{p,a} = 65.6$ cm

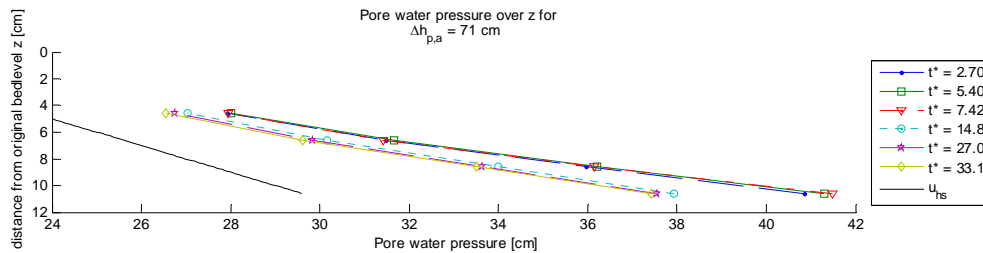


Figure A. 27: Pore water pressure distribution over depth during test with $\Delta h_{p,a} = 71$ cm

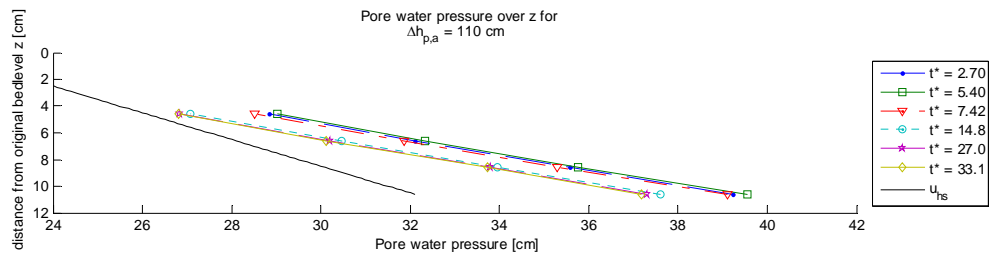


Figure A. 28: Pore water pressure distribution over depth during test with largest excess pore water pressure

Appendix E: Electromagnetic flow meter

An electromagnetic flow meter (EMS) is used for the measurements of the undisturbed current velocity at a distance of $\frac{1}{2}D$ from the bed. This quantity is referred to as U_c .

The device measures the velocity at a specific height in two directions. The output of the instrument is a voltage between -10 and +10 volt. The signal can be switched to 1m/s and 2.5 m/s. For a setting of 1m/s every change of 1 V corresponds to 0.1 m/s. For a setting of 2.5m/s 1 V implies a velocity change of 0.25 m/s. Because the measurement device shows some variation over time, the signal is averaged over 10 measurement points in time before it is stored. The accuracy is $\pm 1.5\%$ for the 1 m/s setting and $\pm 0.5\%$ for the 2.5 m/s setting. Reference is made to Delft hydraulics (1990) for more information on this device.

Appendix F: Preliminary tests on liquefaction

In order to obtain an estimate on the required height at which liquefaction occurs and to test the functioning of the porous stone preliminary tests are performed. A number of tests are performed at different heights.

Setup

The setup is shown in figure A.29. A bucket is put at a higher level than the aquarium, so that an overpressure is created in the porous stone. Water starts to flow toward the porous stone and creates an upward force on the sediment in the aquarium. The applied difference in pressure head between the bucket and the aquarium is denoted as $\Delta h_{p,a}$.

There is a significant resistance in the hose between the bucket and the aquarium. Additional resistance is present due to the connections between the bucket and the tap close to the bucket, since due to availability of parts, these have been chosen in a smaller diameter. Consequently, the actual pressure in the porous stone is significantly lower. Therefore the piezzometric head is measured again just before the porous stone by connecting a tube just before the porous stone and measure the height the water reaches. The difference in pressure head between the porous stone and the water height of the aquarium is referred to as $\Delta h_{p,od}$.

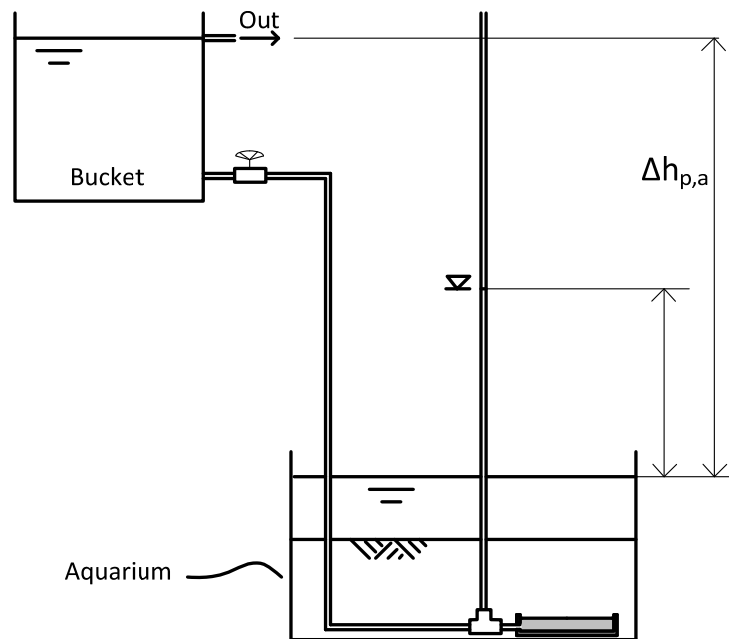


Figure A. 29: Schematised setup for preliminary tests on liquefaction.

Results

The results of these tests are shown in table A.3. Here test 1-10 the maximum time to wait was 5 minutes. For test 11-13 this waiting time was less, since they managed to liquefy the soil. During test 11-13 the discharge the bucket has to provide has been measured. This discharge is approximately 1.2 L/min.

Table A. 3: Results of preliminary tests on liquefaction

Meting no.	$\Delta h_{p,a}$ [cm]	$\Delta h_{p,od}$ [cm]	Liquefied [-]	total time [sec]	Discharge L/min
1	51	25.7	No	300	-
2	53.6	27	No	300	-
3	57.2	28.7	No	300	-
4	61.6	30.6	No	300	-
5	65.2	32.4	No	300	-
6	67	33.2	No	300	-
7	68.8	34.2	No	300	-
8	70.6	33.8	Yes	80	-
9	72.4	32.4	Yes	45	-
10	74.2	32.2	Yes	37	-
11	68.8	33	Yes	935	1.19
12	70.6	31	Yes	42	1.19
13	70.6	31.2	Yes	-	1.13

Description of process

After a certain period, part of the soil is pressed upward. This occurs in a shape similar to a saucer dome. The height gradually increases, implying the space of the pore becomes larger and the resistance to the excess pore water pressure declines, so the process is enhancing itself. Up to now the shape is relatively regular.

After a certain moment the vertical resistance of the sand is lost and a current brakes through which transports sand as if it is in suspension. As soon this blowout happened the flow concentrates in one feeder, which may slowly move in horizontal direction and does not necessarily have a regular shape. Furthermore it does not arise straight above the centre of the porous stone. The irregular shape could be explained by non-homogenous soil properties or an enclosed preference in the porous stone. The irregularity is more pronounced for smaller pressures. The height around the liquefied region keeps being slightly higher than the surrounding. A photo is given in figure A.30

**Figure A. 30: Photo of liquefied region after blow out.**

The saucer dome shape arose after 30 and 37 seconds for test 8 and 12 respectively, while the blowout occurred after 80 and 42 seconds for these tests.

It can be concluded that for $\Delta h_{p,a} \geq 68,8\text{cm}$ the soil manages to liquefy. The pressure head in the porous stone $\Delta h_{p,od}$ is approximately 33 cm but is not accurate, because it is time dependent. It should be noted that the time limit on the tests may veil that a smaller piezometric head can also lead to liquefaction, but the waiting time was insufficient.

After the upward flow was stopped, the sand keeps on being in a liquefied state for a while. This state may be assumed to follow the same behaviour as under wave-induced liquefaction from the moment that the liquefaction progressively dissipates, as was reported by Sumer et al. (2006). The pore water pressure gradient drives the water in the liquefied sediment upwards, while the sediment grains settle through the water until they begin to come into contact with each other. This consolidation progresses as line upwards through the sediment column (Sumer et al., 2006).

It should be noted here that the measurements are very inaccurate and sensitive to mutual differences in circumstances. They are only used to provide estimates and to get acquainted with the behaviour.